UC San Diego
UC San Diego Electronic Theses and Dissertations

Title
Advanced Sensing, Navigation, and Autonomy for Unmanned Underwater Vehicles

Permalink
https://escholarship.org/uc/item/2747z61s

Author
Gallimore, Eric Curtis

Publication Date
2019

Peer reviewed|Thesis/dissertation

UNIVERSITY OF CALIFORNIA SAN DIEGO

Advanced Sensing, Navigation, and Autonomy for Unmanned Underwater Vehicles

A dissertation submitted in partial satisfaction of the
requirements for the degree Doctor of Philosophy

in

Oceanography

by

Eric Curtis Gallimore

Committee in charge:

>   Eric Terrill, Co-chair
>   Jeffrey Gee, Co-chair
>   Mark Anderson
>   John Orcutt
>   Geno Pawlak
>   Daniel Rudnick

2019

The Dissertation of Eric Curtis Gallimore as it is listed on UC San Diego Academic Records is approved, and it is acceptable in quality and form for publication on microfilm and electronically:

_____

_____

_____

_____

_____
Co-chair

_____
Co-chair

University of California San Diego

2019

DEDICATION

For my father, Kevin Gallimore.

Engineers may be born or made, but he deserves credit either way.

EPIGRAPH

If all that experience has taught me anything, it's that the robot revolution
would end quickly, because the robots would all break down or get stuck
against walls. Robots never, ever work right.

Randall Munroe

TABLE OF CONTENTS

LIST OF FIGURES

LIST OF TABLES

ACKNOWLEDGEMENTS

It is impossible to completely acknowledge every person and organization who has contributed to both this work and my career. I apologize for the omission of deserving parties.

My advisor, Dr. Eric Terrill, provided me incredible opportunities throughout my graduate career, and supported me both professionally and personally throughout the process. It would have been impossible to conduct this research without his guidance and support. It has been a pleasure and a privilege to work with him.

Dr. Jeff Gee generously offered to serve as my co-chair, in addition to providing substantial insight and assistance with my magnetometer work. Dr. Mark Anderson provided substantial and helpful direction as I planned research, and then throughout the process. The other members of my committee, Drs. Daniel Rudnick, John Orcutt, and Geno Pawlak have also provided invaluable feedback and guidance.

The staff of the Coastal Observing Research and Development Center (CORDC) provided me a great home at Scripps, and they are some of the most talented and helpful people with whom I've had the pleasure of working. Lisa Hazard is generally responsible for making things happen, and she has been incredibly effective at navigating bureaucracy on my behalf. Team REMUS deserves special recognition: Andy Nager, Bob Hess, Gannon Gesiriech, Nixon Caruthers, and Josh Costa. In addition to being great lab-mates, Joel Hazard, Heidi Bachelor, Mike Jilka, Brian Kim, and Dr. Megan Cimino were great ship-mates. Dr. Peter Rogowski sat through an unreasonable number of my practice talks.

Dr. Travis Schramek went through the PhD process ahead of me, and his shared experience and sage wisdom have been more helpful than I can describe. Dr. Sophia Merrifield

Of course, I couldn't have done any of this without the unwavering support of my wife, Courtney. Despite any evidence to the contrary, I love her more than I love REMUSes.

Chapter 2, in full, is a reformatted reprint of the material as it appears in the Proceedings of the IEEE AUV Conference, 2018 The dissertation author was the primary investigator and author of this paper: E. Gallimore, R. Stokey, and E. Terrill, "Robot Operating System (ROS) on the REMUS AUV using RECON," in *Proceedings of the 2018 IEEE OES Autonomous Underwater Vehicle Symposium*, Porto, Portugal, 2018.

Chapter 3, in full, is a reformatted reprint of material as it appears in the Journal of the Acoustical Society of America, 2019. The dissertation author was the primary investigator and author of this paper: E. Gallimore, M. Anderson, L. Freitag, and E. Terrill, "Synthetic baseline navigation using phase-coherent acoustic communication signals," *Journal of the Acoustic Society of America*, In Press 2019.

Chapter 4, in part, has been submitted for publication. The dissertation author was the primary investigator and author of this paper: E. Gallimore, E. Terrill, A. Pietruszka, J. Gee, A. Nager, and R. Hess, "Magnetic survey and autonomous target reacquisition with a scalar magnetometer on a small AUV".

Chapter 5 contains material currently being prepared for submission for publication. The dissertation author was the primary investigator and author of this material: E. Gallimore, A. Pietruszka, E. Terrill, "The Detection of Submerged WWII Aircraft Sites via Autonomous Underwater Vehicle Based Magnetometer Survey".

VITA

2007   Bachelor of Science, Electrical and Computer Engineering, Franklin W. Olin College of Engineering

2016   Master of Science, Oceanography, Scripps Institution of Oceanography, University of California San Diego

2019   Doctor of Philosophy, Oceanography, Scripps Institution of Oceanography, University of California San Diego

PUBLICATIONS

E. Gallimore, M. Anderson, L. Freitag, and E. Terrill, "Synthetic baseline navigation using phase-coherent acoustic communication signals," Journal of the Acoustical Society of America, in press, 2019.

E. Gallimore, R. Stokey, and E. Terrill, "Robot Operating System (ROS) on the REMUS AUV using RECON," in Proceedings of the 2018 IEEE OES Autonomous Underwater Vehicle Symposium, Porto, Portugal, 2018.

E. Gallimore, E. Terrill, R. Hess, A. Nager, H. Bachelor, and A. Pietruszka, "Integration and Evaluation of a Next-Generation Chirp-Style Sidescan Sonar on the REMUS 100," in Proceedings of the 2018 IEEE OES Autonomous Underwater Vehicle Symposium, Porto, Portugal, 2018.

E. Terrill, M. Moline, P. Scannon, **E. Gallimore**, T. Shramek, A. Nager, R. Hess, M. Cimino, P. Colin, A. Pietruszka, and M. Anderson, "Project Recover: Extending the Applications of Unmanned Platforms and Autonomy to Support Underwater MIA Searches," Oceanography, vol. 30, no. 2, pp. 150–159, Jun. 2017.

B. Bingham, N. Kraus, B. Howe, L. Freitag, K. Ball, P. Koski and **E. Gallimore**, "Passive and active acoustics using an autonomous wave glider," *Journal of Field Robotics*, vol. 29, no. 6, pp 911-923, Nov 2012. doi: 10.1002/rob.21424

E. Gallimore, J. Partan, I. Vaughn, S. Singh, J. Shusta, and L. Freitag, "The WHOI Micromodem-2: A scalable system for acoustic communications and networking," in *OCEANS 2010*, Seattle, WA, 20-23 Sept. 2010, pp.1-7. doi:10.1109/OCEANS.2010.5664354

A. Kukulya, A. Plueddemann, T. Austin, R. Stokey, M. Purcell, B. Allen, R. Littlefield, L. Freitag, P. Koski, **E. Gallimore**, J. Kemp, K. Newhall, and J. Pietro, "Under-ice operations with a REMUS-100 AUV in the Arctic," in *2010 IEEE/OES Autonomous Underwater Vehicles (AUV)*, Monterey, CA, 1-3 Sept. 2010, pp.1-8. doi: 10.1109/AUV.2010.5779661

L. Freitag, K. Ball, P. Koski, S. Singh, and **E. Gallimore**, "Acoustic communications for deep-ocean observatories: Results of initial testing at the MBARI MARS node," in *OCEANS 2010 IEEE - Sydney*, Sydney, Australia, 24-27 May 2010, pp.1-6. doi: 10.1109/OCEANSSYD.2010.5603958

ABSTRACT OF THE DISSERTATION

Advanced Sensing, Navigation, and Autonomy for Unmanned Underwater Vehicles

by

Eric Curtis Gallimore

Doctor of Philosophy in Oceanography

University of California San Diego, 2019

Dr. Eric Terrill, Co-chair
Dr. Jeffrey Gee, Co-chair

Research results that advance the capabilities of autonomous underwater vehicles (AUVs) to conduct seabed surveys are described. These include the creation of a software framework to enable research and development in sensing and adaptive autonomy, a novel synthetic baseline navigation technique, and a magnetic sensing system that incorporates sense and react behaviors. Field experiments were conducted globally in a wide range of littoral environments to test hypotheses associated with the emerging field of autonomy as applied to underwater systems.

To facilitate sensor integration and provide a testbed for autonomous sense and react research, an onboard sensor processing and autonomy system was developed for the REMUS AUV using the Robot Operating System (ROS) that provides high-level control of the vehicle. Multiple vehicles outfitted with this system were used for seabed surveys, sensor evaluation, and engineering tests. This framework enabled the development of novel techniques for undersea navigation and magnetic sensing.

A synthetic baseline navigation technique that self-localizes an AUV using intermittent acoustic communications signals received by a single transducer is presented. The methodology is found to offer advantages over traditional acoustic-based navigation, in that it can operate with or without synchronized clocks, does not require acoustic transmissions dedicated to navigation, and can provide faster navigation solution convergence. The method uses the phase measurement at the output of a second-order phase-locked loop (PLL) to create fine-scale pseudo-range estimates in addition to, or in the absence of, a one-way travel time (OWTT) measurement based on the arrival time of the acoustic data packet. These range measurements are incorporated by an adaptive particle filter. This technique allows the vehicle navigation system to take advantage of multiple phase-derived range measurements made over the duration of a communication packet.

To enable geophysical and archaeological survey capabilities, a scalar magnetometer system has been developed and integrated into an AUV. Real-time signal processing mitigates platform effects of the vehicle. Development of autonomy for on-board processing and target detection, coupled with reacquisition behaviors, is found to increase the effective survey coverage rate by nearly 300% when searching for magnetic dipole targets.

The compact system collects data from a Micro-Fabricated Atomic Magnetometer (MFAM, Geometrics Corporation, San Jose, CA, USA), a total-field atomic magnetometer, and data from the sensor is both streamed to storage and made available to an onboard autonomy engine for real-time sense and react behaviors. Following characterization both in controlled laboratory conditions and at sea to determine its performance limits, methodologies for processing the magnetometer data to correct for interference and error introduced by the AUV platform were developed to improve sensing performance. When conducting seabed surveys, the developed autonomy is found to reliably detect and characterize targets of interest using physics-based algorithms designed to operate in real-time within the computational constraints of the AUV. Over the course of this research, the system was advanced to drive both single- and multiple-vehicle autonomous target reacquisition behaviors. Detailed results from surveys searching for submerged World-War II aircraft wrecks at locations worldwide are presented.

1 Introduction

Autonomous underwater vehicles (AUVs) face unique challenges relative to aerial and terrestrial robots, many of which stem from limitations in communication. As electromagnetic propagation is limited in water, the use of radio for navigation, control, and telemetry is not feasible. Alternative communication schemes, such as acoustic or optical systems, are high-latency and low-throughput or short-range, respectively [1]. These limits are physics-based [2], [3]. These limits in communication preclude the use of systems such as GPS for navigation while underwater, and it limits the ability of human operators to observe sensor data and command appropriate vehicle behavior in real-time.

Expanding the on-board capabilities of the AUV can overcome these limitations. Sensor data can be processed in real-time, and this can be used to drive behavior without human intervention. When using multiple AUVs to accomplish a task, their behavior can be coordinated effectively with frugal use of available communication bandwidth. Navigation in a global reference frame can be accomplished efficiently and accurately using signaling that operates underwater. Underwater vehicles serve to benefit greatly from the emerging scientific field of autonomy as a human "pilot-in-the-loop" is not readily available, in contrast to aerial or terrestrial counterparts.

This dissertation describes specific developments that advance these capabilities. These developments have been validated through at-sea experimentation, including operational use in support of expeditions in littoral waters at locations around the globe. This improved capability offers benefits for scientific, defense, and industrial use of AUVs.

1.1   Motivating Application

The work described here has broad applicability across a wide range of domains, but the research was largely targeted at the use of multiple autonomous underwater vehicles (AUVs) to conduct seabed surveys. This, in turn, was motivated by involvement with Project Recover, a multi-university collaborative organization that seeks to use advanced technology to locate and identify aircraft wrecks associated with servicemembers missing-in-action [4].

Seabed surveys when searching for wreck sites are often conducted using a "find-fix-finish" paradigm[4], [5], which corresponds to the use of wide-area, low-resolution sensors to conduct an initial search for potential targets ("find"), and then reinvestigation of those targets ("fix"), and finally detailed documentation of targets ("finish") [4], [5]. Autonomous underwater vehicles (AUVs) are used throughout these phases of search, where lower-resolution, longer-range sensors are used for initial search, and higher-resolution, shorter-ranges sensors are used for target reacquisition. The "finish" phase may be completed with AUV-based sensors, such as cameras or multibeam sonar, or by remote-operated vehicles (ROVs) or human divers.

The AUVs most commonly used for this work are torpedo-shaped two-man-portable REMUS 100 vehicles [6]. These are actively-propelled, versatile platforms that can carry a variety of instruments. Many sensors use a modular attachment system that allows payloads to be changed for different missions. It is common to use a single vehicle to operate several different sensors over the course of an expedition with many deployment sorties to meet operational requirements.

The initial search ("find") phase for aviation-debris-sized targets is typically conducted using low-frequency (600 kHz) sidescan sonar, which has a relatively long sensing range (greater than 75 m) but sufficient resolution to identify potential targets [7]. This provides a high survey

area coverage rate. Automatic detection of objects of interest in sidescan sonar imagery has been performed, but successful demonstrations to date rely on the objects in question having known, well-defined geometry [8]–[15]. Therefore, targets associated with aircraft debris are identified in sidescan sonar imagery post-mission by human analysts.

Once a potential target is identified, those targets are reacquired (the "fix" phase). At this point, a smaller area near the target is surveyed in higher resolution by the AUV to characterize the target and rule out false-positive target identifications. This may involve the use of high-resolution, short-range sidescan sonar, with the AUV making multiple passes at close range at several headings to obtain multiple images of the target with different acoustic look angles. High-resolution multibeam sonar or optical cameras may be used at this stage, although the effective range of these sensors is low. A magnetometer can be used to locate ferrous debris (Chapters 4 and 5).

Once the target has been reacquired, it may be documented further (the "finish" phase) using other platforms such as remotely-operated vehicles (ROVs) or human divers, depending on the survey area and other expeditionary concerns.

AUVs have been used for a variety of archaeological applications, with a focus on locating and characterizing shipwrecks [5], [16]–[20]. The use of cooperative teams of multiple AUVs for archaeological seabed survey offers the potential to increase survey efficiency. This area is less well-explored, although it has been touched upon in simulation studies [21]–[23].

Surveys of this nature are also used for mine countermeasures (MCM) operations, which involve searching an area for targets of interest [24], [25]. This was an early application for AUVs, and an important application that has driven the development of the REMUS AUV, to

3

the benefit of the scientific research presented here [26]–[28]. The use of networked, cooperative groups of AUVs for this application has been explored since the late 1990's (e.g. [29], [30]).

1.2   Synthetic Sensor Processing

AUVs generally control and measure their motion with precision. Even when the AUV is unable to use external references such as acoustic transponders for large-scale or global localization, it can often maintain good relative motion tracking using sensors that directly measure the vehicle's velocity over the seabed (Doppler velocity logs, or DVLs). This enables synthetic sensing: treating a collection of measurements made by a moving sensor over time as if they were collected by a spatially-distributed array.

The exploitation of synthetic sensor processing is central to the work described here. It is applied to vehicle navigation in Chapter 3, where the vehicle motion is used to create a synthetic "baseline", which refers to a set of locations used for trilateration. In Chapters 4 and 5, synthetic magnetic field gradients are calculated from measurements taken using a single sensor on a moving AUV. Performing these calculations introduces computational complexity, but this additional computation load is now compatible with modern processing capabilities that can be installed in AUVs (Chapter 2).

1.3   Autonomy

Autonomous underwater vehicles are often operated with basic levels of autonomy: they operate with closed-loop control of attitude and velocity, and they are capable of navigating between predefined waypoints [24, p. 1]. For typical seabed survey applications, human operators manually plan survey tracks, and the vehicle navigates to waypoints along the survey tracks to the best of its ability as defined by its navigation accuracy.

Sense-and-react autonomy, where the vehicle interprets sensor measurements in real-time and makes decisions that drive path-planning behavior, is a logical step in enhancing the capabilities of AUVs. This has been used to adaptively sample a variety of oceanographic phenomena, and it has been demonstrated with both buoyancy-driven gliders [31]–[38] and propeller-driven AUVs [39]–[44]. Sense-and-react autonomy has also been previously explored for seabed surveys, but without substantial progress due to the limited scope of those studies. [45] describes a nested survey approach where areas of high interest are mapped and then resurveyed. [46] used a proprietary automatic target recognition system to identify mine-like-objects in sonar data and performing reacquire maneuvering.

The framework described in Chapter 2 enables sense-and-react autonomy aboard REMUS AUVs, and Chapter 4 describes the development and application of autonomy behaviors that respond to magnetic target detections.

1.4 Overview

The subsequent chapters detail several specific advancements in sensor processing, navigation, and autonomy.

Chapter 2 describes a software framework used for sensor integration and autonomy on a family of small AUVs, along with details on hardware implementation. This system is built upon the Robot Operating System (ROS) [47], and it provides standardized messaging as well as a straightforward command-and-control interface that can be used to build complex autonomous behaviors. The capabilities provided by this framework were instrumental to conducting the research described in subsequent chapters, and it enables reactive autonomy on-board the AUV.

Chapter 3 details a novel synthetic baseline navigation technique that uses phase information contained in standard acoustic communication signals to self-localize an AUV. Underwater navigation presents unique challenges, and these are exacerbated when operating several AUVs in a confined survey area. As GPS signals cannot penetrate water, other methods are used to provide navigation in a global reference frame. The method detailed in this chapter offers several advantages over preexisting approaches: it does not require that the vehicle transmit acoustic navigation signals ("go active"), it does not require synchronized clocks throughout the network (although it can take advantage of them if they are present), it uses existing telemetry or command-and-control acoustic communication signals, and it is well-suited to situations where multiple vehicles must operate within acoustic range of one another. AUV position estimates are formed by a particle filter that incorporates phase measurements from a phase-locked loop that tracks the carrier of incoming acoustic communication packets. The performance of this technique was validated through at-sea experimentation.

Chapter 4 describes the use of a scalar total-field magnetometer that is integrated on the AUV and used for geophysical and archaeological surveys. The system, based on a Geometrics (San Jose, CA, USA) Micro-Fabricated Atomic Magnetometer (MFAM), is characterized under controlled laboratory conditions and in the field. A variety of signal processing techniques to mitigate measurement noise and error induced by the AUV platform are described. When performing seabed surveys to locate and identify magnetic targets of interest, measurements from this sensor are processed in real-time during the mission by detection and classification algorithms that use a physics-based model of magnetic anomalies. Autonomy routines that leverage this real-time target detection capability are used to trigger both single-vehicle and

multiple-vehicle autonomous target reacquisition behaviors. This capability is found to significantly increase the effective coverage rate of the magnetic survey system.

Chapter 5 provides additional details on the specific use of the magnetometer system for locating and characterizing sites associated with downed World-War II aircraft. It describes operational differences between this system and the towed magnetometers that are sometimes used in archaeology. Several specific sites are documented, including descriptions of the magnetic properties of artifacts at those sites.

2 ROS on the REMUS 100 AUV using RECON

To facilitate sensor integration and provide a testbed for autonomous sense and react research, an onboard sensor processing and autonomy system has been developed for the REMUS 100 AUV using the Robot Operating System (ROS) and the REMUS RECON interface, which provides backseat control of the vehicle. An interface library, pyREMUS, has been developed to handle the REMUS RECON interface, and a ROS package, ros_remus, uses this library to provide a deep level of interoperability between the REMUS vehicle computer and other ROS-based subsystems. This system has been deployed on multiple REMUS 100 vehicles and it is currently used operationally for field research programs. Vehicles outfitted with this system have seen numerous deployments, where they have been used for seabed surveys, sensor evaluation, and engineering tests.

2.1 Introduction

The Robot Operating System (ROS) [47] is a popular open-source robotics middleware system that has been widely adopted by the research and industrial communities [48]. It has been deployed on several research AUVs [49], [50]. The commercial manufacturer of the REMUS, Hydroid (Pocasset, MA, USA), has indicated that it will be used on the "Next Generation" REMUS 100 vehicle [51], but no open-source interface is currently available.

The system described here makes significant use of an API provided by the REMUS vehicle computer, called "RECON" [52], to provide a ROS interface that can relay data from the vehicle and its on-board sensors to other ROS systems. It also allows ROS nodes to control the vehicle's behavior.

This system has seen extensive operational use, totaling over 500 mission-hours across four REMUS 100 vehicles operated by the Scripps Institution of Oceanography (La Jolla, CA, USA). Most of these missions have been seabed surveys with objectives beyond the testing of software. Notable expeditions include extensive archaeological surveys in Hansa Bay, Papua New Guinea, and Kiska, Alaska, USA, where numerous World-War-II-era aircraft and shipwrecks were found. Additionally, the system has enabled testing and prototyping of novel sensors and autonomy behaviors.

2.2 Architecture overview

The ROS-based system is used as a "back-seat driver" in the vehicle, sending commands to and receiving telemetry from the vehicle's primary CPU and operating software. This implementation allows us to leverage existing tools and rapidly develop new sensor interfaces and behaviors with little risk to the safety of the AUV, which remains under the primary control of the REMUS vehicle operating system.

Furthermore, the system is designed such that high-level control of the vehicle, such as mission planning, can take place entirely via ROS, entirely via the vehicle's standard mission planning interface, or using a mixture of the two. This allows users familiar with traditional REMUS mission programming to immediately take advantage of features implemented in ROS, and it facilitates testing of new functionality.

The major components of the system described in this paper are the RECON vehicle interface, the pyREMUS library that manages the RECON interface and makes it accessible to other modules via Python, and the ros_remus ROS package, which contains the nodes that bridge the RECON interface to the ROS system (Figure 2.1).
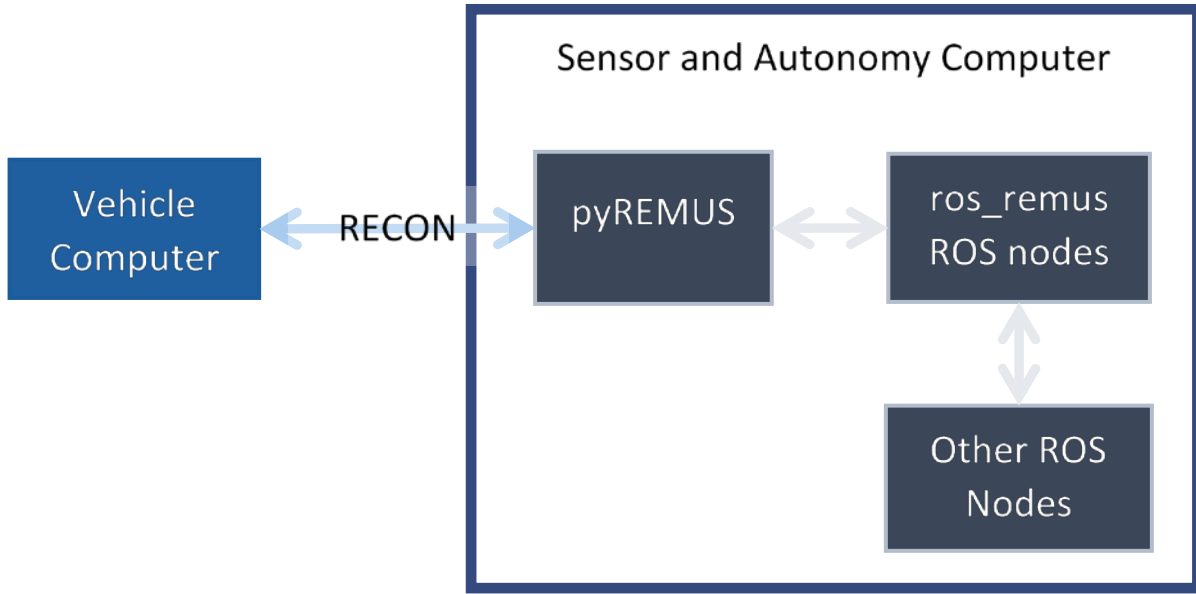
Figure 2.1: Overview of system architecture. RECON is used to communicate between the vehicle computer and the sensor/autonomy computer. This is facilitated by a library named "pyREMUS", which manages the connection and performs appropriate message translation. The "ros_remus" package provides a ROS node that uses the pyREMUS library to interface between the vehicle computer and other ROS components via ROS messaging.

2.2.1 RECON

RECON was initially developed for an ONR program with the goal of using a REMUS 100 to track a plume to its source using a chemical "sniffer" [42]. This required a sensor processing computer to find a plume and then steer the vehicle towards the source. The initial design was based around the division of labor aboard a research vessel: captain and crew (vehicle) were responsible for ship safety, the science party (client) was responsible for achieving the research objectives. The initial RECON controls were low-level and rudimentary. In subsequent years, additional features were added at the behest of users that gave clients far more capabilities, now reaching into all aspects of vehicle operation.

RECON provides a telemetry, command, and control interface to the REMUS vehicle computer for use by external computers. It follows a publish-subscribe model for messaging

over UDP sockets. The protocol uses human-readable ASCII messages with 8-bit checksums to ensure integrity. Messages are sent asynchronously from the vehicle computer to the RECON client to provide sensor data and vehicle status information at user-specified intervals. Commands that change vehicle behavior are sent from the client using the same message interface, and the vehicle responds with appropriate status messages as commands are executed.

The command interface provides both low-level vehicle control, such as commanding a heading and speed, and also complex tasks, such as navigating in a survey pattern. Commands to perform any of these operations can be queued at the vehicle, allowing a state machine on the vehicle computer to track progress. It is also possible to save lists of commands as subroutines on the vehicle computer, which can then be invoked by the RECON client by name using a single command message. The vehicle mission planner provides a mechanism to enable and disable back-seat-driver control via RECON for different segments of the mission.

RECON commands are integrated with the REMUS VIP interface program, such that projected vehicle paths are appropriately plotted in the navigation display. Additionally, RECON commands and the resulting behavior are logged in the vehicle computer log for post-mission analysis using the same tools typically used to review REMUS mission logs.

RECON provides a "help" interface that can be used by an operator or programmatically for interface introspection. This is useful when accounting for differences among vehicles, as the host can determine which features are available via the RECON interface by querying the help system.

RECON also provides an interface to indicate subsystem status to the vehicle computer. For example, this can be used to trigger a mission abort in the case of a critical failure or log the error and notify the operator. Additionally, it provides a watchdog system (using keepalive

messages) that allows the vehicle to detect when communication with the RECON client has failed. At all times, the "front-seat" vehicle computer monitors vehicle health and safety, and it will override commands sent by RECON clients if necessary.

2.2.2 PyREMUS

A library named "pyREMUS" provides the software interface to the vehicle CPU. It provides a "Pythonic" (idiomatically correct Python) mechanism to use the REMUS RECON interface and exposes the RECON features described above. This library communicates with the vehicle computer via a UDP socket and handles message parsing, generation, and dispatch. Parameters of RECON messages are converted to and from appropriate Python types.

Although it is used here to connect to ROS, pyREMUS is middleware-agnostic. It can be used to build an interface with MOOS or other autonomy systems, or directly interface sensors with the vehicle. It currently runs under Python 2.7 or Python 3 and requires only the Python standard library.

pyREMUS can operate with any REMUS vehicle running RECON version 3 or 4, including both REMUS 100 and REMUS 600 vehicles.

2.2.3 A very brief overview of ROS

ROS provides a collection of tools and libraries that implement features commonly needed by a variety of robots. It supports message-passing between separate processes that run on one or several computers via a publish-subscribe mechanism (called, intuitively, "publishing" and "subscribing" to "messages") as well as a remote procedure call mechanism called "services". Processes that either publish or subscribe to messages are called "nodes". It also provides tools for inspection of running systems and logging data. ROS is described in great detail in its documentation [53].

2.2.4 ros_remus

The ros_remus package provides several modules, including the ROS node that serves as the primary interface between the vehicle computer and other ROS nodes in the system. It also defines ROS message types that correspond to REMUS RECON messages and performs appropriate type conversions.

It incorporates logic to monitor and report the mission state of the vehicle, which is widely used for logging and sensor control. The module also provides a node, mission_bag_node, which generates new ROS bag log files on mission start and stop. This simplifies logging sensor data, since sensor nodes need only publish messages containing data, and this can be logged by the mission_bag_node.

There is also an additional node, node_status, that allows monitoring and reporting ROS node status to the vehicle. This node is packaged separately to simplify its use in other nodes that may not have other dependencies on messages in the ros_remus package. This is commonly used to toggle annunciators in the REMUS Vehicle Interface Program and generate entries in the vehicle computer log. The annunciators can be configured at run time by setting ROS parameters (programmatically or in the ROS launch file).

2.3 Sensors

In the systems fielded to date, each sensor is supported by a ROS package and at least one ROS node that controls its operation. Most sensor controllers leverage the telemetry from the vehicle and provide simple status feedback to the vehicle computer. Generally, sensors are decoupled from autonomy; other nodes are responsible for monitoring sensor data and commanding appropriate vehicle behavior.

The authors have developed drivers for sidescan sonars, multibeam sonars, a magnetometer, optical imagers, and an experimental acoustic navigation system. Additionally, existing open-source ROS drivers have been used to integrate new sensors in the vehicle.

2.3.1 Sensor control and configuration

REMUS vehicle missions are built from "objectives", which represent tasks that the vehicle executes in sequence. Different objectives require that different sets of sensors are enabled and configured, so each objective specifies an "instrument setup" configuration. On the vehicle computer, the mission file includes a mapping of instrument setup names to sensor configurations (for any sensors that are directly controlled by the vehicle).

To take advantage of this capability and provide compatibility with traditional REMUS vehicle mission programming, pyREMUS and ros_remus can also use the instrument setup names defined in the vehicle mission. The instrument setup name for the currently running objective is published in the remus/status topic, and it is therefore available to any node when the vehicle is running. ros_remus also incorporates a mechanism for controlling sensors, so they don't need to parse or interpret the instrument setup name internally.

An instrument setup configuration that maps instrument setup names to sensor control parameter can be specified in YAML via a dedicated file or inline in a roslaunch file. This file (Figure 2.2) defines how each sensor under ROS control should operate. The instrument_setup_node monitors and parses the instrument setup name from the remus/status message and then uses dynamic_reconfigure [54] to control sensor nodes based on the mappings in the instrument setup configuration file. Therefore, any sensor node that supports

14

dynamic_reconfigure can be controlled via the REMUS vehicle mission without modification.

```yaml
# The default setup is used when the instrument
# setup is not listed elsewhere. It also sets
#default values for each sensor that can be
# optionally overridden below.
default:
    arcscout:
        enabled: yes
        range: 75
    norbit:
        enabled: no
    hanucam:
        enabled: no


# The underscore ("_") indicates that we should
# search for this string in the instrument setup
# name, not match the whole name
_camera:
    arcscout:
        enabled: yes
        range: 30
    hanucam:
        enabled: yes
        exposure: auto
        interval: 0.1


# This matches a specific instrument setup name
transit:
    arcscout:
        enabled: no
```

Figure 2.2: Sample Instrument setup file, showing commonly used functionality. The syntax is YAML that is compatible with the ROS parameter subsystem, and it can be included in a roslaunch file or as a separate file

2.4   Actions

RECON provides the ability to directly command relative complex actions, such as navigating a complete survey pattern, with a few messages. After first "adding" the message to the queue, parameters can be subsequently modified as required, for example by changing the row length, spacing, number of rows, or orientation/heading. It can also be used to compose complex sequences of actions, which are then tracked by a state machine in the vehicle controller such that the back-seat driver need only monitor the overall status of the action sequence. pyREMUS makes these actions available to Python programs, and the ros_remus node exposes this functionality via actionlib, a ROS library that provides a standard interface for performing tasks [55]. actionlib provides a mechanism for commanding an action, monitoring progress, and receiving feedback that the action has been completed successfully or failed.

The implementation of actions in the vehicle computer and exposed via RECON maps well to the paradigm of actionlib actions. Therefore, ros_remus exposes action servers that map directly to RECON actions. Additionally, ros_remus implements an action to execute a series of RECON transit actions, which corresponds to navigating to a series of waypoints. Table 2.1 describes the actions available in ros_remus and via RECON.

Table 2.1: Summary of ros_remus and RECON actions

ros_remus action	RECON action	Description
Transit	Transit	Transit to a waypoint
TransitList		Transit to a series of waypoints, via multiple RECON Transit actions
Rows	Rows	Navigate in a "mow-the-lawn" survey pattern
Loiter	Loiter	Slowly circle a waypoint (to keep the vehicle close to one location)
SurfaceLoiter	Surface Loiter	Surface the vehicle and then circle a waypoint
	Manual	Follow a heading at a specified speed. Not currently implemented in ros_remus
Circle	Circle	Circle a waypoint with a specified radius

Most actions provide properties that allow the user to specify vehicle depth, altitude, speed, and which navigation sensors to use. Presently, ros_remus does not provide a mechanism to manually command vehicle heading and speed, as this functionality has not been required by any applications to date. However, this capability is exposed via pyREMUS, should it become necessary to incorporate it in the future.

2.4.1 Behaviors

These actions can be used to compose complex autonomy behaviors. Since they are exposed via actionlib, they are easily used with state machine libraries such as SMACH [56]. They may also be called directly without the use of additional libraries. The behaviors themselves are not part of the remus node or the ros_remus package, and they are tailored to particular missions and use cases.

Typically, one or more behaviors is implemented in a node that processes sensor input and invokes ros_remus actions. An arbiter node may be used to select among behaviors provided by other behavior nodes, facilitating modularity and code reuse.

2.5 Multi-vehicle Operation

Various mechanisms exist to support ROS operation across multiple robots connected via a network [57]. For use on AUVs, however, systems that provide high levels of convergence between robots by passing significant amounts of data over a network are not suitable, since AUV communication throughput is severely limited during operation. Rather than attempting to synchronize the complete state of the robot or pass all messages between robots, only a select subset of messages necessary for a particular cooperative operation are passed between vehicles using an acoustic modem link.

2.5.1 Acoustic communication

Systems have been developed to communicate over heterogeneous underwater acoustic links from ROS [58] and other middleware, but this system is more complex than we require.

The primary mechanism for underwater communication on the REMUS is a WHOI Micromodem-2 acoustic modem [59], which, in this configuration, has a maximum burst throughput of 5kbps. Although RECON provides an interface to use the acoustic modem via the vehicle computer, this mechanism places limitations on data rates and packet sizes. Instead, the autonomy computer connects to a second serial port on the modem and uses it directly.

A ROS node subscribes to relevant ROS topics. When specified ROS messages are received, they are marshalled into a compact binary format for acoustic transmission, and then transmitted. The timestamp associated with the ROS message header is used as a unique

identifier that can be used to provide positive acknowledgement of received messages. When acoustic messages are received, the inverse occurs, and the node publishes a ROS message corresponding to the received message.

Presently, the marshalling format for each message used acoustically is user-defined via Python functions to handle marshalling and unmarshalling. Work is ongoing to build a system that parses ROS message files with optional metadata and marshals messages into a format that is compatible with the dynamic compact control language (DCCL) [60].

2.5.2 Multi-vehicle behavior

Multi-vehicle autonomy is achieved by passing either stimuli or commands from one platform to the other and then operating a behavioral state machine that executes a series of actions via ros_remus. This architecture is flexible and does not enforce a particular multi-agent control strategy.

An overview of how this system operates when performing multi-vehicle autonomous target reacquire is shown in Fig. 2. In this case, one vehicle is equipped with a sensor system that identifies targets of interest while conducting a seabed survey (often called automatic target recognition, or ATR). The ATR node publishes messages with details about the targets it has detected. The acoustic communication (acomms) bridge node subscribes to these messages and relays them via the acoustic modem. A second vehicle equipped with a different sensor that will be used to re-survey the target receives this acoustic message. The acomms bridge node publishes the received message, which is then handled by a behavior node that decides if and how the vehicle should navigate to investigate the target. The behavior node then calls appropriate actions via the actionlib interface on the remus node, which commands the vehicle accordingly.

This use-case has been exercised at sea to perform autonomous multibeam sonar reacquisition of archaeological targets identified by a magnetic target detection system operating on a different vehicle.
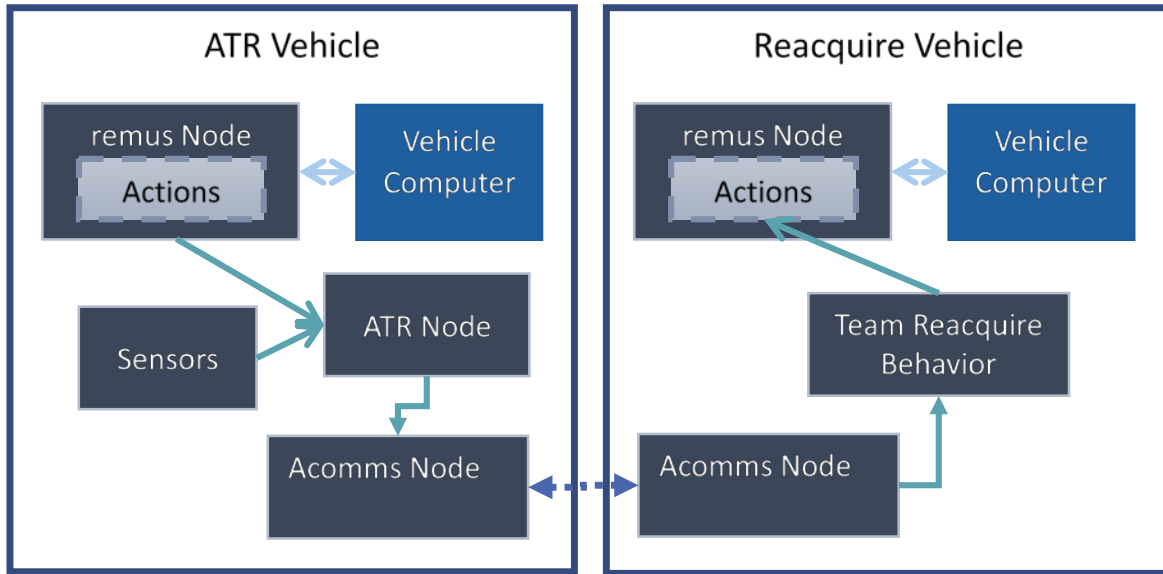
Figure 2.3: Overview of system architecture for multi-vehicle autonomous target reacquision. In this example, a vehicle ("ATR Vehicle") identifies a target of interest and passes target information to the "Reacquire Vehicle", which maneuvers to resurvey ("reacquire") the target.

2.6 Implementation

In our vehicles, the ROS-based software stack runs on x86-based single board computers. Two configurations are used: one based on an Intel Atom E3845 quad core processor, for applications that require more processing capability, and one based on an Intel Atom Z34xx SOC for applications where minimizing power consumption is critical.

These systems run either Ubuntu or a custom OpenEmbedded Linux distribution. Automatic startup of the ROS system is handed by a systemd unit that calls roslaunch. The roslaunch file used on a particular AUV is determined automatically by searching for a file name that matches the computer's hostname. This allows all the autonomy computers across multiple

20

vehicles to use the same code, and the appropriate configuration is automatically selected at runtime.

ros_remus has been used operationally at sea under two ROS versions: ROS Kinetic (released 2016) and ROS Indigo (released 2014). Testing with ROS Melodic (released 2018) is ongoing.

The system has been deployed on four REMUS 100 vehicles thus far, and installation on additional REMUS 100 and REMUS 600 vehicles is underway.

2.7 Conclusion

A system has been developed that leverages the REMUS RECON interface to provide a ROS interface to the REMUS AUV. It provides reusable components that allow novel sensor integrations and autonomy development, with significant integration to the REMUS mission planning system. Vehicles outfitted with this system have seen extensive operational use, and they have been used for seabed surveys, sensor evaluation, and engineering tests of other systems. The system continues to be developed to improve its capabilities, and integration with additional vehicles is ongoing.

2.8 Acknowledgment

This chapter, in full, is a reformatted reprint of the material as it appears in the Proceedings of the IEEE AUV Conference, 2018 The dissertation author was the primary investigator and author of this paper: E. Gallimore, R. Stokey, and E. Terrill, "Robot Operating System (ROS) on the REMUS AUV using RECON," in *Proceedings of the 2018 IEEE OES Autonomous Underwater Vehicle Symposium*, Porto, Portugal, 2018.

3 Synthetic Baseline Navigation with Phase-coherent Acoustic Communication Signals

The development of a synthetic baseline navigation technique that self-localizes an autonomous underwater vehicle (AUV) using intermittent acoustic communications signals received by a single transducer is described, along with field results from in-ocean tests. The method uses the phase measurement at the output of a second-order phase-locked loop (PLL) to create fine-scale pseudo-range estimates in addition to, or in the absence of, a one-way travel time (OWTT) measurement based on the arrival time of the acoustic data packet. These range measurements are incorporated by an adaptive particle filter. This technique allows the vehicle navigation system to take advantage of multiple phase-derived range measurements made over the duration of a communication packet. These measurements, when incorporated with an appropriate filter and vehicle kinematic model, improve vehicle navigation at no additional cost in navigation-specific acoustic transmissions. This approach was demonstrated and evaluated with data collected at-sea using a REMUS 100 AUV.

3.1 Introduction

AUVs have traditionally relied on acoustic navigation techniques such as long-baseline (LBL) or ultra-short-baseline (USBL) systems, which require measuring two-way acoustic travel times between multiple transmit or receive elements to form a navigation solution [61], [62]. These techniques generally form least-squares maximum likelihood estimates of position using a well constrained set of time-delay-of-arrival measurements.

The use and development of accurate and synchronized clocks has enabled one-way travel time measurements that are suitable for navigation (e.g. [63], [64]). Various systems have been developed that employ a single estimate of the one-way travel time of an acoustic communications packet rather than a signal dedicated to navigation [63]–[66]. These systems offer several advantages over traditional LBL and USBL navigation: they reduce the number of acoustic transmissions required, are scalable to any number of receivers, and eliminate one path delay to reduce latency. Navigation solutions using one-way travel time may using one or several transmitters depending on the implementation and its desired accuracy and spatial coverage.

Synthetic baseline navigation computes a localization solution by leveraging the motion of either the AUV or another platform to provide multiple range measurements over time. This has been demonstrated using two-way travel time to transponders [67], [68] and with USBL-style direction-of-arrival measurements [69]–[71]. A primary objective of these methods is to reduce the number of acoustic emitters, ideally to one, or to improve the quality of the navigation solution for a given number of transponders or navigation beacons. Similar techniques have been used to localize moving sources using fixed receive arrays that exploit acoustic channel structure [72]. Generally, the navigation solution is computed using linear estimators (least squares or Kalman filters) that incorporate range measurements, a model of vehicle kinematics, and other

sensor inputs available on a platform. Recently, particle filters have been used to improve performance of traditional USBL navigation systems coupled with other navigation aids such as a Doppler velocity log (DVL) [73].

The work presented here builds upon the navigation methods reviewed above. Importantly, it relies only on phase tracking information that is often already available from Doppler estimators in acoustic communications receivers. The specific approach presented here takes advantage of the phase-locked loop (PLL) incorporated in a decision-feedback equalizer in a single-carrier communications receiver but could be adapted to other modulation methods that use high-resolution Doppler estimators.

This approach enables localization using acoustic communication signals when one-way travel time (OWTT) is not available, and it is therefore useful when synchronize transmit and receive clocks are not available. When OWTT measurements are available, this technique reduces the uncertainly of the position estimate, which enables localization using fewer acoustic transmissions.

3.2   Implementation

The navigation system, described in detail in this section, uses an adaptive particle filter to estimate vehicle position. The process model is based on the vehicle kinematics and incorporates a 7-variable state vector along with control inputs. High-resolution pseudo-range measurements are computed using the phase-tracking output of the acoustic receiver while communication packets are being received. The measurement model incorporates these pseudo-range measurements along with an initial starting range derived from the one-way travel time of the communication packet, if it is available, velocity information from the vehicle's doppler

velocity log, and heading information from the vehicle attitude and heading reference system. Localization of the vehicle is achieved using a hybrid particle filter where position is tracked by a particle filter and other state variables are tracked using an unscented Kalman filter.

3.2.1 Kinematic Process Model

The vehicle is localized using a two-dimensional constant turn rate and velocity kinematic model that also incorporates horizontal water current. A complete description of the dynamics of an underwater vehicle involves 18 state variables, and current (fluid velocity) requires at least three more[1]. For both conceptual and computational simplicity, the model tracks only a subset of the state, which is sufficient to track the vehicle.

Depth is not explicitly tracked in this model, although it is indirectly incorporated in some measurement functions of the tracking filter. This assumption is reasonable, as the depth of the vehicle can be measured with high precision and accuracy using a pressure transducer. Furthermore, the vehicle sway velocity is incorporated in the current velocity terms. As the vehicle uses only one thruster, which propels the vehicle forward or backward and cannot directly induce transverse motion, any sway over ground is due primarily to ocean currents.

The vehicle surge velocity (forward, through water), yaw, and yaw rate are composed in the body-fixed frame, while the current velocity and vehicle position are in local North-East-Down (NED) coordinates. The corresponding state vector is

---

[1] Corresponding to force, velocity, and pose of surge, sway, heave, roll, pitch, and yaw. Irrotational current requires another three velocity states. See, e.g., [74]

$$\boldsymbol{x} = \begin{bmatrix} \text{postition, North} \\ \text{position, East} \\ \text{current velocity, North} \\ \text{current velocity, East} \\ \text{vehicle surge velocity} \\ \text{vehicle yaw (heading angle)} \\ \text{vehicle yaw rate} \end{bmatrix} = \begin{bmatrix} x \\ y \\ u_C \\ v_C \\ u \\ \psi \\ r \end{bmatrix} \qquad (1)$$

The vehicle control inputs include speed and steering control, corresponding to the rotational rate of the propeller and the angle of the rudder:

$$\boldsymbol{u} = \begin{bmatrix} \text{propeller speed} \\ \text{rudder angle} \end{bmatrix} = \begin{bmatrix} n \\ \delta_r \end{bmatrix} \qquad (2)$$

With these controls, the speed model is

$$u = b_u(n) \qquad (3)$$

Where b_u is an empirically-determined function mapping propeller rotation rate to vehicle speed through water. The steering model is

$$r = b_\delta(\delta_r) \qquad (4)$$

Where b_δ is an empirically-determined function mapping rudder angle to vehicle yaw rate. Both of these empirical functions can be determined by performing a polynomial fit to experimental data collected on the vehicle over a range of speed and steering inputs.

The horizontal position is calculated using the kinematic differential equations

$$\dot{x} = u_C + u \cos \psi \qquad (5)$$

$$\dot{y} = v_C + u \sin \psi \qquad (6)$$

And the yaw and yaw rate are related as

$$\dot{\psi} = r \qquad (7)$$

3.2.2 Pseudorange Measurement via Phase Tracking

The navigation technique exploits the phase tracking information required to properly demodulate and equalize a phase-shift keyed (PSK) communications packet, which is made available from a phase-locked loop. The approach is independent of the type of signal constellation, and it may be BPSK, QPSK, or higher order. This output of the PLL is a phase time series that can be used to generate hundreds of estimates of range between the transmitter and receiver for each packet, depending on the length of the packet and its bandwidth.

Typical PSK packets begin with an acquisition probe (such as an FM sweep), followed by a PSK-modulated sequence that includes an equalizer training sequence and coded data.

The implementation described here is based on the processing done by a WHOI Micromodem-2 acoustic modem. In this system, the acquisition probe is detected using a matched filter, and the modem determines and reports a time of arrival that corresponds to this detection. If clocks at the transmitter and receiver are synchronized, this process alone can be used to determine one-way travel time for navigation purposes [65]. The Micromodem-2 provides time-of-arrival measurements with one microsecond precision and to the accuracy governed by bandwidth and the acoustic propagation channel. The modem clock can be synchronized with a reference, such as a pulse-per-second signal from a GPS at the start of a mission or with a stable atomic clock in the vehicle [59].

The initial range estimate for each packet is made using the time-of-arrival (TOA) measurement for the acquisition probe. Using the known time of transmission, this forms a single one-way travel time (OWTT) measurement, assuming a direct acoustic path. This implementation uses the local speed of sound (as measured by the AUV via a CTD) to determine

a corresponding geometric range, but this can be improved by use of ray tracing to compute the average sound speed over the path taken by the signal from its source.

The QPSK sequence is processed using an adaptive equalizer that incorporates an LMS adaptive filter and a second-order PLL for carrier phase tracking. The equalizer estimates the channel impulse response and applies a corresponding filter to the incoming samples, such that the channel effects are mitigated. The PLL phase gradient is calculated by measuring the phase difference between the received QSPK symbol, as demodulated using the PLL-adjusted carrier, and a known training symbol. Each packet incorporates a DC-balanced training sequence chosen to enable this carrier recovery. The PLL is tuned such that most of the motion-induced Doppler shift is tracked by the PLL and not by the group delay of the LMS filter, using parameters from Johnson et al. [75]. This process is illustrated in Figure 1. A more detailed discussion of the adaptive equalizer can be found in [76].
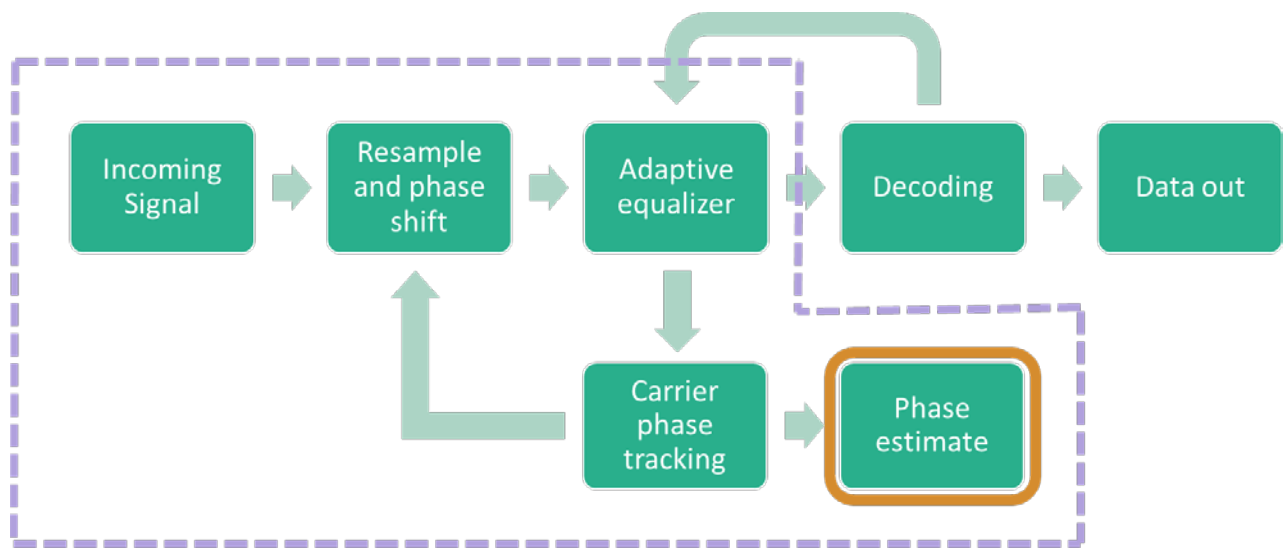
Figure 3.1: Block diagram showing basic processes involved in receiving PSK acoustic communication signals. The portion of this process that is used for navigation in this work is enclosed with the dashed line.

The PLL-tracked phase is then low-pass filtered and delay-corrected. The phase measurement controls a resampling filter that applies a corresponding group delay (positive or negative) to the incoming samples such that time dilation or contraction is removed. The group delay (T) associated with this phase shift is given as

$$T = -\frac{\phi}{2\pi f_c} \tag{8}$$

where ϕ is the phase shift and f_c is the carrier frequency.

In this method, the calculated group delay is tracked throughout the received packet and is used indirectly to generate pseudorange measurements for each received symbol at a decimated rate that is chosen to match the cutoff frequency of the low-pass phase filter.

It should be noted that the measurements are only valid if the equalizer has converged and is operating with reliable feedback. If not, the phase gradient measurement may be invalid, and this error will propagate into the group delay estimate. Typically, the equalizer converges during training where perfect feedback is available and then continues to operate reliably after changing to decision-directed mode. To test that the measurements are valid, the equalizer mean-squared error (MSE) is low pass filtered to provide a reliable low-noise estimate, and, when the MSE for a symbol is low (less than 1, corresponding to positive output SNR), the equalizer is in a converged state. In this state, the algorithm considers the group delay estimate for that symbol to be valid.

The local speed of sound is used to convert each filtered and gated group delay measurement to a difference in range between subsequent received symbols. This process yields a series of range measurements between the source and receiver over the duration of the received packet which are then used in the Bayesian tracking filter to localize the AUV.

3.2.3 Measurement Models

The measurement models incorporate the phase-derived pseudorange measurements, one-way travel time measurements, and data from the vehicle's doppler velocity log (DVL) and attitude and heading reference system. An appropriate model is selected to incorporate only the measurements that are available in each time step.

The pseudoranges to each transmitting source are calculated using the phase-tracking method described above. The range relation is given as

$$\rho = \sqrt{(x_{source} - x)^2 + (y_{source} - y)^2 + (z_{source} - z)^2} \tag{9}$$

where ρ is the range and x, y, and z are distances in Cartesian space. The vertical components (z) are not modeled but are used directly by the measurement functions.

The DVL reports bottom tracking velocity in the body frame: surge velocity u_{DVL} and sway velocity v_{DVL}. These are related to state as

$$u_{DVL} = u + u_C \cos \psi + v_C \sin \psi \tag{10}$$

$$v_{DVL} = u_C \sin \psi + v_C \cos \psi \tag{11}$$

The vehicle attitude and heading reference system (AHRS) measures yaw rate and heading angle (adjusted to true North) as

$$r_{gyro} = r \tag{12}$$

$$\psi_{compass} = \psi \tag{13}$$

We assume that measurement noise is normally distributed for each of these instruments, and each of them reports data at different rates, as summarized in Table 3.1.

Table 3.1: Summary of measurements and instruments used for navigation with their update rates, standard deviation, and availability.

Measurement	Instrument	Typical Measurement rate	Typical Standard Deviation	Availability
Range from one-way travel time (OWTT)	Acoustic comms system with synchronized clocks	<0.1 Hz	0.01-10m (depending on time synchronization and error sources described in text)	Intermittently, once each time a packet is received (if TX and RX time are synchronized)
Difference in range from phase tracking information	Acoustic comms system	Up to PSK symbol rate	0.00012m	During packet RX for approx. 3.5s
Velocity over ground	DVL (1200kHz RDI Workhorse ADCP)	0.5 - 2 Hz	0.3 cm/s [77]	When vehicle is <25m above seafloor
Yaw (heading) and heading rate	AHRS (Kearfott INS) or magnetic compass	9-10 Hz	0.1 (INS) to 3 deg (magnetic compass)	Continuous

3.2.4   Localization with Hybrid Particle Filter

Tracking and localization of vehicles is commonly performed using Kalman filters to estimate position and velocity. When the system being modeled includes nonlinear states or measurements, extensions of the Kalman filter are often employed, such as the extended Kalman filter (EKF) and the unscented Kalman filter (UKF) [78]. The UKF improves upon the EKF for many systems, and details relating to its performance and implementation are widely discussed in the literature, e.g. [74], [79]–[81].

Despite its advantages over the EKF, the UKF may still perform poorly when applied to some nonlinear systems. In practice, the pseudorange measurement data proves unsuitable for a

linear or linearized filter because the corresponding measurement equation (8) is nonlinear, and the associated probability densities can be multimodal and nongaussian in Cartesian space.

To avoid some of the problems associated with using a linear filter with a nonlinear system, a particle filter is used to form vehicle location estimates. The particle filter does not assume that the system is linear, Gaussian, or unimodal. Several excellent overviews of particle filters exist, see e.g. [82]–[84], and the implementation used in this system is described below.

However, tracking all the state variables in a particle filter would be computationally prohibitive in an embedded system. To address this, the implementation partitions the state into linear and nonlinear components, which are tracked with a UKF and a sequential-importance-sampling (SIS) particle filter, respectively. The particle filter acts as an integration filter that incorporates the estimate from a UKF, as illustrated in Figure 2.
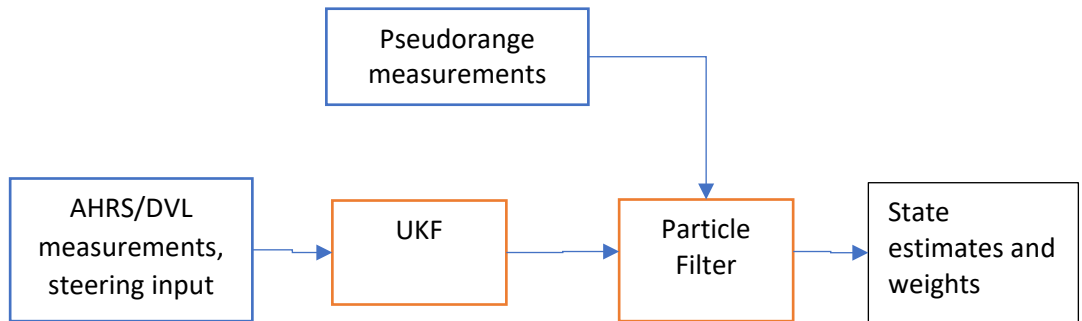
Figure 3.2: Block diagram showing data flow in Integrating navigation filter using UKF and particle filter

In this hybrid filter, the model is simplified such that the particle filter only tracks the following state.

$$x^p = \begin{bmatrix} \text{postition, North} \\ \text{position, East} \end{bmatrix} = \begin{bmatrix} x \\ y \end{bmatrix} \tag{14}$$

A separate unscented Kalman filter uses DVL, AHRS, and steering data to estimate a state vector,

$$x^k = \begin{bmatrix} \text{vehicle velocity over ground} \\ \text{vehicle heading over ground} \end{bmatrix} = \begin{bmatrix} v_g \\ \psi_g \end{bmatrix} \tag{15}$$

The velocity and heading over ground incorporate the effects of both currents and AUV body motion.

The Kalman state estimate is used as a control input to the particle filter in the prediction step as

$$x_{t+1}^p = f\left(x_t^p, x_t^k, v_t\right) \tag{16}$$

where v is process noise, and f is a function that predicts the state variables as

$$x_{t+1} = x_t + \left(v_{g,t} + v_{v,t}\right) \cos \psi_{g,t+1}^p \, dt \tag{17}$$

$$y_{t+1} = y_t + \left(v_{g,t} + v_{v,t}\right) \sin \psi_{g,t+1}^p \, dt \tag{18}$$

3.2.5   Particle Filter Measurement Update

The measurement update operates in one of two modes. If a one-way travel time measurement corresponding to a total range is available, the filter adjusts the particle weights using the pseudorange data via the measurement equation (8) and the expressions

$$f_X(x) = \mathcal{N}\left(\rho_{i,predicted}, R_\rho\right) \tag{19}$$

$$w_i = f_X(x), \qquad x = \rho_{measurement} \tag{20}$$

where $f_X(x)$ is the probability density function of a normally-distributed random variable with mean $\rho_{predicted}$ (from the measurement function) and variance R. w_i is the particle weight, found by evaluating $f_X(x)$ at the measurement value.

When using the phase-derived time difference of arrival data, the filter operates instead with the difference in range given by taking the group delay T_i, from equation (8), and multiplying by the speed of sound (c) measured by the AUV:

$$d\rho_{measurement} = T_i c \tag{21}$$

The prior is formed using the control vector output from the UKF to update the nonlinear state vector as described in (17) and (18) and taking the discrete difference of the state across time steps:

$$d\rho_{i,predicted} = \sqrt{(x_{t+1} - x_t)^2 + (y_{t+1} - y_t)^2 + (z_{t+1} - z_t)^2} \tag{22}$$

Note that z is not tracked by the filter, but measurements of depth are used directly.

The filter adjusts particle weights in this mode as described above for the one-way travel time case, but with

$$f_{d\rho}(x) = \mathcal{N}\left(d\rho_{i,predicted}, R_{d\rho}\right) \tag{23}$$

$$w_i = f_{d\rho}(x), \qquad x = d\rho_{measurement} \tag{24}$$

The particles are roughened (also called jittering or diffusing) by adding additional independent Gaussian noise to prevent sample degeneracy and reduce the effects of dependent noise processes in the sampling system.

In both cases, particle weights are normalized after calculation such that

$$\sum_i w_i = 1 \tag{25}$$

The particles are resampled after each update if the number of effective particles drops too low (below N/2, where N is the number of particles), using a common approximation as described in [84],

$$\widehat{N}_{eff} = \frac{1}{\sum_i w_i^2} \tag{26}$$

where w_i is the weight of each particle. Particle resampling is done with a systematic resampler [85].

3.2.6 Position State Estimates

Position state estimates are generated by calculating the weighted mean of the particle state vectors.

$$\widehat{x_t^p} = \begin{bmatrix} \widehat{x}_t \\ \widehat{y}_t \end{bmatrix} = \sum_i w_i \begin{bmatrix} x_{i,t} \\ y_{i,t} \end{bmatrix} \tag{27}$$

Notably, this estimate may not characterize a multimodal distribution in a useful way, so a weighted covariance variance of the state particles is computed to help quantify the validity of the estimate.

$$Q^p = \frac{1}{1 - \sum_{i=1}^{N} w_i^2} \sum_{i=1}^{N} w_i \left(x_t^p - \widehat{x_t^p} \right) \left(x_t^p - \widehat{x_t^p} \right)^T \tag{28}$$

These position estimates and covariances form the output of the localization system.

3.3 Simulation

To validate the basic functionality of the localization technique, the filter algorithms were run using simulated vehicle movements across a range of realistic values. This demonstrated that the particle filter could successfully incorporate both one-way-travel-time measurements as well as pseudorange measurements using the algorithm described in the previous section. An illustration of the output of the particle filter and estimator from a single acoustic packet simulation is shown in Figure 3.3.
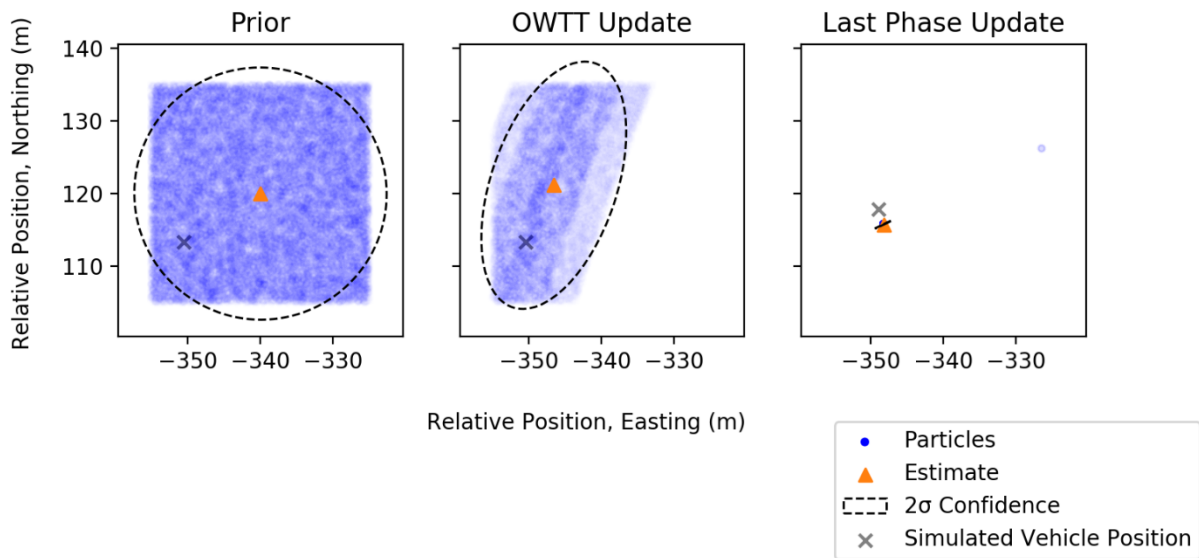
Figure 3.3: Plot of particle distributions and navigation filter estimates operating over a single simulated acoustic comms packet of approximately 5 second duration while the simulated vehicle travels at an average of 1.5 m/s. Positions are relative to the simulated transmitter. Each particle (dot, blue color online) is partially transparent, with its opacity determined by the weight of the particle. Therefore, darker regions correspond to higher-probability regions. 2-sigma covariance ellipses are drawn with dashed lines. (The covariance ellipse in the right subplot is small and overlaps with the estimate marker). The weighted estimate, as described in Eqn. 27, is plotted as a triangle (orange color online). The first subplot ("Prior") shows an initial particle distribution, which was deliberately chosen such that it was offset from the simulated position of the vehicle (marked with a cross). The center subplot shows the distribution and estimate associated with the one-way-travel-time measurement update, and the corresponding reduction in uncertainty is noticeable. The right plot labeled, "Last Phase Update," shows the output of the filter after incorporating hundreds of pseudorange measurements. Most of the particles are clustered near the estimated position (and the estimate marker covers most of the dots). Of interest, this example shows an additional cluster of particles near -335m Easting and 125m Northing, which represent another, less probable, position region that remains tracked by the particle filter, illustrating an advantage of this nonlinear filtering technique.

3.4 Experiment and Results

To evaluate performance of this navigation system under real-world conditions, a REMUS 100 AUV was operated in ocean waters adjacent to the Scripps Pier in La Jolla, CA.

The vehicle was programmed to swim a north-south and east-west survey pattern (Figure 3.4) in constant-altitude mode at a speed of 1.5m/s for approximately 750m in each direction. This mission geometry is typical for seabed survey applications using the REMUS 100, and it offered a variety of ranges and aspects between the transmitter and the vehicle.

An acoustic communication gateway buoy (a device that incorporates a subsurface acoustic transducer, an acoustic modem, and a radio link for surface communication) was deployed from the end of a pier, approximately 100m to the east of the operating area. It transmitted Rate 1 Micromodem packets with a 25kHz carrier, 5kHz bandwidth, and duration of about 4 seconds. Packets of this length and type are commonly used for AUV telemetry.

Packets were transmitted at varying intervals throughout the trial, with a maximum frequency of 4 packets per minute. Although more frequent packet transmission could improve the navigation performance, since more phase measurements would be available, the maximum packet frequency was chosen such that there was enough time between transmissions to allow the vehicle's standard long baseline navigation and acoustic communication systems to operate during the experiment.
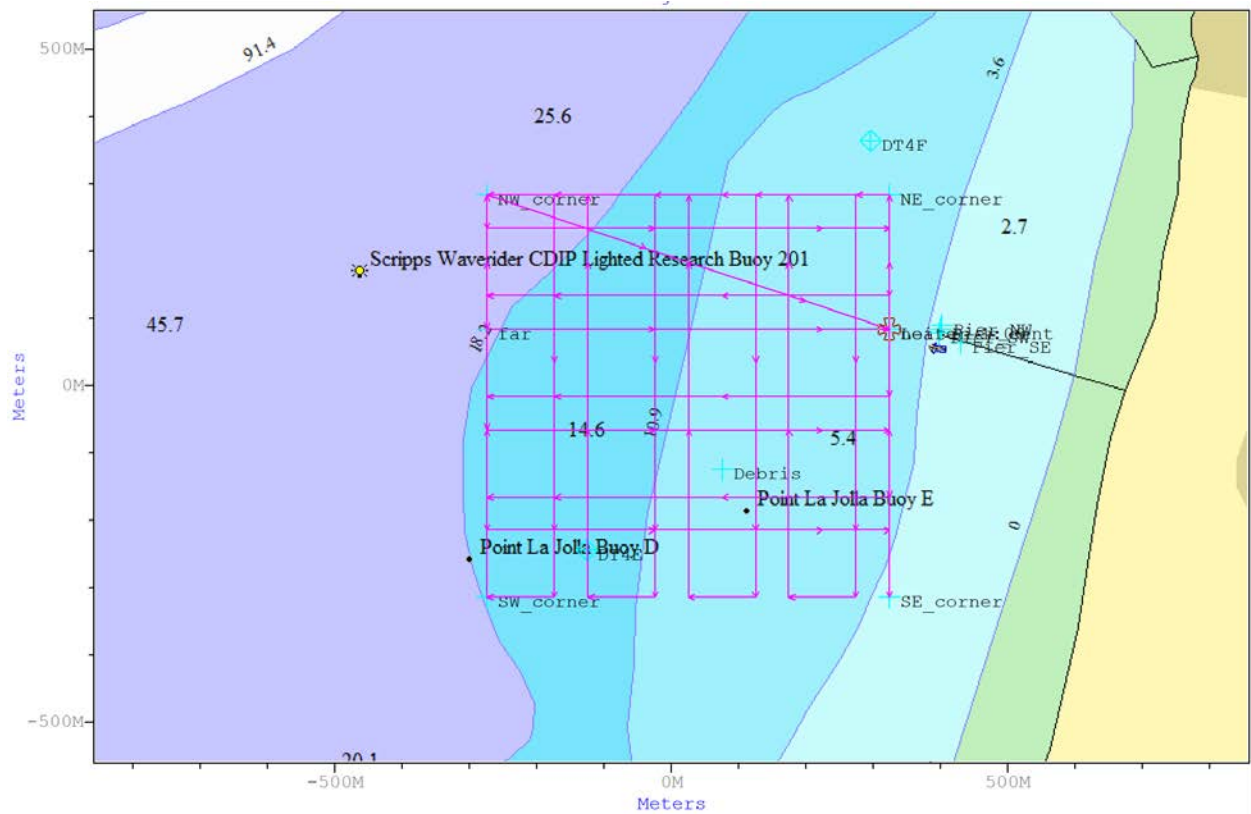
Figure 3.4: REMUS mission plan. Lines with arrows (magenta color online) indicate the planned vehicle track. Bathymetry is notated by background shading (color online).

3.4.1 Vehicle Hardware

The REMUS vehicle was equipped with a custom passband acoustic recording system that captured data from a single HTI-96 hydrophone mounted at the front of the vehicle (Figure 3.5). The vehicle is approximately 1.5 m long, and the minimum turning radius is about 5 m.

Figure 3.5: REMUS 100 vehicle used for this experiment, shown as it is being deployed. The hydrophone is visible at the vehicle nose. The modem hardware and passband recorder is incorporated within the vehicle's dry payload section (inside the yellow hull section).

The hydrophone signal was amplified and filtered by analog circuitry prior to being simultaneously processed by a Micromodem-2, which provided GPS-synchronized timestamps for the packet time-of-arrival [86], and sampled by a 96kHz passband recorder, as illustrated in Figure 3.6

.
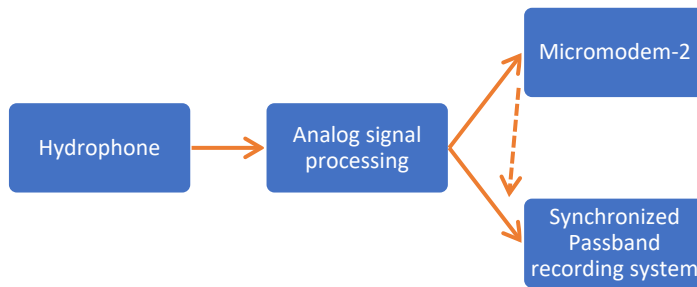
Figure 3.6: Block diagram of recording system integrated in the REMUS AUV.

To allow evaluation of the mode in which one-way travel time is used, a chip-scale atomic clock (CSAC) manufactured by Microsemi Corporation (Aliso Viejo, California, USA) was incorporated using custom interface hardware. For this experiment, the CSAC was used only as a real-time clock to control drift in the time of arrival measurements, and not used to derive a phase-locked analog-to-digital converter clock.

The acoustic recordings, vehicle AHRS, vehicle DVL, timing information, and additional diagnostic data were logged using a software stack built upon the Robot Operating System (ROS) [47].

These data were processed offline using the navigation filters described above, and the results were compared with the vehicle internal navigation track. The vehicle's internal navigation solution was formed by proprietary algorithms incorporating sensor data (from the vehicle AHRS, GPS when surfaced, and DVL) as well as intermittent long-baseline transponder fixes.

3.4.2 Results using adaptive filter incorporating one-way travel time

During the aforementioned mission, the filter was found to capably incorporate data from both the one-way travel time measurements as well as phase measurements. The progression of

measurement updates as two packets are received is shown in Figure 3.7 and Figure 3.8. In this example, 10000 particles are generated and randomly distributed uniformly over a $900m^2$ area. The vehicle's actual position falls within this area (but not at its center). In most applications, the initial particle distribution should be chosen such that it adequately samples the possible locations of the vehicle. These experimental results suggest that an initial particle density between 10 and 20 particles per square meter is sufficient.
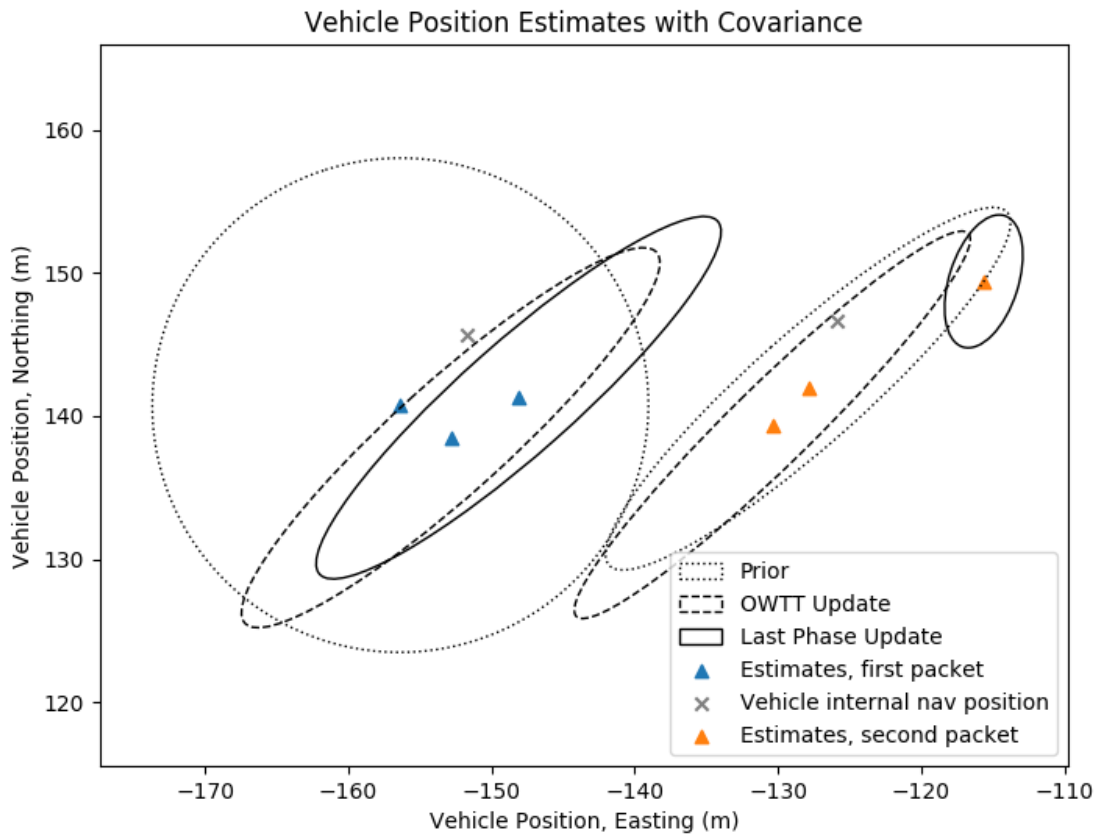
Figure 3.7: Plot of estimates of vehicle position (triangles) and 2-sigma covariance ellipses for the adaptive filter. As the vehicle travels east (left to right on the plot), two packets are received. Covariance ellipses are plotted showing the covariance of a prior estimate (the output of the predictor before measurements are incorporated) as a dotted line, a dashed ellipse showing the estimate once the one-way travel time (OWTT) measurement is incorporated, and a solid ellipse showing the estimate after all the phase measurements for the packet are incorporated. Many phase measurement updates are performed, but only the estimate after the last update is plotted for clarity. The decreasing area of the covariance ellipses shows how the filter incorporates data from one-way travel time measurements as well as phase estimates to improve the accuracy and confidence of the position estimate. The latest vehicle's internal navigation fix at the time of the last phase update is plotted for comparison. Inaccuracy in the survey of the LBL transponder and buoy positions during this experiment account for the differences among the position estimates.
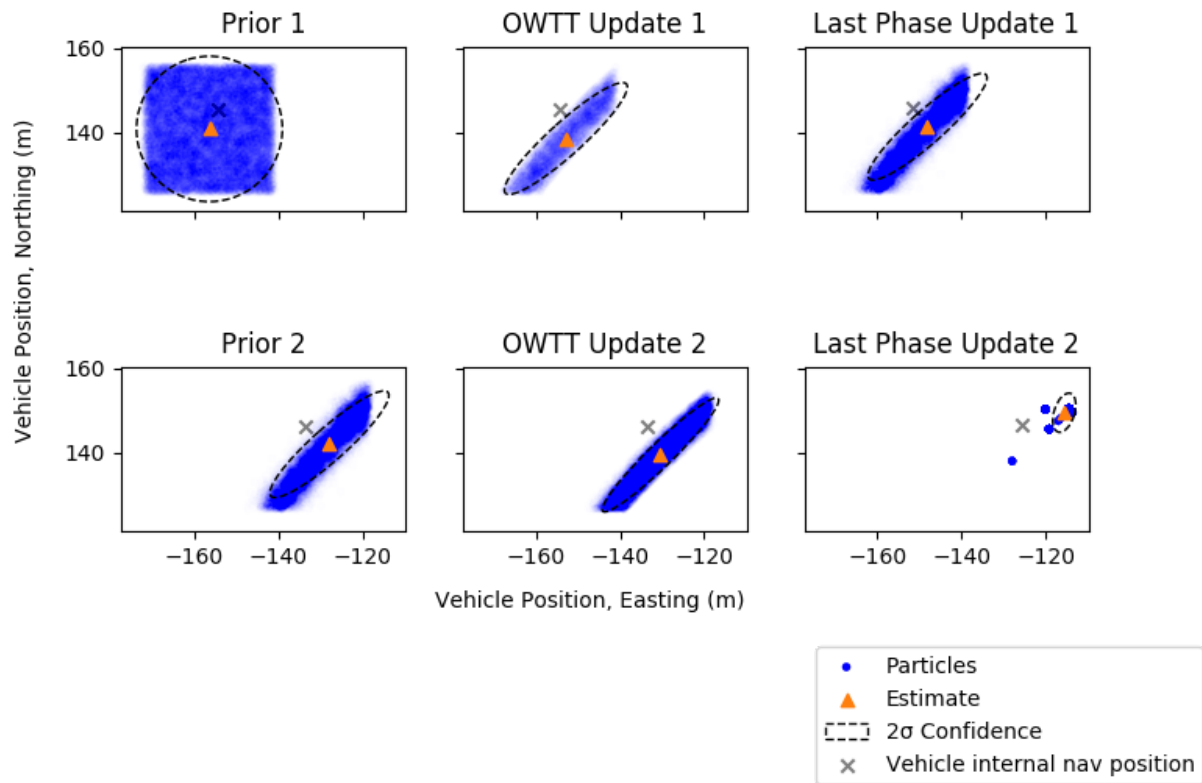
Figure 3.8: Particle distributions with corresponding position estimates and covariance ellipses, shown as two packets are received by the moving vehicle. This figure illustrates the same sequence as illustrated in Figure 3.7, but it shows the particle cloud at each step. Each particle (dot, blue color online) is partially transparent, with its opacity determined by the weight of the particle. Therefore, more opaque regions correspond to higher-probability regions. The first subplot ("Prior 1") shows the user-provided initial particle distribution. The lower-right plot labeled, "Last Phase Update 2," shows that the additional phase measurements from the second packet allow the filter to converge.

The benefit of incorporating the phase-derived pseudorange data is apparent when comparing the performance of the navigation filter using only the one-way travel time (OWTT) data and the results using pseudorange measurements. Figure 3.9 shows how the uncertainty of the position estimate (shown as the standard deviation of the estimate) decreases as a series of packets are received over a 25-minute period. The use of phase-derived pseudorange

measurements in addition to the OWTT causes the navigation estimate to converge much more quickly, using fewer received acoustic packets. It also performs well even when there are long intervals during which no packets are received. Therefore, this method is more suitable than operating with only OWTT measurements when acoustic packets are received only intermittently. Even when OWTT measurements are regularly available, using pseudorange data improves the certainty of the position estimate.
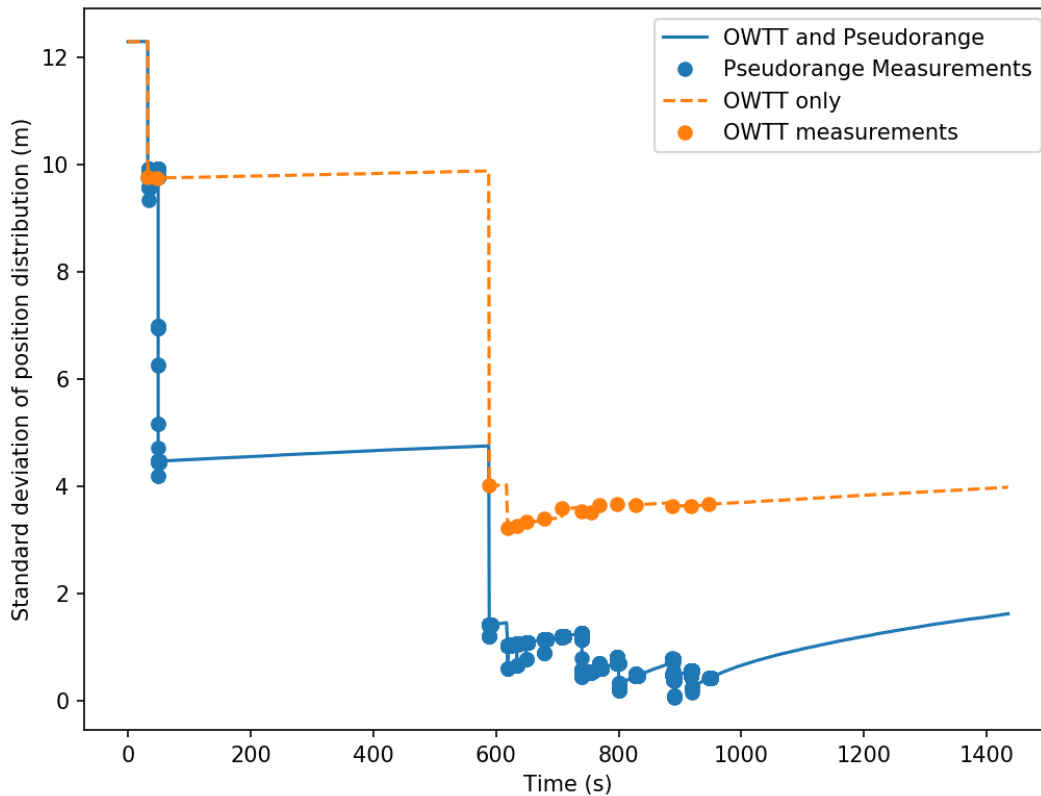
Figure 3.9: Weighted standard deviation (square root of trace of Equation 28) of the position estimates generated by the filter. Results are shown for the case where both pseudorange and OWTT measurements are used (solid line, blue) and when only the OWTT measurements are used (dashed line, orange). Phase measurement updates are highlighted using blue dot markers, and OWTT measurement updates are highlighted with orange dot markers. Note that uncertainty grows with time in the absence of new measurements, which can be seen in the areas where there are gaps between received packets (periods with no measurement markers). The reduction in uncertainty from using the phase measurements is apparent when comparing the results from the OWTT-only and OWTT-and-pseudorange measurement cases.

3.4.3   Results without one-way travel time

The performance of the navigation system using only phase measurements within packets, and not one-way travel time measurements, was also evaluated. This represents

46

situations where time is not accurately synchronized between the transmitter and receiver and, therefore, one-way travel time measurements are unavailable. Figure 3.10 shows a plot of localization estimates generated using only the phase-derived pseudorange data, along with associated covariance ellipses and the vehicle's internal navigation track.
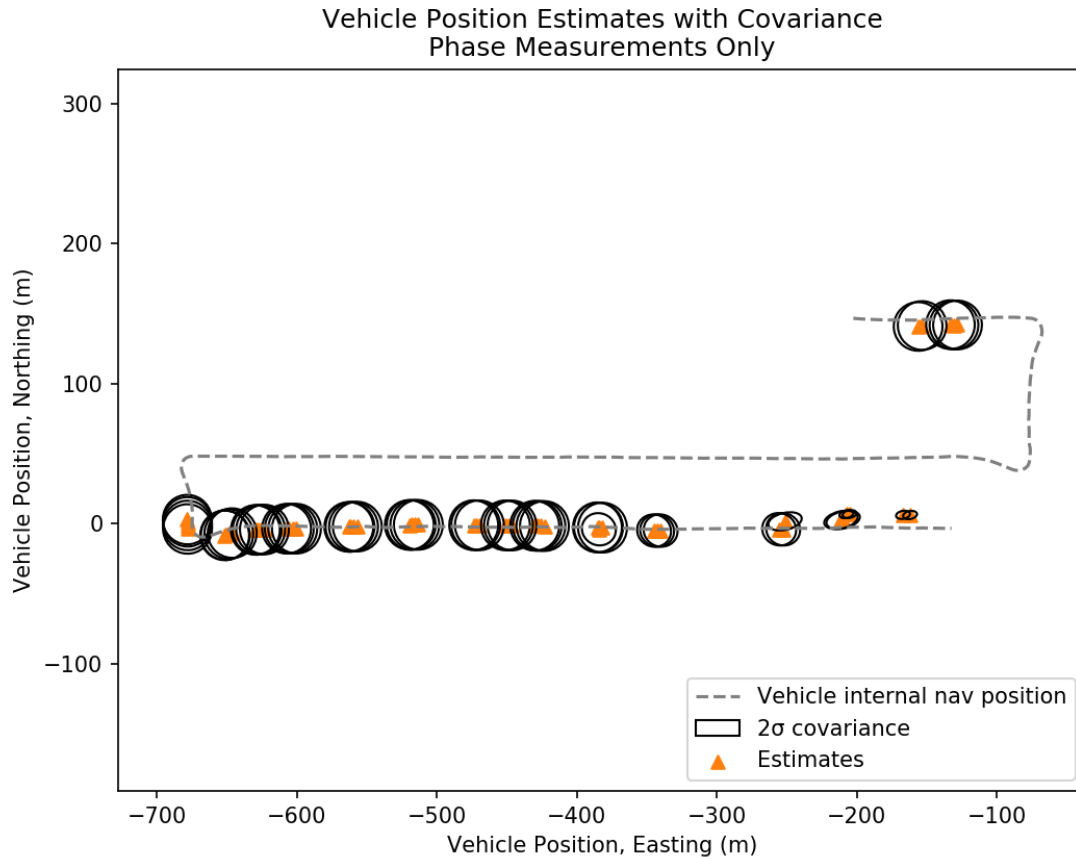
Figure 3.10: Plot of estimates of vehicle position (triangles) and 2-sigma covariance ellipses for the filter using only phase measurements. As the vehicle travels east and south (left to right, from top to bottom, on the plot), sixteen packets are received, and the navigation filter runs continuously. Many phase measurement updates are performed, but only a few estimates per packet are plotted for clarity. The decreasing area of the covariance ellipses shows how the filter incorporates data from phase estimates to improve the confidence of the position estimate. The position estimate from the vehicle's internal navigation system is plotted as a gray dashed line. Note that measurements are only intermittently available (and entirely absent while the vehicle is travelling west), but the filter still tracks the vehicle position. The offset between the filter position estimate and the vehicle's internal navigation solution is about 12 meters at the last estimate, which is within the accuracy bounds of this experiment.

When operating without one-way travel time (OWTT), the filter still converges, but many additional measurements are needed to achieve levels of certainty in the position estimate comparable to the adaptive filter case described above, as shown in Figure 3.11.
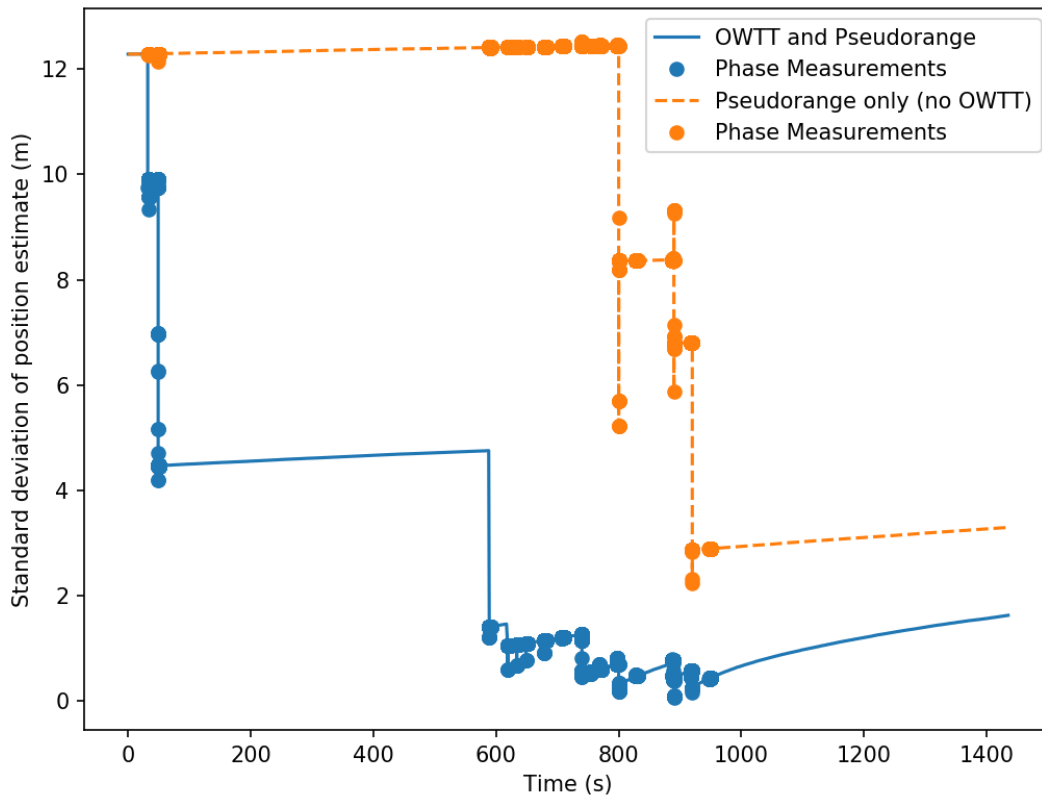
Figure 3.11: Weighted standard deviation (square root of trace of Equation 28) of the position estimates generated by the filter, comparing the performance when OWTT is used (solid line, blue) and when OWTT is not available (dashed line, orange). Phase-derived pseudorange measurements are highlighted with dot markers (blue and orange color online). The certainty of the estimate improves as more data is incorporated by the filter in both cases, but the lack of OWTT data always increases the uncertainty of the estimate.

In both cases, the filter estimates converge to positions near the REMUS navigation algorithm estimates of position, which incorporated intermittent LBL navigation transponder fixes. The differences in position between the filter estimates and the REMUS algorithm are within the accuracy bounds of the experiment (several meters), which were limited by uncertainty in the position of LBL transponders and the transmitting buoy, all of which were manually surveyed using a handheld GPS. Future experimental validation could be performed on an instrumented tracking range to increase confidence in this algorithm.

3.5   Discussion

3.5.1   Implementation Details and Limitations

The hybrid particle filter and unscented Kalman filter implementation used here is computationally advantageous, as it only tracks two state variables with particles, and it uses a single Kalman filter for tracking the motion of the vehicle. Field results from at-sea testing illustrate the performance of the approach and compatibility with the computational resources that can be available in most small AUVs. However, it does not model the non-zero covariance among the velocity, heading, and position states, and the Kalman-estimated state updates never incorporate pseudorange data. Given greater computation capability in the future, better estimates might be found by converting the partitioned integrating filter into a marginalized (Rao-Blackwellized) particle filter or changing the partitioning such that more state variables are tracked by the particle filter.

This choice of partition in state variables also allows the vehicle heading and velocity control inputs to the particle filter to be generated by another sensor fusion process in the vehicle, such as a separate INS or the internal navigation algorithm. This is advantageous when only

processed sensor data is readily accessible in the AUV, and available sensor measurements may be delayed or decimated.

Although the phase tracking technique generates a new phase estimate for each symbol in the received packet, averaging and decimation is done to reduce the data output rate from the phase tracker. This process reduces the computational load by limiting the number of measurement updates performed by the particle filter. Furthermore, this system is designed for eventual real-time implementation where the phase estimates will be provided by the Micromodem-2 to the computer running the navigation filter, and the communication throughput between these two devices is limited.

Additionally, measurements are gated for kinematic consistency and to avoid numerical effects associated with very small integration time steps.

Although this navigation method does not require that velocity over ground measurements from a DVL to be continuously available, it does require a reasonable measurement or estimate of velocity over ground for the duration of a received packet. In the absence of this data, there is an inherent unresolvable ambiguity between the velocity over ground and the possible position tracks. Practically, this implies that the DVL must have continuous bottom lock, or the current must be sufficiently stationary that velocity through water measurements are sufficient to form accurate velocity over ground estimates at the time acoustic communication packets are received.

3.5.2 Error in pseudorange measurement

Several significant sources contribute to error in the range measurement, including environmental uncertainty and timing accuracy. Timing errors in the phase measurement generate distance errors in the pseudorange measurement.

We use a single, measured value for the sound speed in the medium. This assumption is reasonable when operating over short ranges, but it would require propagation modeling to use the phase tracking technique in more challenging environments. A fractional error in sound speed corresponds to an error in range as,

$$e_{range} = \frac{\bar{c}_{used} - \bar{c}_{actual}}{\bar{c}_{actual}} \, \rho \tag{29}$$

where ρ is the actual range between the source and receiver, and $\bar{c}$ is the average sound speed along the path.

Any mismatch in sampling clock rate between the transmit and receive system will appear as a Doppler shift in the data. This offset propagates to range as

$$e_{speed} = c \frac{f_s^{receiver}}{f_s^{source}} \tag{30}$$

$$e_{range} = e_{speed} \, t \tag{31}$$

Where t is at most the duration of the packet. In the system used for the experiment, the sample clock accuracy is at worst ±20ppm, such that the maximum possible fractional difference between the source and receiver clock frequency is 4E-5. Using typical values for sound speed, this error corresponds to a maximum Doppler velocity error of 6 cm/s, and an accumulated range error of about 20 cm over the course of a packet. This error does not accumulate beyond the duration of a single packet.

The time-of-arrival estimate is affected primarily by the relative drift of the real-time clock in the system, which is accurate to ±2ppm on the Micromodem-2 [59]. This corresponds to range error as

$$e_{range} = c \, \alpha_{rtc} \, t \tag{32}$$

Where α_{rtc} is the drift rate of the real-time clock (bounded by the accuracy of the real-time clock) and t is the time since the real-time clock was last synchronized with a reference. Practically, the clock is synchronized to GPS time each time the vehicle surfaces. For example, for each hour that the vehicle has been submerged, the worst-case range error from this source is about 10 m.

Both the mismatch in sampling rate and real-time clock can be mitigated using a highly-stable and accurate clock, such as a chip-scale atomic clock [86]. The real-time clock drift can be mitigated using a more accurate real-time clock, such as a SEASCAN [64].

Motion of either the vehicle or the transmitter that is not tracked by the model contributes directly to error in the navigation result. For example, if the transmit transducer is moving and that motion is not characterized, the changing range between the source and receiver appears as pseudorange error. Additionally, the kinematic model used may fail to accurately describe vehicle motion in highly-dynamic conditions, where the kinematic assumptions might not hold. Once integrated, this will contribute to position error in the estimates.

3.5.3 Possible Extensions

In this paper, an algorithm for position estimation using phase measurements of acoustic communication signals is described, and experimental results are shown with a single transmitter at a fixed location and a moving receiver. This method is readily extended to the case of multiple transmitters and receivers. There is no limit imposed by the algorithm to the number of source-receiver pair phase measurements incorporated in the particle filter update. Although the transmitter was fixed and the moving platform hosted the receiver in this experiment, the algorithm operates symmetrically, and these roles could be reversed.

A less trivial extension would involve both a moving transmitter and receiver. While the fundamental approach remains the same, experimentation is required to determine how much kinematic information about the movement of the source must be transmitted to the receiver to generate useful position estimates.

3.6 Conclusions

A novel synthetic baseline navigation technique has been developed and demonstrated at sea. Analysis of experimental results shows that the use of phase measurements from received acoustic communication packets will improve position estimates over those made using only a single one-way travel time measurement per packet. Furthermore, this technique can generate position estimates without using one-way travel time measurements, which are unavailable without synchronized transmitter and receiver clocks.

These benefits are realized using a modest amount of additional processing applied to existing signals measured by existing sensors. Therefore, this navigation technique is suitable for integration on production and experimental AUV platforms.

3.7 Acknowledgment

This chapter, in full, is a reformatted reprint of material as it appears in the Journal of the Acoustical Society of America, 2019. The dissertation author was the primary investigator and author of this paper: E. Gallimore, M. Anderson, L. Freitag, and E. Terrill, "Synthetic baseline navigation using phase-coherent acoustic communication signals," *Journal of the Acoustic Society of America*, In Press 2019.

4 Magnetic Survey and Autonomous Target Reacquisition with a Scalar Magnetometer on a Small AUV

A scalar magnetometer payload has been developed and integrated into a two-man portable autonomous underwater vehicle (AUV) for geophysical and archaeological surveys. The compact system collects data from a Geometrics micro-fabricated atomic magnetometer (MFAM), a total-field atomic magnetometer. Data from the sensor is both stored for post-processing and made available to an onboard autonomy engine for real-time sense and react behaviors. This system has been characterized both in controlled laboratory conditions and at sea to determine its performance limits. Methodologies for processing the magnetometer data to correct for interference and error introduced by the AUV platform were developed to improve sensing performance. When conducting seabed surveys, detection and characterization of targets of interest are performed in real-time aboard the AUV. This system is used to drive both single- and multiple-vehicle autonomous target reacquisition behaviors. The combination of on-board target detection and autonomous reacquire capability is found to increase the effective survey coverage rate of the AUV-based magnetic sensing system.

4.1 Introduction

A micro-fabricated atomic magnetometer (MFAM) [87], [88] has been integrated in a small, two-man portable autonomous underwater vehicle (AUV, the REMUS 100 [6]) and fielded to perform geomagnetic surveys and target detection surveys searching for underwater World War II-era archaeological sites. The system is constructed as a modular payload that is rigidly attached to the nose of the AUV (i.e., it is not towed). It has seen extensive deployment

under many different ocean environments at sites near San Diego (USA), Papua New Guinea, Kiska (Alaska, USA), and Palau.

The integrated system takes advantage of the high (1 kHz) sampling rate of the MFAM and digital signal processing routines were developed to overcome and compensate for interference from the AUV platform. Unique to the approach presented is a signal processing chain that is designed such that it can operate in real-time on an embedded computer in the AUV.

When surveying for discrete magnetic targets (versus wide area geophysical surveys), a real-time target detection and classification algorithm are run on-board the AUV. The detector and classifier then drive autonomous behaviors that improve ability of the vehicle to discriminate and localize targets, significantly reducing false-positives and increasing overall survey efficiency. Furthermore, data on targets that satisfy classification criteria can be relayed acoustically to other vehicles to drive multiple-vehicle, cooperative autonomous target reacquisition.

4.2 Background

4.2.1 Marine Magnetometers

Marine magnetometers have seen widespread use for geophysical studies, archaeology, unexploded ordinance (UXO) and mine detection, and navigation. Although they are often deployed as ship-towed instruments, some deployments have been have been conducted with a variety of AUVs, such as the REMUS 600 [89], [90], Bluefin 12 [91], [92], Iver2 [93], Gavia [94]–[96], Sentry [97], and the Autonomous Benthic Explorer (ABE) [98], [99]. In several AUV deployments, the magnetometer package was towed to physically separate the sensor from the AUV [93], [96], [100]. (Many AUVs include a low sensitivity vector magnetometer that is used

as a compass. The magnetometers used as compasses in most AUVs are not sensitive enough to be used for the applications described here. For the purposes of this discussion, we use "magnetometer" to describe sensitive instruments useful for geophysical exploration and target detection.)

Many different sensors have been developed to measure magnetic fields. Broadly, they can be categorized by whether they make scalar or vector measurements [101]. Vector magnetometers require calibration. Therefore, when a vector magnetometer is used to sense small absolute field changes, they are typically used in a system that also incorporates a scalar magnetometer to assist in calibration [94].

Scalar magnetometers that measure the Larmor frequency provide an absolute field measurement with no temperature dependence or drift, and do not require calibration. They are well-suited to detecting small changes in the magnetic field on moving platforms, where small platform orientation changes generate changes in the vector components of the field that are difficult to separate from the signal of interest when using vector magnetometers [101].

Research at the U.S. National Institute of Standards and Technology (NIST) and subsequent work funded by the Defense Advanced Research Projects Agency (DARPA) and the Strategic Environmental Research and Development Program (SERDP) led to the development of a small, low-power cesium vapor magnetometer: the Micro-Fabricated Atomic Magnetometer, or MFAM [87], [88], [102], [103]. The MFAM provides a total-magnetic-field measurement via optical measurement of the Larmor precession frequency of excited atoms in the vapor chamber. As a result, the sensor requires no in-field calibration. Additionally, it samples the magnetic field at a high rate (1 kHz).

This device has been commercialized by Geometrics, Inc., and the size and power consumption of this instrument make it suitable for integration on a small AUVs.

4.2.2 Magnetic Target Detection

Scalar magnetometers can be used to identify magnetically-susceptible material by measuring its interaction with the geomagnetic field. The induced magnetization generates a distortion in the ambient field that can be detected. The magnitude of the distortion is governed primarily by the magnetic susceptibility, amount of material, and the geometry of the object or material. When searching for compact ferrous objects, this distortion can be approximately modeled as a point-source magnetic dipole in the far field, and the resulting field strength falls off with distance cubed (r^3).

When adequate survey data are available and a dipole source model is appropriate, some properties of the source may be inferred. Much of the work applied to magnetic dipole sensing has been directed at the detection of unexploded ordinance (UXO) (e.g. [104]). An overview of conventional techniques to perform this inversion for magnetic targets is given in [105], which describes both iterative (least-squares fitting) techniques and also a "pattern recognition" approach using template signals that is similar to the detection and classification scheme developed in this work. [106] describes a real-time capable least-squares fitting approach for classifying gradiometer data. Wavelet analysis has also been successfully employed for target parameter estimation [107]. These techniques are well-suited to characterizing small dipole targets.

The work herein builds on established, classical techniques to enable effective real-time operation using the computing resources that might reasonably be deployed inside a small AUV.

4.2.3 Autonomy

Sense and react autonomy with AUVs has been described for a variety of scientific applications (e.g. [31]–[33], [39], [108]), but fewer seabed survey applications exist. An early example from the NATO Undersea Research Centre (NURC) used a team of two surface vehicles to identify and reacquire mine-like objects [109]. This system used a robotics framework named MOOS-IvP [110] as an autonomy stack, and transmitted sonar imagery taken by a survey vehicle in real time to human operators, who then identified targets of interest. A second vehicle then reacquired those targets. Mine-like objects detected in sidescan sonar were automatically reacquired using the same vehicle in [46]. Recently, archaeological survey with multiple AUVs has been addressed in simulation, using a team of a fast, "survey" vehicle and a hover-capable "inspection" vehicle [21]–[23].

The authors are not aware of any prior work describing real-time detection and autonomous reacquisition of magnetic targets using both single and multiple vehicles, as described in this work.

4.3 Vehicle Integration

AUVs provide stable platforms that are capable of precise navigation and are generally well-suited to underwater survey applications. However, as with many moving platforms, the AUV itself is magnetic and generates electromagnetic fields due to propulsion motors, control servos, and electronic systems. In most ship-based surveys, the effects of platform noise are mitigated by towing the sensor at large distances from the vessel, so that these effects are minimized [111, pp. 90–91]. Towing is possible with an AUV (e.g. [93], [96]), but it carries substantial drawbacks: a towbody complicates vehicle deployment and recovery, presents a snag

hazard when towing near the seabed, and hampers vehicle mobility, response, and turn radii. Thus, motivation existed to develop a sensor payload mounted to the front of the vehicle (Figure 4.1, Figure 4.2). This positions the sensor as far as possible from the vehicle thruster, which is a brushless DC electromagnetic motor. Additionally, the vehicle was modified to remove as much ferromagnetic material as possible, by replacing steel fasteners and components with titanium and aluminum. These modifications are minor when compared with earlier efforts to create a non-magnetic AUV [112].

The MFAM consists of two sensor heads attached with cables to an electronics module. These are incorporated in a pressure housing (Figure 4.2) along with custom interface electronics that process the signals from the MFAM and pass the data to a payload processing computer inside the vehicle using an Ethernet interface. This interface is fast enough to capture data at the full 1 kHz sampling speed of the sensor. The total power draw of the system in operation is approximately 8 W.

Figure 4.1: Sensor system in long housing attached to REMUS 100 AUV.
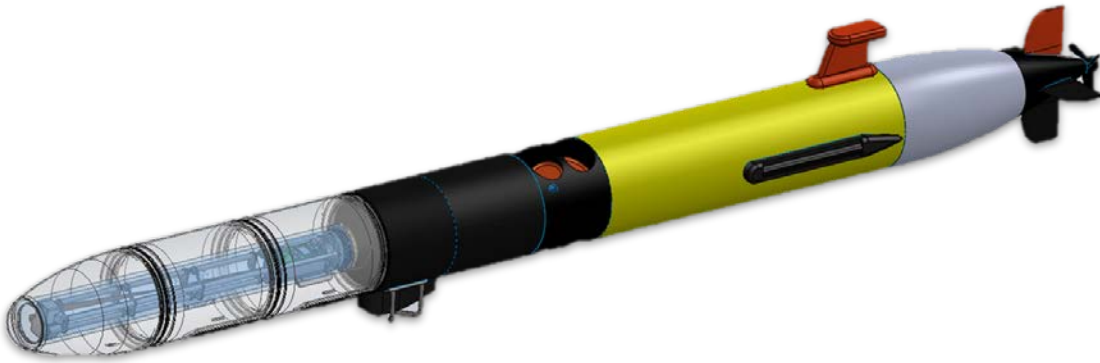
Figure 4.2: Modeled cutaway showing MFAM pressure housing inside flooded section.

The MFAM is controlled by a computer in the AUV that is dedicated to sensor processing and high-level autonomy. This computer runs a custom software suite based on the Robot Operating System (ROS) [47] that logs data from the MFAM as well as navigation and status information from the AUV [113]. This system enables both real-time processing of magnetic data and also post-processing with complete knowledge of the vehicle state.

4.4   Heading error

Despite being a scalar, total-field sensor, the MFAM is sensitive to orientation. First, there is a "dead zone" region where the sensor is not able to measure the magnetic field magnitude. This occurs when the field vector is aligned with the optic axis of the MFAM sensor [88], [114]. Outside the dead zone, the MFAM is largely insensitive to the relative orientation of the incident magnetic field vector, but it does exhibit some intrinsic heading error. To mitigate this, two matched sensor heads are incorporated in the MFAM. The heading error of each sensor in the pair is strongly correlated, so the heading error can be mitigated by physically placing the

two sensors next to one another, with one rotated 180 degrees around the optic axis. Taking the

average value of the two sensors provides a total field value that minimizes intrinsic heading

error. A plot showing the heading error measured during sensor calibration is shown in Figure

4.3.

Figure 4.3: Intrinsic heading dependence of MFAM sensors. This corresponds to rotation in
the azimuthal plane with the sensors mounted in a typical configuration on the AUV. The gaps
in the traces correspond to the dead zone of the sensors, where no measurements are possible.
Measured values are in nanoTeslas (nT). Figure courtesy Geometrics, Inc. Used with
permission.

The two sensors are typically mounted such that the optic axes (and therefore the dead

zone) are aligned port-starboard; transverse to the vehicle. This allows the vehicle to accurately

sense the magnetic field at any location on earth without rearranging the MFAM sensors,

provided the vehicle heading is roughly aligned with either magnetic north or south. As the

vehicle can maneuver, adjusting survey geometry to satisfy this constraint is often tractable and

simpler than rearranging the sensors. When operating in areas where the magnetic field is nearly

horizontal (such as Palau), the entire magnetometer module can be easily rotated 90 degrees,

such that the optic axis is oriented up and down (aligned with the gravity vector), and the field

can be accurately sensed regardless of vehicle heading.

Although the aforementioned technique mitigates the intrinsic heading error associated

with the MFAM payload itself, the system when installed on the AUV still exhibits heading error

due to interaction between magnetically susceptible material on the AUV and the earth field

(induced magnetization) as well as any permanent magnetization of AUV components.

Furthermore, despite removing as much ferrous material from the vehicle as possible, magnetic

disturbances from the electromagnetic motors that drive the thruster and control surfaces remain.

This will be addressed further in the next section. Figure 4.4 shows experimental results that

illustrate the total heading error on the vehicle. Notably, the heading error is most stable when

the vehicle heading is aligned with magnetic north or south, but these headings also represent the

extremes of platform heading error.

When processing data from the system, an empirical correction can be applied based on

a fit to measured heading error in an area. A calibration mission, during which the vehicle circles

in the middle of the water column as far from likely disturbances as possible, can be run to obtain

measurements of the platform heading error for all vehicle headings. The measured heading

error depends not only on the vehicle heading, but also the pitch and roll of the vehicle. However,

the vehicle pitch and roll are stabilized during operation and typically don't exceed +/- 3 degrees

when following a survey line free of obstacles, so calibration over vehicle heading is sufficient in practice.
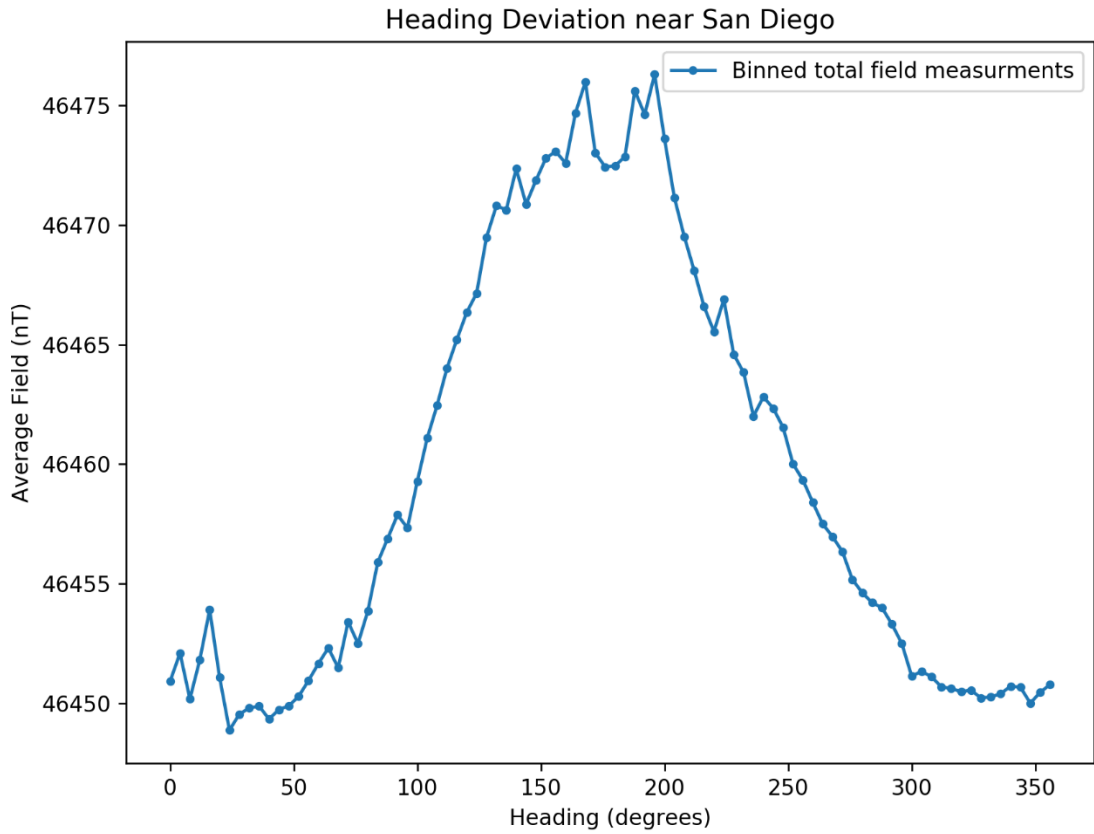
Figure 4.4: Measured heading dependence of total magnetic field measurements with AUV operating mid-water column away from targets near La Jolla, CA. This uses the average value measured by two MFAM sensors mounted in opposing orientations such that the heading error of the sensor pair is minimized with the optic axis of both sensors horizontal. Note that the heading error is most stable in magnetic north and magnetic south orientations. The measured total field over a range of headings (approximately 46450 nT to 46475 nT) is comparable to values from the International Geomagnetic Reference Field (IGRF) model, 46181 nT, and the World Magnetic Model (46157 nT).

4.5   Platform Noise

Although mounting the magnetometer on the nose of the vehicle offers substantial operational advantages, it does expose the sensor to electromagnetic interference from vehicle

systems. The MFAM samples at 1 kHz, which is found to be sufficient to isolate and identify many sources of interference in the frequency domain. The signals of interest for the target detection and geophysical exploration applications described in subsequent sections fall below 2.5 Hz, so much of this noise can be removed from the processed signal via frequency-domain filtering.

To establish baseline noise performance of the MFAM without the AUV, it was tested in the Scripps Electromagnetic Research Facility (EMRF), which is a non-magnetic building designed for magnetic testing and evaluation. The data from this experiment show significantly higher noise values across the spectrum than the manufacturer-published sensor noise floor (Figure 4.5, blue and red lines). Some of this is easily explained (there are strong peaks at harmonics of 60 Hz, corresponding to the frequency of the electrical mains supply to the building), but the remainder is not easily attributed to a particular noise source. The sensor may have been affected by electromagnetic noise generated by the computer used for logging data (although it was placed several meters away to mitigate this effect) or from the electronics used to interface with the MFAM. The MFAM was powered using a battery for this experiment, but several of the voltage rails used by the interface electronics were derived from battery voltage by switching power supplies.

The baseline noise of the sensor alone was compared with noise spectra collected while the vehicle was operating. Two different instrument housings were used: one that positioned the MFAM sensors approximately 56 cm forward of the vehicle forward endcap, and one that positioned the sensors 81 cm forward of the endcap. Similar missions were run in mid-water-column away from identified magnetic targets to gather data in both configurations. For these runs, the vehicle operated its acoustic Doppler current profiler (ADCP) and acoustic navigation

and telemetry systems but was not running sidescan sonar or other sensors. Only data recorded while the vehicle was stably navigating north-south tracklines were used for analysis. The results are shown in Figure 4.5 (green and orange traces). Using the longer housing (that provides greater distance between the sensors and the body of the vehicle) improves noise performance across the spectrum. However, using the shorter housing improves the maneuverability and handling of the vehicle. Both systems have been used operationally, with the shorter, more maneuverable unit preferred when operating in high sea state or strong currents.

For comparison, data collected by a Geometrics 858 magnetometer system towed by a small boat in Palau is also shown in Figure 4.5. The towbody did not maintain good altitude control during this data collection, which likely contributes to strong low-frequency signals. The 858 system sampled at 10Hz, so spectral information above 5Hz is not available.
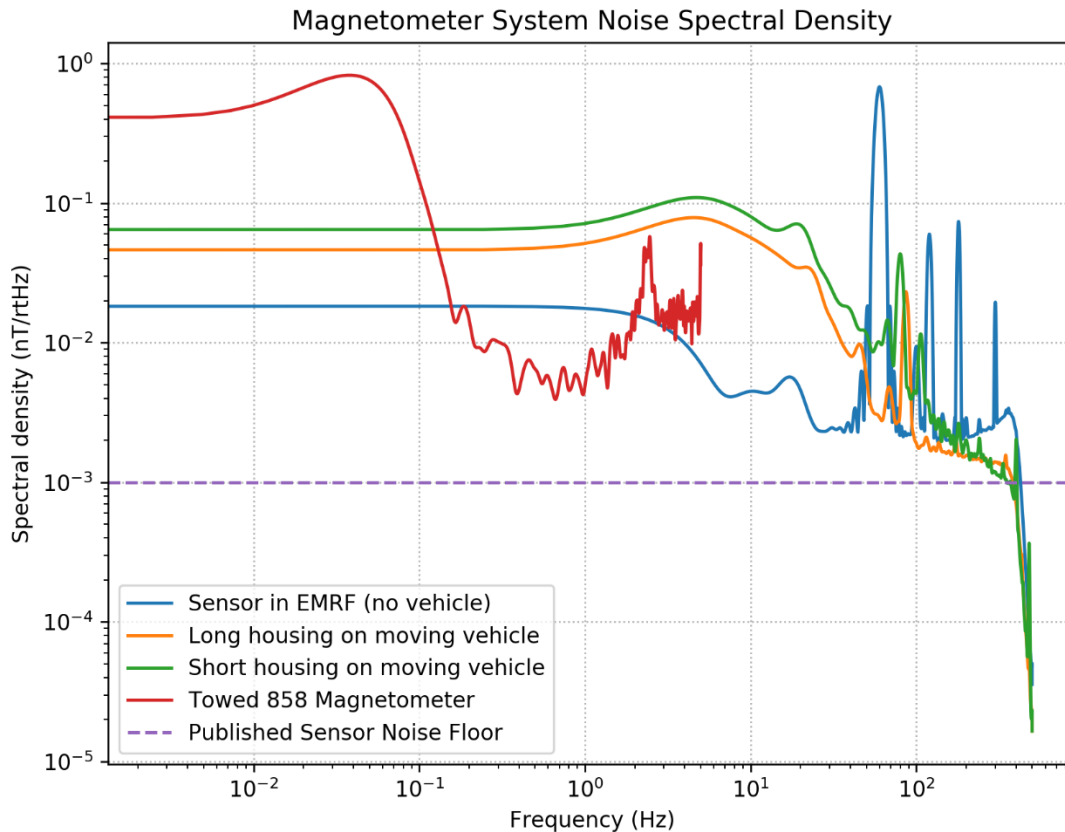
Figure 4.5: Variance spectral density of measured noise collected by magnetometer system in different configurations. The dashed line shows the published noise density value in the MFAM calibration sheet. "Sensor in EMRF" shows data collected in the Scripps Institution of Oceanography Electromagnetic Research Facility, which is a non-magnetic structure located in a relatively isolated part of the campus. The strong peak at 60Hz and harmonic peaks are due to the mains supply to the building, which was turned on during the test, although the sensor was powered using a battery. Data from the moving vehicle was taken while the vehicle was travelling at approximately 3kt far from external magnetic targets or disturbances. The short housing places the MFAM sensors 22 inches forward of the vehicle's front endcap, and the long housing places the sensors 32 inches forward of the endcap. A comparison from a ship-towed Geometrics 858 magnetometer is shown in red. The towed system sampled at 10 Hz, so no spectral data is available above that level. The strong low-frequency signal in the towed data is due to poor altitude control with the towed system.

Sidescan sonar is often used for seabed survey, and many magnetic survey missions also benefit from sidescan sonar coverage. Unfortunately, the sidescan sonar generates significant magnetic interference when operating. The acoustic center frequency of the sonar exceeds the

sampling rate of the MFAM by several orders of magnitude, and most of the observed energy is concentrated at the sonar ping rate and harmonics thereof (Figure 4.6). It is unknown how much of the observed signal is due to coupling from the acoustic transmission system and how much is due to magnetic fields generated due to impulsive current flowing in the wiring harnesses that power the sonar.
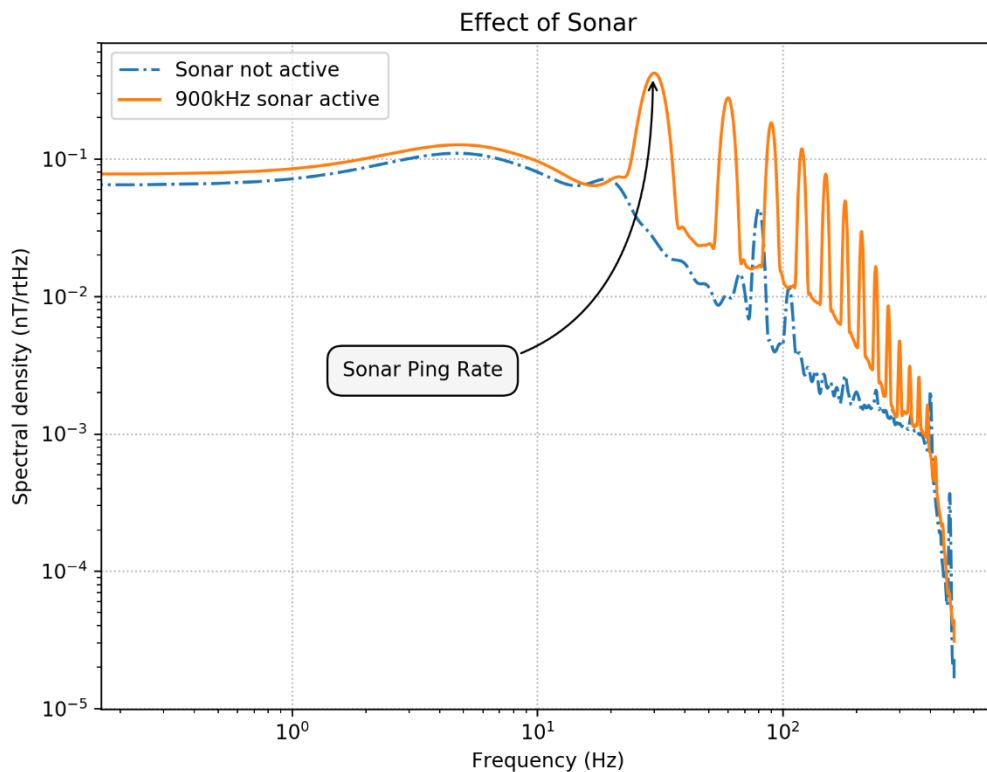
Figure 4.6: Variance spectral density of the measured signal collected by the vehicle when travelling at approximately 3kt away from magnetic targets or disturbances. Two values are shown, one with no sonar operating, and one with the Marine Sonic Arc Scout sidescan sonar operating. The sonar was pinging at approximately 28Hz and transmitting FM sweeps with 150kHz bandwidth centered at 900kHz, and the spectral peaks in the sonar data correspond to harmonics of the ping repetition rate of the sonar.

The vehicle's propulsion motor (thruster) is an eight-pole motor that uses fixed electromagnets arranged around a rotor that incorporates eight permanent magnets. Several

spectral peaks due to the thruster operation are observable in data collected from a vehicle in motion (Figure 4.7). The overall thruster rotation rate corresponds to a peak in frequency (1200 rpm corresponding to 20 Hz, for example). Peaks are also present at eight times the rotation frequency, corresponding to the rotation of the eight permanent magnets in the thruster shaft. The observed magnetic signal is a combination of the magnetic fields of the permanent magnets on the rotor, the generated fields of the stator windings, and the varying current flowing though the wiring that powers the motor.

Increasing the average rotation rate of the thruster from 1200 rpm to 1600 rpm shifts the frequency content of the noise spectrum but does not significantly affect the overall noise variance. Furthermore, the data suggest that there is no advantage to operating in a fixed rotation rate mode rather than a constant speed-over-ground mode (where thruster rotation rate varies depending on ocean currents). The is no significant increase in the overall noise variance when operating in constant speed-over-ground mode.
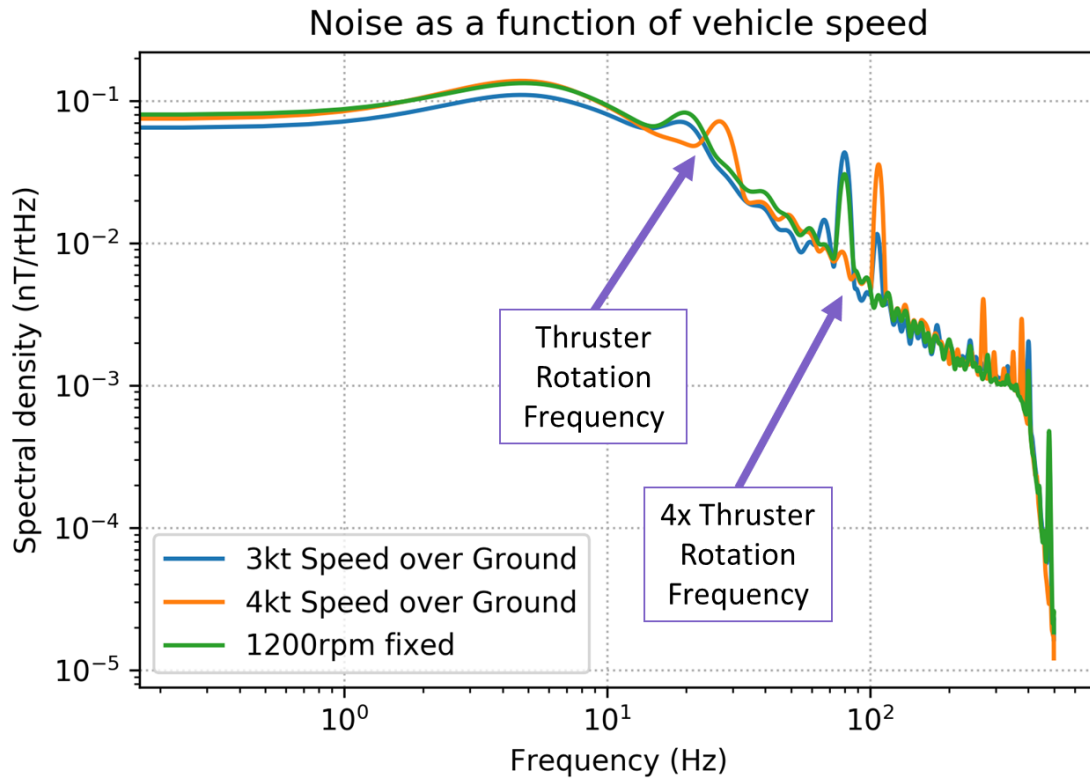
Figure 4.7: Variance spectral density of the measured signal collected by the vehicle when travelling at different speeds far from magnetic targets or disturbances. The vehicle operated in several modes. First, in constant speed over ground at 3kt or 4kt, where the vehicle's doppler velocity log (DVL) provides feedback such that the propeller speed is controlled to maintain constant speed over ground even in the presence of currents. Second, with the thruster running at a fixed rotational speed of 1200 rpm, which results in a velocity through water of about 3kt on this vehicle. All these measurements were made with the sensor installed in the short housing.

The vehicle includes an acoustic navigation and telemetry system that intermittently transmits by applying a modulated high voltage to a ceramic transducer located toward the front of the vehicle. When this system is transmitting, it generates an offset disturbance of several nT in the magnetic data that remains roughly constant while the system is transmitting. If necessary, this can be controlled by limiting the transmission rate of the acoustic modem, and the disturbance is filtered out by some of the processing algorithms described in subsequent sections.

As the transmission times are logged, it would also be possible to individually correct the offset for each transmission in post-processing, but this is not currently performed.

In summary, the AUV platform generates significant high-frequency magnetic noise (above 2.5Hz) due to the proximity of electrical motors and acoustic transmission systems. Since the MFAM samples at 1kHz, this noise can be removed with digital filtering. In contrast, the Overhauser magnetometers sometimes used in tow-behind-AUV systems to date [93], [96] sample at a maximum of 4Hz [115], and the atomic magnetometer used in [94], [95] samples at a maximum of 20 Hz. With those systems, all noise above the Nyquist frequency will be aliased, and it cannot be digitally filtered.

4.6   Applications and Results

An AUV equipped with the MFAM payload has been deployed for numerous surveys, allowing the characterization of the payload in different operating environments. Basic geomagnetic surveys have been conducted, with engineering evaluation of the magnetometer system as a primary goal. The system has also been operationally fielded during expeditions in waters near San Diego, Papua New Guinea, Alaska, and Palau, where it has identified and characterized targets of archaeological interest. These surveys typically follow a "find-fix-finish" paradigm [4]. In the initial "find" phase, large areas are surveyed with long-range, low-resolution sensors, such as low-frequency sidescan sonar. The "fix" phase follows, where high-resolution, short-range sensors reacquire targets identified during the "find" phase to gather additional high-fidelity data and accurately localize and characterize the target. In the "finish" phase, the site is identified and documented as completely as possible, often using human divers or remotely-operated vehicles.

The magnetometer system is typically employed during the "fix" phase to discriminate geological targets from anthropogenic targets containing ferrous metal, but it can also be used for the "find" phase, particularly if searching for a partially-submerged target or working in an area with excessive sonar clutter.

4.6.1 Geomagnetic Survey

To evaluate the suitability of the system for geophyical work, a seabed survey was conducted offshore La Jolla, CA near a local geologic formation known as Dike Rock [116]. This system is uniquely suited for near-shore operation, as the vehicle does not tow a sensor and therefore maintains good maneuverability.

To make effective geomagnetic measurements, the data are post-processed to mitigate the platform effects (Figure 4.8). First, the values output from the two MFAM sensors are averaged to generate a measurement with the MFAM sensor heading error mitigated, as described above. Next, a low-pass filter with a cut-off frequency of 2.5 Hz is applied, which corresponds to a spatial filtering of all signals with scales shorter than 0.6 m when the vehicle is travelling at 1.5 m/s. These nominal filter settings were found to reject much of the noise associated with the vehicle thruster. Next, data are masked during turns (by rejecting heading rates greater than 2 degrees per second) to reject transient signals that appear due to attitude changes and heading error. An empirical heading error correction is applied using data from a calibration run, as described earlier. Finally, if the mission is sufficiently long, or if there is a desire to compare data over long durations, corrections for diurnal and/or secular variation are applied. If there is a desire to apply these corrections, it may be advantageous to record data with a fixed magnetometer to identify appropriate variation values (see e.g. [111, p. 75]).

Figure 4.8: Flowchart showing summary of processing steps when using the AUV-based magnetometer to conduct geomagnetic surveys. This preserves low-frequency total field information.
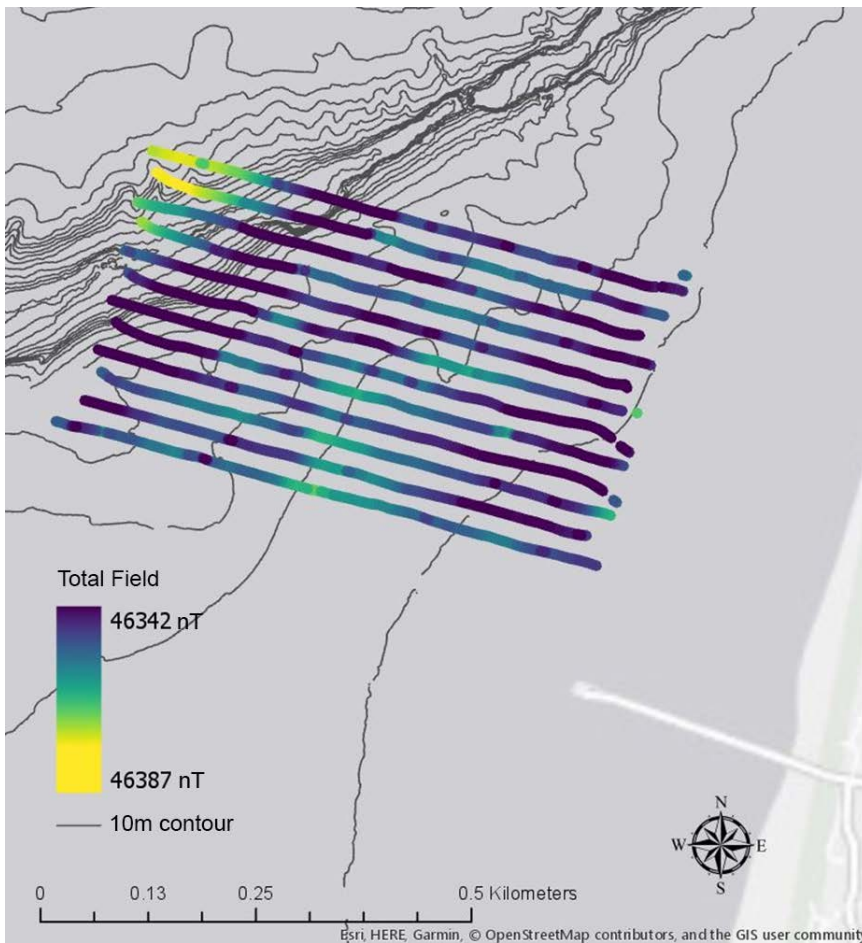
Figure 4.9: Map of total magnetic field sampled offshore of Dike Rock near La Jolla, CA. These data have not had diurnal or secular variation corrected. Scripps pier is visible in the lower right of the figure.

The total geomagnetic field measurements made by the MFAM on the AUV have been validated against values from the Enhanced Magnetic Model [117]. Table 4.1 shows values obtained at several geographically disparate locations.

Table 4.1: Comparision of measured total field to EMM values

Location	MFAM Measurement (Average)	Enhanced Magnetic Model (EMM2017)	Difference
San Diego	46532 nT	46267 nT	265 nT (0.57%)
Kiska, AK	49675 nT	49756 nT	-81 nT (0.16%)
Hansa Bay, PNG	40354 nT	40206 nT	148 nT (0.37%)

4.6.2 Magnetic Anomaly Detection

When searching for magnetic targets or anomalies, small-scale relative changes in the measured field are of greater interest than the absolute magnitude of the field. Thus, the magnetic gradiometer, which measures magnetic field variation over distance, is an important tool for magnetic search.

In practice, a pair of scalar magnetometers is often configured as a gradiometer by physically separating them. This configuration creates an instrument with directional sensitivity. In most systems, the pair of sensors is arranged such that their separation is transverse to the direction of platform motion, such that two orthogonal gradients can be calculated directly, and the vertical gradient can be estimated with physical models [118], [119]. Gradient data can be used to generate a so-called analytic signal, which is a representation of the total magnitude of the gradients in all directions. This simplifies target detection by emphasizing magnetic anomaly signals over background variations, and is widely used to identify anomalies with towed gradiometers [118], [120].

To support this common configuration as a one-dimensional gradiometer, the MFAM payload includes two sensor heads that are attached to a single electronic interface. However, the installation of the magnetometer sensor heads on the REMUS 100 is practically limited by the vehicle size. The largest transverse separation possible without incorporating a mechanical superstructure that will negatively affect vehicle dynamics is approximately 20 cm, almost an order of magnitude smaller than a typical, towed transverse gradiometer [118]. Furthermore, configuring the two MFAM sensor heads as a gradiometer would prevent them from being coincidentally located so that they can be averaged to minimize heading error.

However, the AUV is capable of precise navigation and continuously measures its velocity over ground using a Doppler velocity log (DVL). (In the REMUS 100, the DVL function is performed by a downward-looking ADCP equipped with specialized firmware to measure speed over the seabed using reflections from the bottom.) Therefore, it is possible to accurately calculate along-track gradient from data collected using a single sensor.

There are many possible filtering operations that can be used to calculate along-track gradient measurements, which can be used for anomaly detection. The general processing chain involves some smoothing or low-pass filtering to remove high-frequency noise and differentiating, with appropriate critical frequencies selected for the speed of the vehicle and the size of the target. To identify anomaly targets, the gradient magnitude is taken. To visually identify dipole targets, which often generate more than one peak in gradient magnitude, a dilation filter with an appropriate window size joins adjacent signal peaks. Then, an erosion filter is used to sharpen the peaks. Vehicle kinematic information can be used to mask invalid data. A summary of the implementation of this process is shown in Figure 4.10.

The inherent high-pass filtering involved in the differentiation removes signal due to secular or diurnal variation and reduces clutter from large geophysical features.

This processing can run in real-time on the vehicle. It has not been used to drive autonomous behavior in its current implementation, due to the greater suitability of the dipole target detection algorithm described in the next section for all surveys to date. However, the output of the synthetic gradient processor can be compared with a detection threshold to provide on-board anomaly detection.

Figure 4.10: Summary of synthetic gradient processing used to generate gradient intensity values that highlight magnetic anomaly targets

Two confirmed targets associated with aircraft wrecks are readily observable in the output of this processing chain when applied to data from a magnetic survey conducted near Hansa Bay, Papua New Guinea (Figure 4.11).
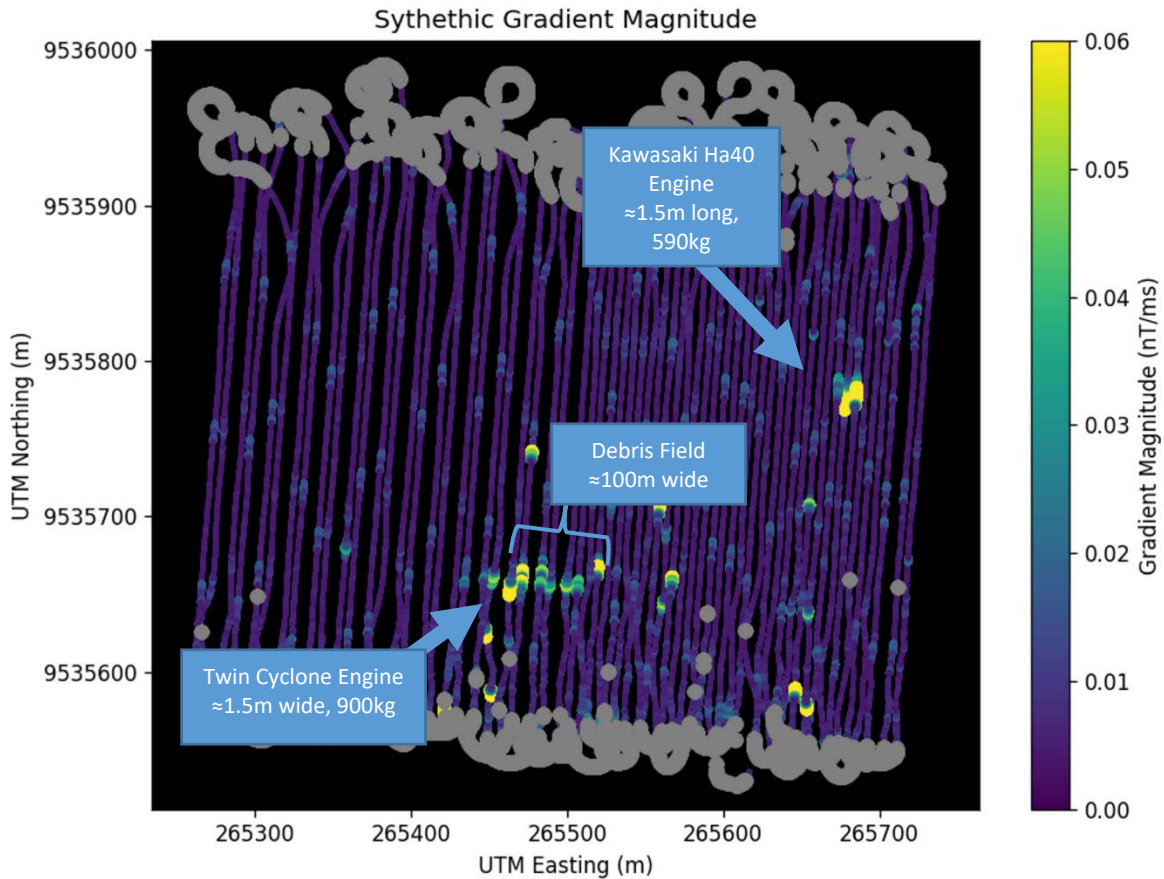
Figure 4.11: Processed synthetic gradient data from systematic magnetic survey over World War II archaeological targets near Hansa Bay, Papua New Guinea. Debris from two aircraft wrecks generates strong signatures in the synthetic gradient. Subsequent surveys with sidescan sonar, optical imagers, and divers identified the wreckage of a Japanese Ki-61 aircraft with a Kawasaki Ha40 engine and a U.S. B-25 Mitchell aircraft with a Wright R-2600 engine visible (the second engine of this twin-engine craft was not found). These targets are highlighted in the figure. "Blanked" data that has been rejected due to a high turn rate or invalid heading rate is shown in gray. The periodic "noise" in the gradient is interference from the acoustic modem system, which is not removed by this signal processing chain.

4.7 Dipole Target Detection and Classification

4.7.1 Modeling

From a relatively small set of parameters, it is possible to model the far-field magnetic disturbance due to an induced dipole in a ferrous or paramagnetic object. Given the ambient (Earth) field vector ($\vec{B}_{earth}$) and the targets mass (m), density (ρ), and rationalized volume magnetic susceptibility (κ), the magnetic moment ($\vec{m}$) can be calculated as

$$\vec{m} = \frac{m\kappa}{\mu_0 \rho} \vec{B}_{earth} \tag{33}$$

The dipole disturbance field ($\vec{T}$) is then determined by

$$\vec{B}_{anomaly} = \frac{\mu_0}{4\pi} \left(\frac{3\vec{x}(\vec{m} \cdot \vec{x})}{|\vec{x}|^5} - \frac{\vec{m}}{|\vec{x}|^3} \right) \tag{34}$$

where μ_0 is the magnetic permeability of free space and $\vec{x}$ is a vector of points surrounding the target in Cartesian space.

The total measured field ($\vec{B}$), including both the dipole disturbance field as well as the ambient (Earth) field is given by

$$\vec{B}_{total} = \vec{B}_{earth} + \vec{B}_{anomaly} \tag{35}$$

Of these parameters, the value for the ambient field ($\vec{B}_{earth}$) can often be found using models such as the World Magnetic Model [121] or Enhanced Magnetic Model [117]. The properties of the target object (mass, density, and susceptibility) may not be known, although reasonable estimates can be made. "Rule of thumb" values are provided in [122].

The magnitude of the induced dipole moment scales linearly with target mass (equation 33). Therefore, for a given set of assumed values for magnetic susceptibility and target density,

mass can be used as a proxy for moment magnitude. This is useful when presenting data to operators and analysts who may lack intuition regarding moment magnitudes expressed in Am^2.

4.7.2 Detection

Due to the formalized analytic description of the physics describing the magnetic anomaly field, the signal corresponding to the far-field dipole disturbance magnitude can be modeled and used as a template for a matched filter. The matched filter provides significant benefit by providing signal-processing gain, effectively improving the signal-to-noise ratio (SNR) at the input to a detector. However, in almost all cases, the dipole moment magnitude (which depends on specific properties of the object in question) is not well-known.

However, analysis over simulated target properties shows that the normalized amplitude of the disturbance field is relatively stable over a wide range of target moment magnitudes, and this stability increases with distance. Therefore, targets of widely varying mass and susceptibility can be detected using a relatively small bank of matched filter templates. An example of the strong correlation between signatures from targets with two orders of magnitude difference in equivalent ferrous mass is shown in Figure 4.12.
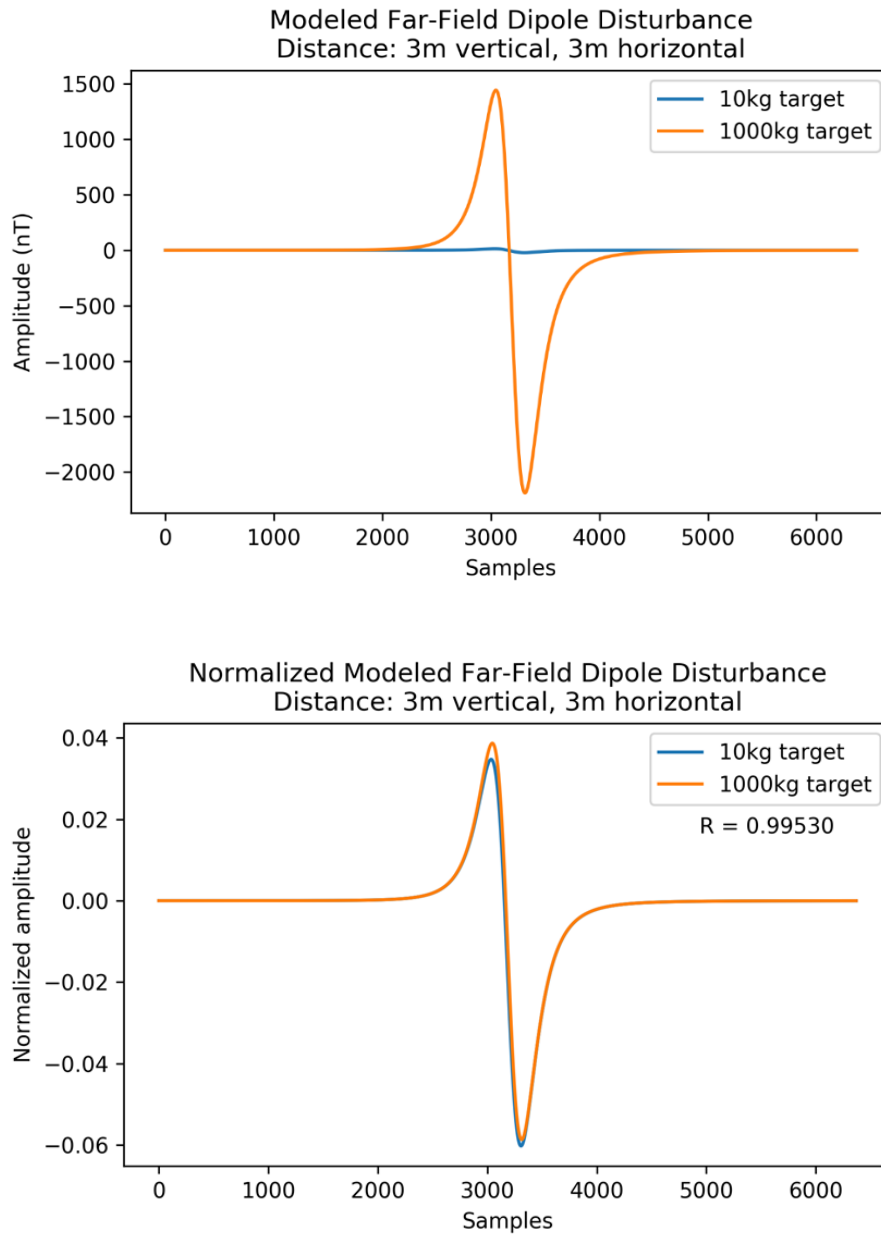
Figure 4.12: Disturbance field amplitude (top) and normalized disturbance field amplitude (bottom) for two magnetic targets with significantly different moments: 10kg and 1000kg masses with density of 8000 kg/m^3 and volumetric susceptibility of 100 (unitless in the SI system, equivalent to 8 emu/cm3 in the cgs system). This illustrates the similarity in the far field between the normalized signatures (with a Pearson cross-correlation of 0.995), which we leverage to reduce the computational load when running the detector.

The matched filter detector is found to be computationally-tractable on modern microcomputers suitable for integration on-board the AUV, which are limited in capability due

to energy and power limitations. While the computer used for sensor processing on the AUV has limited computation capability and is not capable of modeling all possible target scenarios in real-time, it has several gigabytes of RAM. This is sufficient to store results from many modeling calculations performed prior to vehicle deployment.

Accordingly, the algorithm is designed such that all the computation associated with dipole field modeling is performed at initialization time (before the mission begins), and not in real-time. The results are stored in RAM and then used repeatedly. As a result, modeled templates are not adjusted for changing vehicle kinematics; rather, the closed-loop control of the vehicle is leveraged to ensure that the vehicle maintains a consistent speed and heading that matches the assumptions used for modeling at initialization time.

Templates are generated for a range of relative target geometries at 1 meter intervals. A single moment magnitude is used to model detector templates, since the output is normalized as described above. The signal observed by the vehicle is symmetric when traveling from magnetic north to magnetic south and vice-versa, so only one disturbance field is modeled for each combination of transverse and vertical distance to the target.

In real-time during the mission, the magnetic field is sampled at 1kHz and subsequently bandpass-filtered and decimated using a series of digital filters. This removes high-frequency noise from other vehicle systems as well as any DC offset (non-time-varying component) of the total field.

Then, kinematic data from the vehicle is used to determine if the magnetic data are valid. Data are rejected if the vehicle's heading, heading rate, or speed over ground exceed threshold values. The filters are reset at the beginning of each north-south or south-north leg.

81

Valid data are processed by a matched filter (replica-correlator) bank that uses the pre-calculated values determined at initialization time as templates. The output of each matched filter element in the filter bank is a convolution of the template and the incoming signal, or the correlated power in the signal. For a given input sample and template, this is

$$T = \sum_{k=0}^{n} x_{k+i-n}\, h_k \tag{36}$$

where h is the template signal, x is the prefiltered incoming signal, n is the length of the matched filter template in samples, and i is the index of the current sample of the incoming sample.

History buffers are maintained such that multiplication operations are only performed once on each incoming sample. Additionally, a ring buffer with length equal to the group delay of the matched filters stores the vehicle state information. This is done to correctly link the vehicle state associated with a detection for use elsewhere.

A real-time windowed peak detector operates on the output of each matched filter to identify maximum values. When a peak is found that exceeds the detection threshold, a detection message is generated that includes the vehicle state information, detector SNR, an estimated target position, and a snapshot of the magnetic sample data that generated the detection.

This algorithm, as implemented, runs faster than real-time on the sensor processing computer in the vehicle with hundreds of dipole model templates (a number useful for magnetic survey). An overview of the system is illustrated in Figure 4.13.
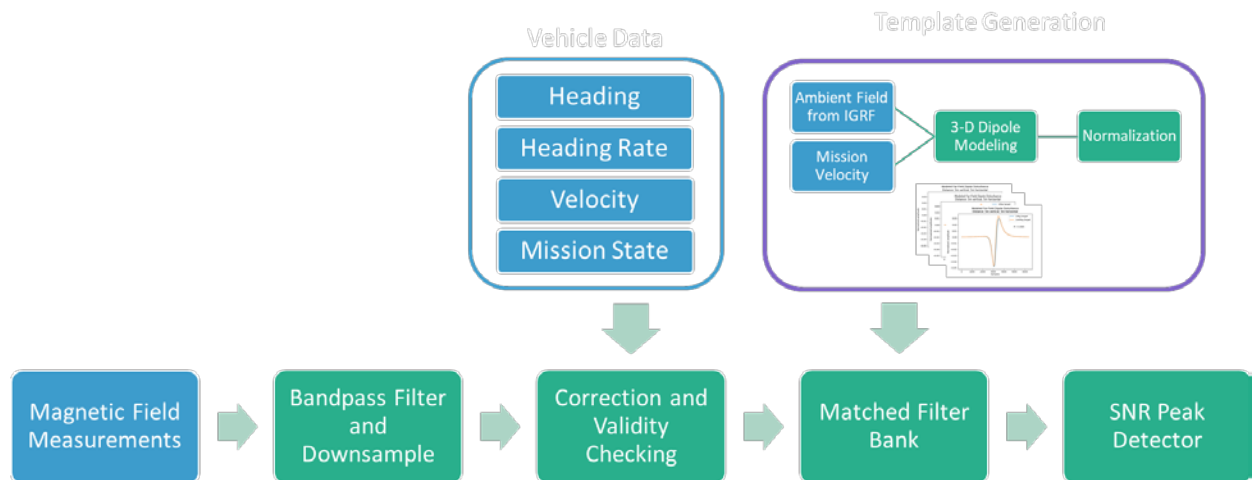
Figure 4.13: Flowchart showing real-time detector operation. The templates for the matched filter bank are precalculated once at mission start time and used repeatedly. Total magnetic field measurements are bandpass filtered to a narrow range and then the resulting signal is decimated. Filtered data are checked for validity using vehicle kinematic data prior to matched filtering. The matched filter bank calculates the correlation between the measure signal and each precalculated template. The uncorrelated signal power is also tracked using a moving average filter. Detections are generated when peaks in the matched filter output SNR (the ratio of correlated to uncorrelated power) exceed the detection threshold.

4.7.3 Detector performance

The matched filter detector used in this system detects a signal of unknown amplitude (but known sign) and unknown time of arrival. This detector lacks optimality properties, but it performs well in practice. Analytic evaluation of its performance is difficult to obtain [123, p. 333]. However, reasonable approximations can be made to estimate the detector performance, and these estimates can be used to plan optimal surveys. The estimated performance has been validated through simulation.

Performance is estimated using analytic expressions for a matched filter operating in gaussian white noise from [124, pp. 253–260], with noise amplitude equal to the standard deviation of the worst-case noise measured by the magnetometer system on the vehicle in the

configuration used for a particular survey. Worst-case noise is used to simplify and bound the problem, as the noise probability distribution is not known.

For the purpose of survey planning, a desired probability of detection is usually given. This allows determination of appropriate detection thresholds as

$$\gamma = \mathcal{E} + \sqrt{\sigma^2 \mathcal{E}} \, Q^{-1}(P_D) \tag{37}$$

Where $\mathcal{E}$ is the energy (integrated amplitude squared) of the signal, σ^2 is the noise variance, Q^{-1} is the inverse survival function, and P_D is the specified probability of detection. Detection thresholds are calculated for each matched filter in the filter bank.

The sliding-window of the detector is approximated as a series of independent trials, each of which has a duration in time equal to the noise-equivalent time of the template signal (a non-overlapping block assumption), using an expression derived from [125, p. 119]:

$$\tau_{ne} = \frac{\left(\sum_{k=0}^{n} h[k] \, dt\right)^2}{\sum_{k=0}^{n} h[k]^2 \, dt} \tag{38}$$

Where dt is the sample period, n is the length in samples of the template signal, and h is the template signal.

Since the amplitude of the dipole disturbance field falls rapidly with distance, the probability of detection is bounded by the model associated with the smallest moment magnitude and greatest distance. This is used to determine corresponding probabilities of false alarm, as

$$P_{FA} = Q\left(\frac{\gamma}{\sqrt{\sigma^2 \mathcal{E}}}\right) \tag{39}$$

Where Q is the survival function and γ is the threshold described in equation 37.

This can be used to draw receiver operating characteristics (ROC) curves for the detector, as shown in Figure 4.14, that relate probability of detection and probability of false alarm to

various ranges from the target. While ROC curves are not typically used in magnetic target detection problems, the proposed approach provides a quantitative and pragmatic framework for assessing the performance of the system.
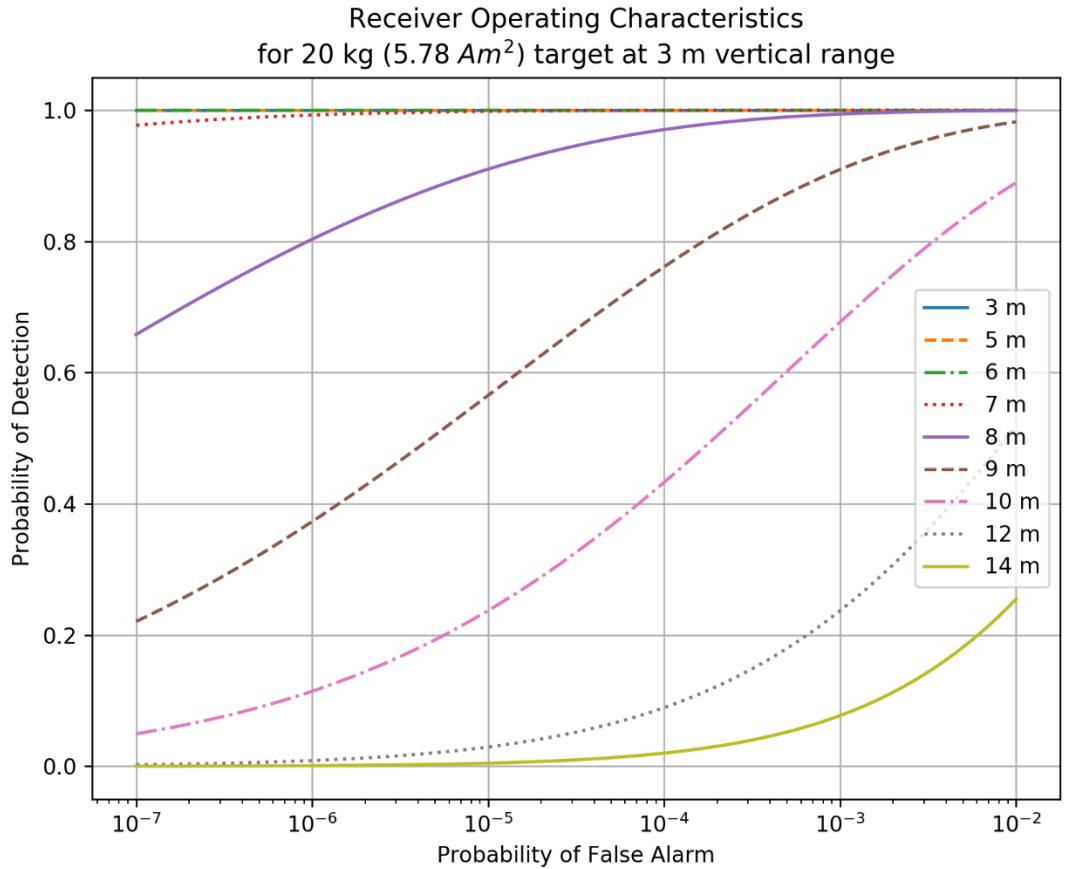
Figure 4.14: Receiver operating characteristics for matched filter detector detecting target equivalent to 20 kg steel using empirical noise data. Different curves are shown for different transverse ranges to the target, which correspond to changing signal to noise ratios (SNRs) in the measured signal.

These results can be used to plan surveys that optimize the survey area coverage rate (sometimes called "clearance rate") of the system. The area coverage rate is given by

$$\text{Area coverage rate} = (2 \cdot \text{speed} \cdot \text{range})(1 - FAR \cdot \text{cost}) \tag{40}$$

Where FAR is the false alarm rate, given by

$$FAR = \frac{\text{Probability of false alarm}}{\tau_{ne}} \tag{41}$$

The cost is the time spent on reacquire maneuvering or missions for each false detection.

Since the probability of false alarm can be found from the desired probability of detection for a target of a particular size, optimal survey geometries can be planned for each desired probability of detection. Figure 4.15 shows an example of the area coverage rate associated with a range of probabilities of detection and survey lane spacings (corresponding to transverse distance to the target). As the survey lane spacing increases, the area coverage rate increases. However, the minimum amplitude of the sensed dipole disturbance field decreases (since the sensor is farther from the target). Therefore, to achieve a desired probability of detection, the detection threshold must decrease. This increases the probability of false alarm. Since there is a time cost associated with false alarms, the increase in false alarms eventually decreases the effective coverage rate.

The survey lane spacing associated with the highest effective coverage rate can be used to optimize survey performance. As the earth field varies with geographic location, and the earth field drives the dipole disturbance field modeling, all these values must be recalculated for each area in which the system is operating.
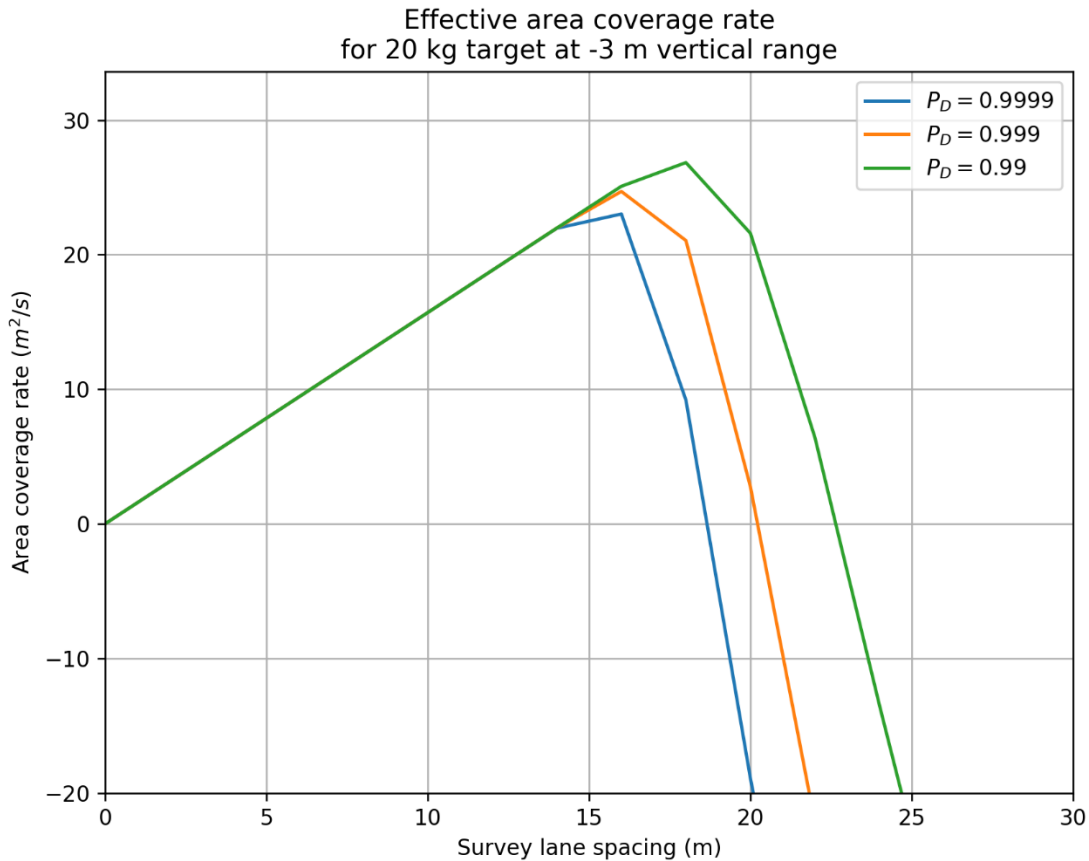
Figure 4.15: Calculated effective area coverage rates for a 20kg minimum target at a range of survey lane spacings, calculated using the earth field near La Jolla, USA. The received signal amplitude decreases with range, so lower detection thresholds must be used at longer ranges to maintain the same probability of detection. This increases the probability of false alarm, and the cost of false alarms eventually overcomes the advantage of operating at longer ranges. Lowering the required probability of detection decreases the probability of false alarm, so the sensor system can operate at longer ranges before this occurs.

4.7.4 Classifier

Each time a detection is made by the matched-filter detector, the snapshot of sampled data that led to the detection is passed to the classifier, which estimates the relative position and moment magnitude of the target. An overview of classifier is shown in Figure 4.16.
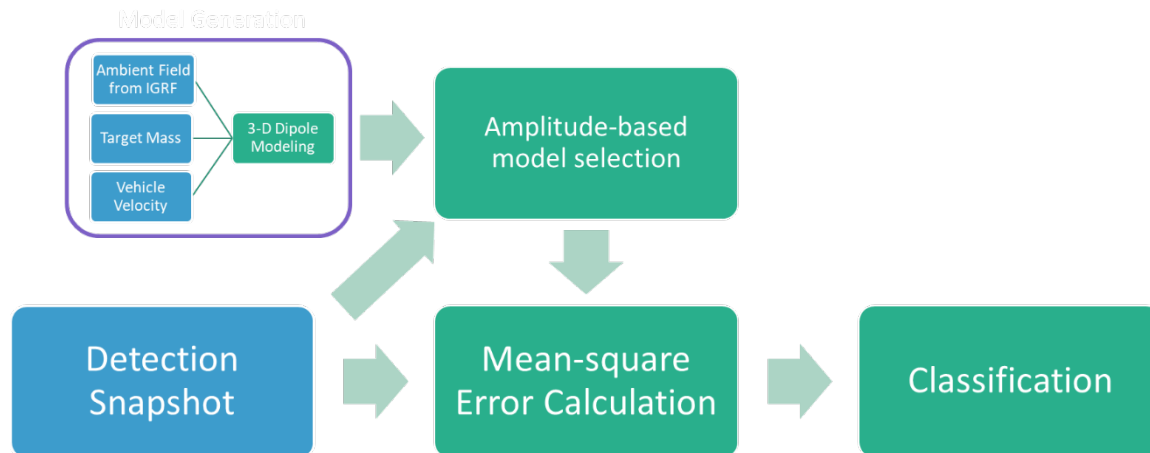
Figure 4.16: Flowchart showing classifier operation. A three-dimensional dipole model issued to generate a template library. The filtered signal associated with each real-time detection is compared against a subset of these templates, and the minimum mean-squared difference between the incoming signal and template is used to classify the relative position and magnetic moment of the target.

Like the detector, the classifier architecture is optimized to perform all modeling operations at initialization-time (pre-mission), rather than at run-time (during the mission). Three-dimensional dipole modeling is performed across a range of relative target geometries (with one-meter spacing) and moment magnitudes (masses). The range of moment magnitudes modeled depends on the expected targets of the survey, and are generated using a range of equivalent masses, typically at 5 kg or 10 kg intervals. These model results are cached in memory for real-time use in-mission. The number of model results stored varies with the expected target characteristics on a survey. Typical aircraft debris search missions use around 5000 to 10000 models, which occupy only a small fraction of the available RAM on the embedded computer in the AUV.

The classifier calculates the mean-squared error (MSE) of the difference between each template and the snapshot of measured data. In contrast to the detector, which uses normalized

templates, the classifier incorporates the moment magnitudes (masses). The parameters (mass/moment magnitude and relative position of the target) used to model the template corresponding to the lowest MSE form the classification result. An example showing a detection snapshot and the template from the corresponding classified model is shown in Figure 4.17.
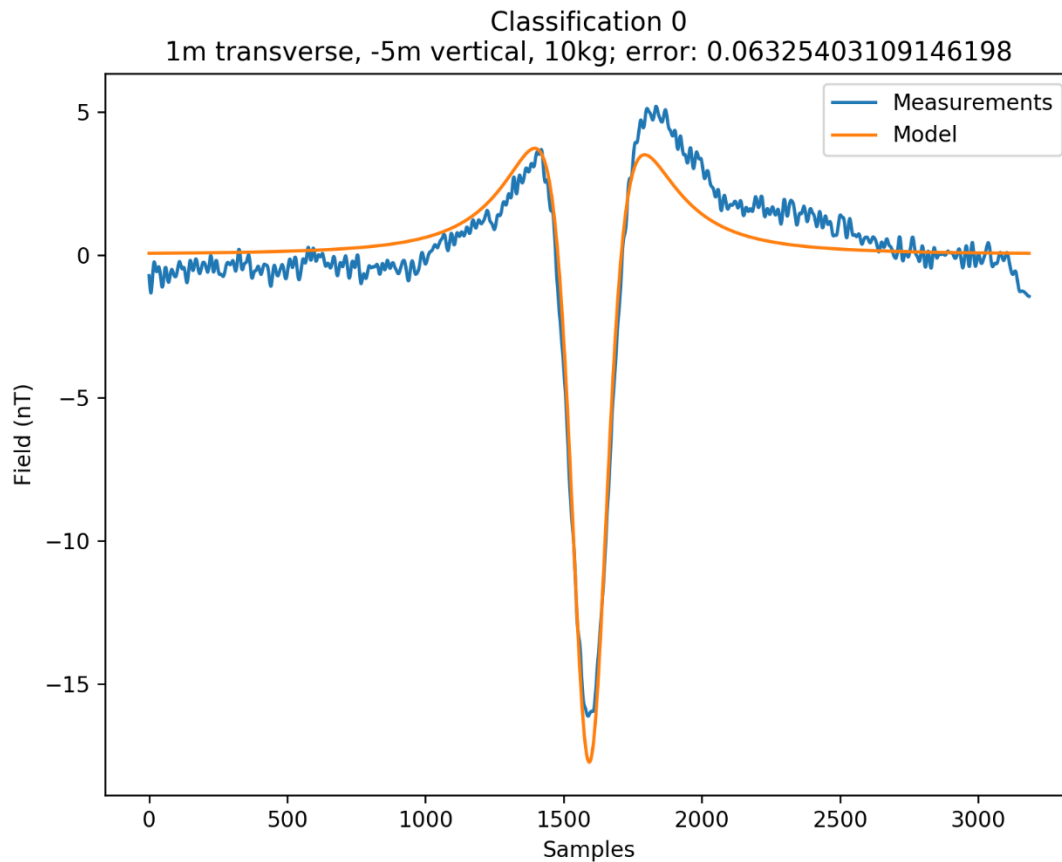
Figure 4.17: Classification snapshot showing measured data and the model template associated with the best classification match.

The classifier runs on each detection snapshot, and it takes several seconds to run when using tens of thousands of templates on the sensor computer in the AUV. This brief latency is acceptable, since it only runs when detections occur, not continuously.

4.7.5 Multiple mean squared error classifier

When performing classifications using a single pass near a magnetic target, there is ambiguity: between left and right, and between the magnitude of the magnetic moment and the distance between the vehicle and the target. (The signatures of stronger targets located farther away are similar to smaller targets at close range.) This ambiguity is resolved by using data from multiple passes by the target with a multiple minimum mean-squared error (MMSE) classifier.

The input set for the multiple MMSE classifier is the collection of detection snapshots resulting from a reacquire operation around the initially-detected target. Each detection snapshot is subjected to the mean-squared error classifier described in the previous section, and the mean-squared error (MSE) values for each geometric position and target moment magnitude (mass) are stored.

The MSE values from multiple passes are gridded to a regular 0.5 meter grid via linear interpolation in the transverse (magnetic east-west) and vertical (depth) directions. The grid positions in geographic space are determined by combining the transverse and vertical ranges used by the classifier with the position of the vehicle at the time corresponding to each classification.

The MSE values are inverted and summed in transverse (east-west), vertical (depth), and moment magnitude (mass) dimensions to produce a combined MMSE score that incorporates data from every pass near the detected target. The along-track (northing) target position estimate is given by the mean of the vehicle northing positions for all the detections. In this way, measurements from all the passes near the target are incorporated in the final classification. This

typically resolves ambiguities in target position and moment magnitude (mass), as shown in
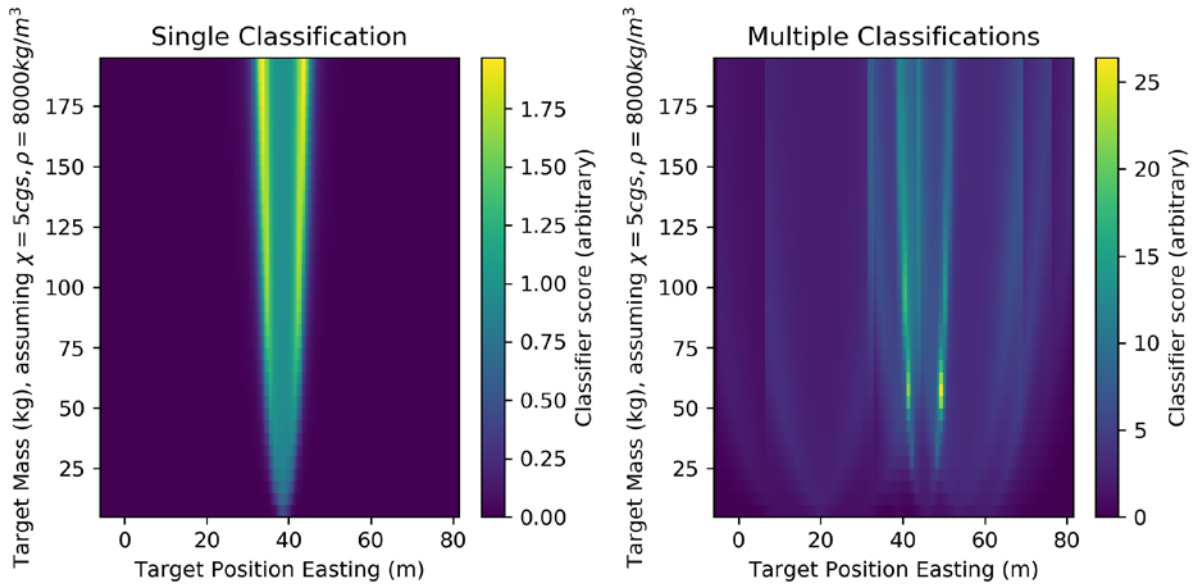
Figure 4.18.
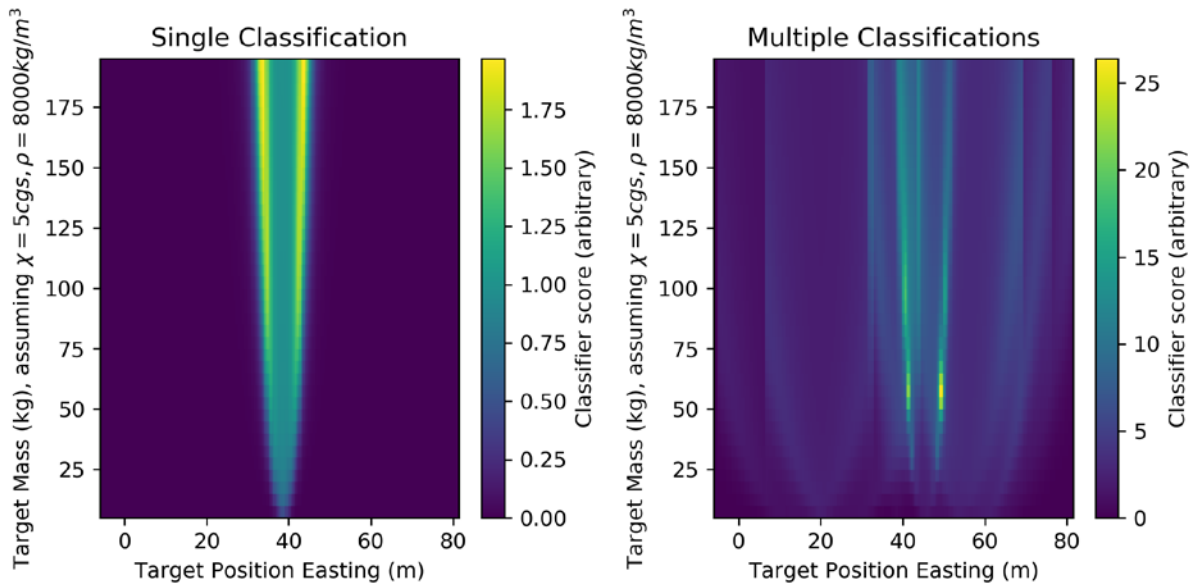
Figure 4.18: Ambiguity slices (at one target depth) for classifications using either a single classification (left) or the multiple pass classifier operating on data from 5 passes near a target. This target was determined to be a Kawasaki Ka-40 engine upon diver inspection, and the estimated mass (from magnetic moment magnitude) is consistent with this.

When validated against target locations from other sensor modalities, the multiple MMSE classifier performs well.

4.7.6 Limitations

This detection and classification system has proven effective in practice, and has been used for numerous archaeological seabed surveys. However, it has limitations rooted in the need to maintain computational tractability on-board the AUV by pre-calculating model values and limiting the total number of models used.

The primary limitation lies with the assumption that a single dipole target is present. If multiple dipole targets (as shown in Figure 4.19) or non-dipole targets such as pipelines or cables are encountered, incorrect classifications can be made. This does not generally affect detection of targets, since the superposition of multiple small dipoles appears as a single large dipole at ranges much larger than the distance between the individual dipoles.
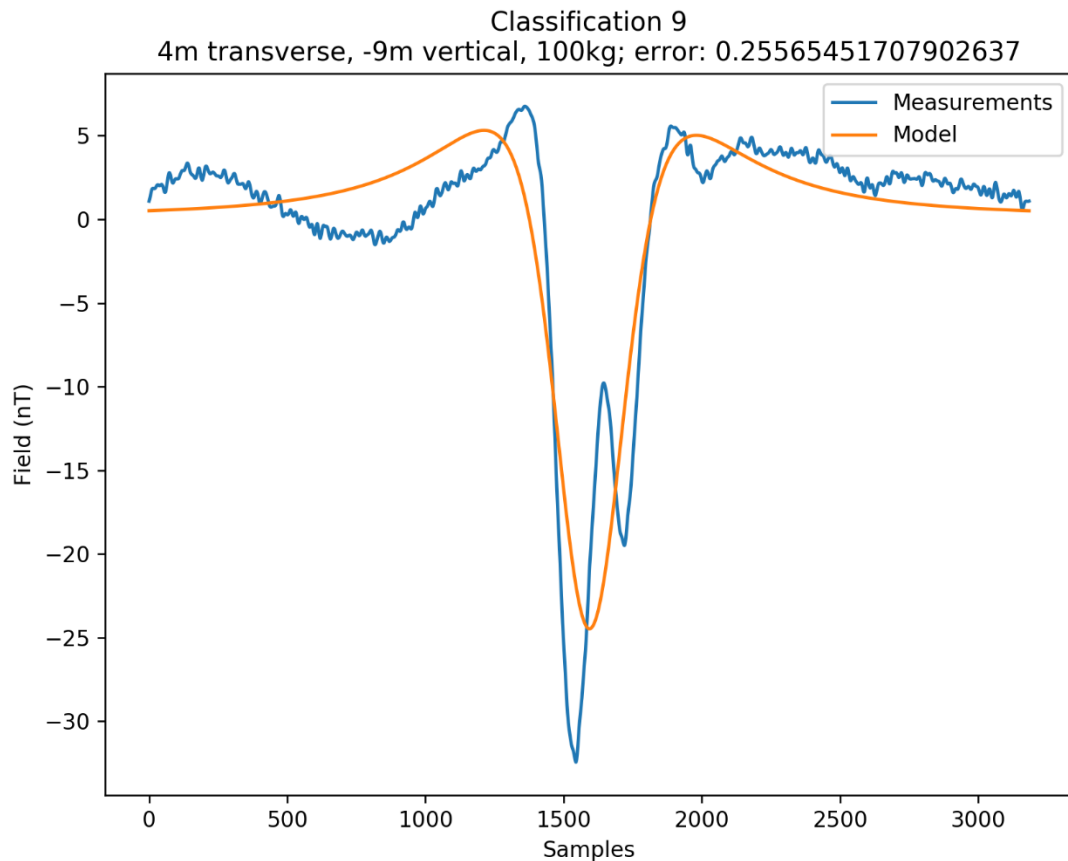
Figure 4.19: Classifier match near a multiple-dipole target while surveying a debris field associated with an aircraft wreck. Rather than recognizing that the two minima correspond to discrete dipole disturbances, the classifier has identified the best-fit single dipole solution, and the estimate of target properties is incorrect.

Additionally, only a limited range of dipole target sizes and geometries are modeled, and, if the actual target properties are not modeled, the classifier output will be incorrect. In practice, the set of modeled dipoles is chosen to represent the dipole magnitudes associated with the targets of the survey.

The modeled disturbance fields are based on a particular vehicle speed and heading in an isobathimetric environment. Small deviations in speed, heading, and bathymetry reduce the correlation between the model and measurements, but this is not catastrophic. (It can be modeled

as a slight decrease in SNR for the detector and lower correlation or higher MSE for the classifier.). The prefilter system detects excursions in vehicle kinematics and marks the corresponding magnetic data invalid, so any large deviations may cause gaps in detection coverage. This can be mitigated, as these gaps are currently detected in real time, and future work may produce autonomy behaviors to redirect the vehicle such that these areas are re-surveyed.

While not observed in the reported surveys, geomagnetic storms may generate signatures that mimic features of interest. This can be addressed via post-processing using data from reference stations [126], but it is not possible to filter out these signals in real-time using this system.

4.7.7 Autonomy

The on-board real-time magnetic target detector drives an autonomous sense-and-react reacquisition behavior. While no target is currently being reacquired, the vehicle swims a broad survey pattern. When a target of interest is detected, the vehicle is commanded to perform reacquire maneuvering, where the vehicle will turn and swim additional tracks near where the target was detected.

The first reacquire maneuver ("Reacquire Find" in Figure 4.20) has two primary goals: determining if the initial detection was erroneous and resolving the left-right ambiguity inherent in using a scalar magnetometer to identify targets. The path chosen for the first reacquire maneuver drives two north-south tracks at the estimated transverse distance of the target. As a result, if the classifier determined the correct transverse range using data from the first pass, one of these subsequent tracks should pass directly over top of the target. Therefore, the signal from the target should be stronger than on the first pass.

If no target is detected on these passes, the algorithm assumes that the initial detection was made in error, and the vehicle will resume its original broad survey path.

If a detection occurs during the first reacquire (Reacquire Find) passes, a new estimate of the target position is formed by taking the average of the transverse and along-track positions associated with all the detections. (Note that this is not the same algorithm used when operating the multiple-pass MMSE classifier, which is more computationally demanding.) The vehicle is then commanded to navigate along two additional north-south tracks 2 meters to either side of the new target position estimate ("Reacquire Characterize" in Figure 4.20). Detections and classifications are generated on these additional passes. This behavior typically results in at least four distinct detections of the same target that was initially detected. These data are processed by the multiple MMSE classifier as described earlier, and a composite target classification is generated.

The operator can specify the vehicle altitude during these reacquires based on knowledge of the local environment. The altitude is chosen to balance the need for vehicle safety with the desire to swim as close to the bottom (and therefore the target on or under the seabed) as possible.

A summary state machine diagram of these behaviors is shown in Figure 4.20. An example showing vehicle mission playback snapshots from a survey mission over an aircraft debris field is illustrated in Figure 4.21.
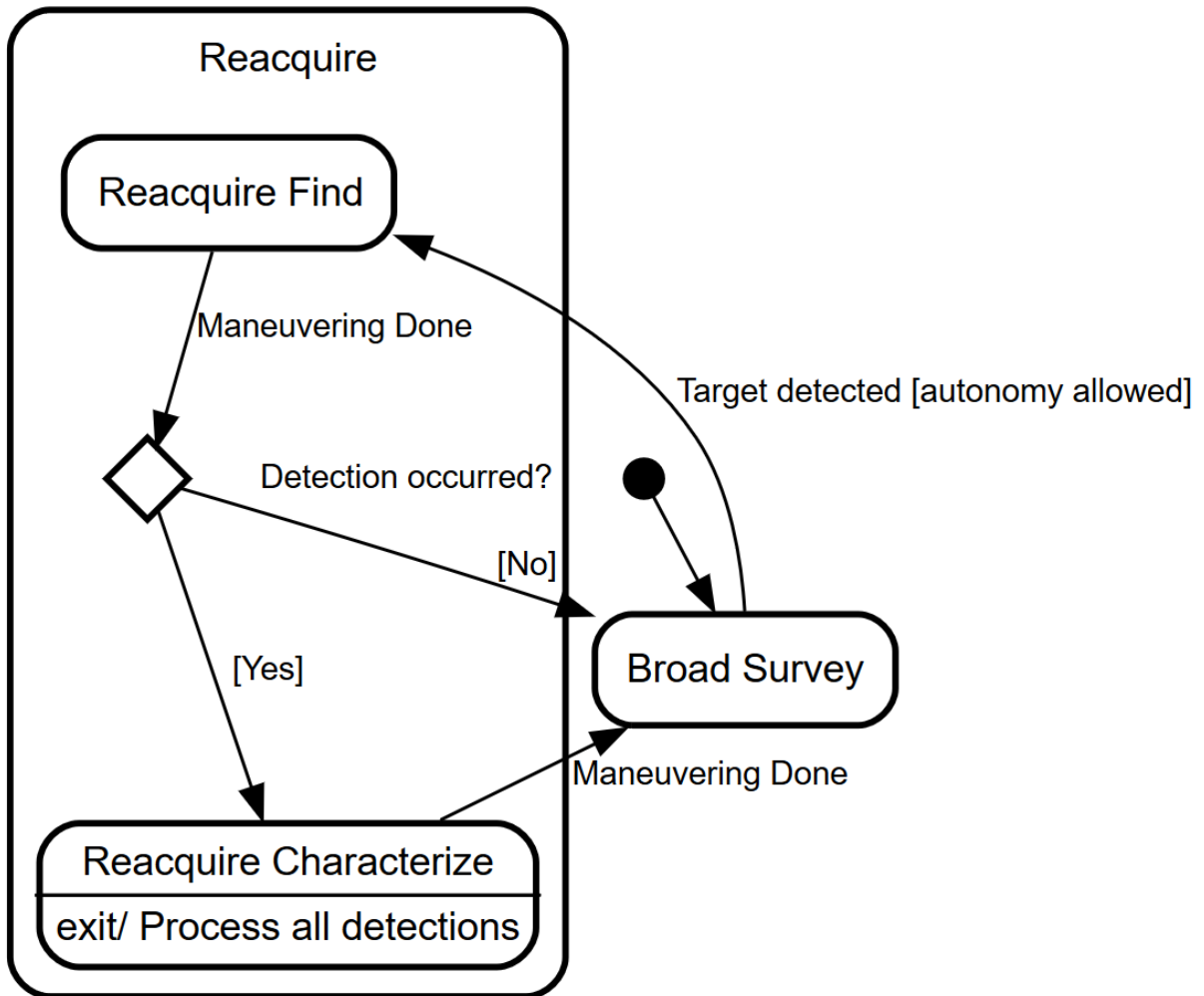
Figure 4.20: Simplified state diagram of autonomous reacquire behaviors. The vehicle begins running a broad survey pattern. When a magnetic detection occurs, the vehicle maneuvers in a pattern (Reacquire Find) to resolve the left-right ambiguity in the target detection and collect additional data. If no detections occur during this maneuvering, the initial detection was likely erroneous, so the vehicle returns to the broad survey course. If at least one detection occurs, the vehicle maneuvers in a narrow box over the new estimated target position (Reacquire Characterize).
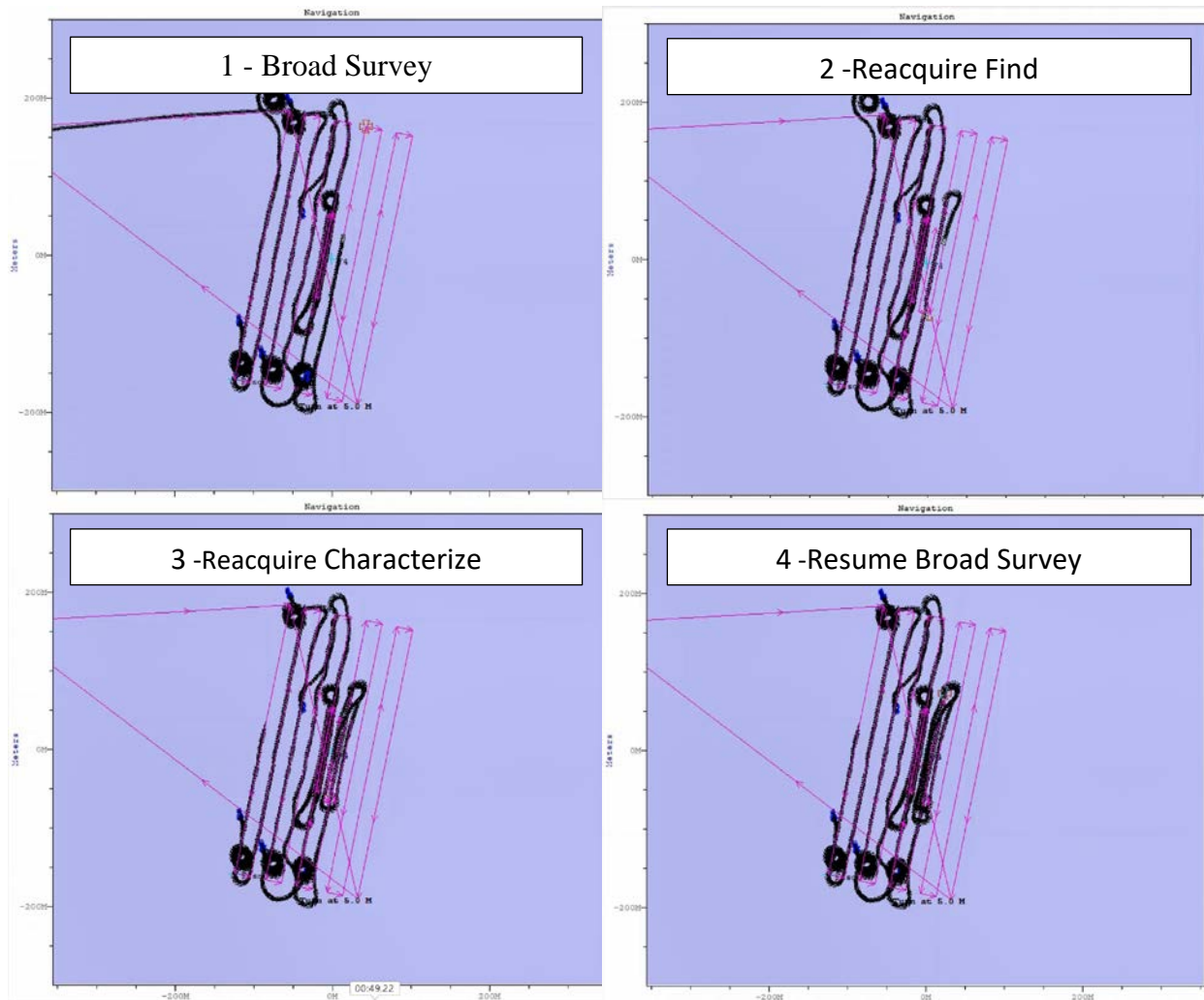
Figure 4.21: Autonomous reacquire behavior mission playback from a mission over an aircraft debris field. Time flows left to right, top to bottom. Top-left: The vehicle (Black line shows vehicle track) is running a broad survey pattern (magenta lines show planned track). Top-right: A target was detected, and the vehicle is running Reacquire Find maneuvering. The new planned track is visible. Bottom-left: Detections were made in Reacquire Find, so the vehicle begins Reacquire Characterize maneuvering. The new planned track is shown, and it is centered over the correctly-resolved target position. Bottom-right: Reacquire Characterize maneuvering is complete, and the vehicle is resuming the broad survey path. Video online.

This behavior provides an important system-level optimization of survey performance. To maximize the area-coverage rate, it is desirable to run surveys with larger lane spacing. However, to ensure that no targets are missed, this requires lowering the detection threshold.

97

When the detection threshold is lowered, it increases the probability of false alarm. Because the cost (in time and energy) of individual reacquire maneuvers when using the autonomous reacquire behavior is low compared with separate reacquire missions, it reduces the cost of false alarms. For example, an autonomous reacquire maneuver to confirm the existence of a target takes approximately 3 minutes, while a dedicated reacquire mission requires much more time. In addition to the time spent surveying over a target, separate reacquire missions may involve transit time for the AUV, as well as time spent in deployment, recovery, and boat transits to the operation area.

If large lane spacing is used for a survey, using the maximum range required for detection on a single pass will not collect enough measurements to accurately characterize the target. By autonomously reacquiring the target immediately after detection, it addresses this concern, and it eliminates the need for a separate magnetic reacquire mission.

The magnetic reacquisition behavior is implemented on the AUV using a collection of ROS nodes, illustrated in Figure 4.22. Processing steps are divided logically, such that behaviors and signal processing steps are compartmentalized and may be modified independently from one another. All ROS messages are logged during missions (via rosbag, a standard logging utility incorporated in the ROS middleware) to enable post-mission analysis and development through simulation using real data.

The autonomous reacquire behaviors do not override any of the health-and-safety functionality of the vehicle, which is maintained by the vehicle "front seat" computer.
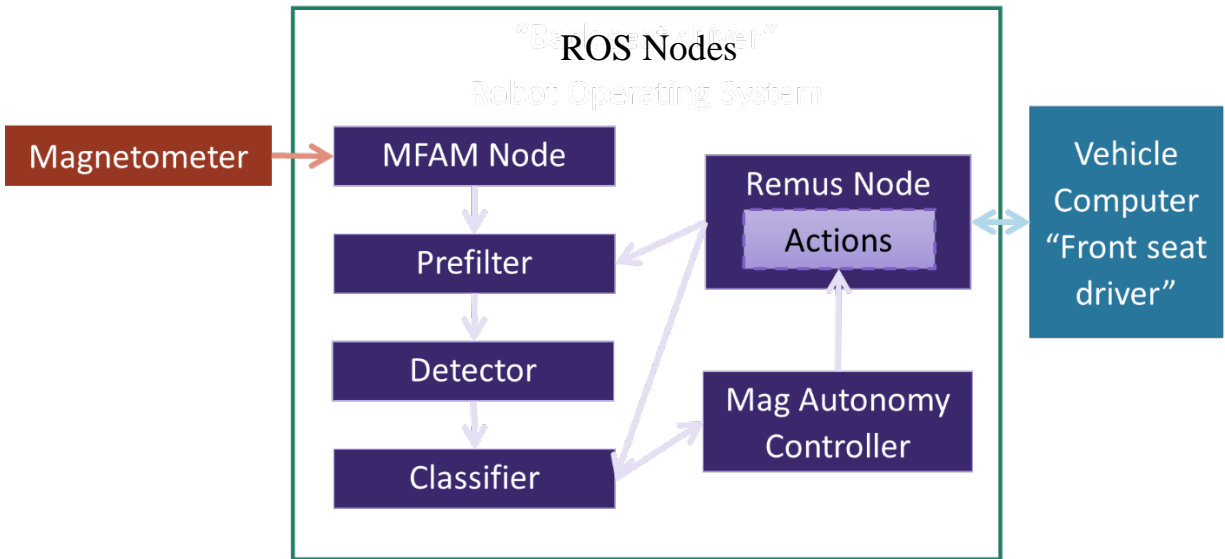
Figure 4.22: Magnetic target reacquisition system components. ROS nodes are shown as purple boxes, and data flow is indicated with arrows.

4.7.8 Multiple-vehicle autonomy

The on-board classification capability also enables multiple-vehicle sense-and-react behaviors to autonomously reacquire the target using other sensor modalities, such as optical imagers and high-resolution multibeam sonars.

The vehicles' acoustic modems (WHOI Micromodem-2 [59]) are used to coordinate this behavior. In the current implementation, the two vehicles communicate directly with one another. However, the system architecture allows for the use of acoustic relay nodes to pass messages between vehicles and can be easily extended for use with more than two vehicles.

On the magnetic sensing vehicle, a ROS message containing information about the target classification, including the estimated position, moment magnitude, and classification score is generated each time a multiple-pass classification is completed. An acoustic bridge ROS node receives these messages and efficiently encodes the data for acoustic transmission using 192-

byte Micromodem-2 packets. Each target is uniquely identified using the ROS message header of the target classification message. The target messages (several of which may be packed into a single Micromodem packet) are transmitted acoustically on an operator-specified fixed schedule until all the target messages have been acknowledged by the partner vehicle.

On the partner reacquire vehicle, these acoustic messages are received and converted back to ROS target classification messages. Each time a packet containing target messages is received, the partner vehicle replies acoustically with an acknowledgement packet that lists the target identifiers that were successfully received. A reacquire behavior node on the partner vehicle processes the target classification messages and determines, based on the classifier score and the vehicle's other objectives, if reacquire maneuvering should take place. If reacquisition is called for, the behavior node command the vehicle to perform a reacquisition via appropriate ros_remus actions. The parameters of the reacquisition actions (lane spacing, vehicle altitude, and speed) are determined by the requirements of the sensor being used. An overview of this system is illustrated in Figure 4.24.

This system has been successfully exercised at sea to autonomously reacquire archaeological targets of interest. Example mission playback snapshots are shown in Figure 4.23.
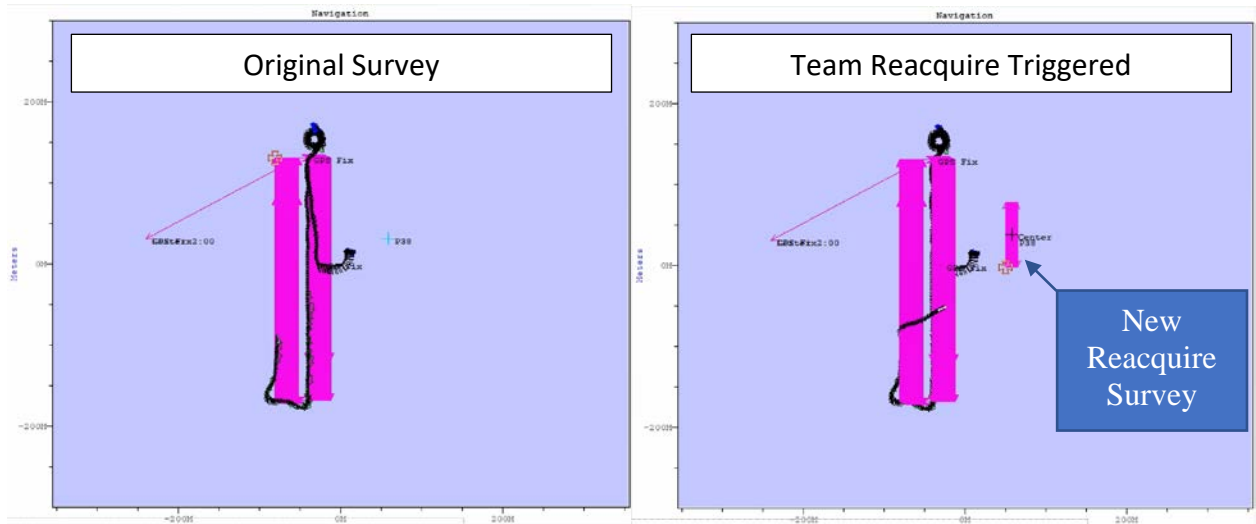
Figure 4.23: Mission playback snapshots showing cooperative reacquire behavior. Left: a vehicle is running a multibeam bathymetry survey (planned path shown in magenta, vehicle track shown in black). The magnetometer-equipped vehicle (not shown) is running a magnetic reacquire mission near the point labeled "P38". Right: The magnetometer vehicle has sent an acoustic packet with a target characterization message. The multibeam vehicle is now travelling to reacquire that target (new magenta box showing planned reacquire survey path to the right, vehicle track in black). Video online.
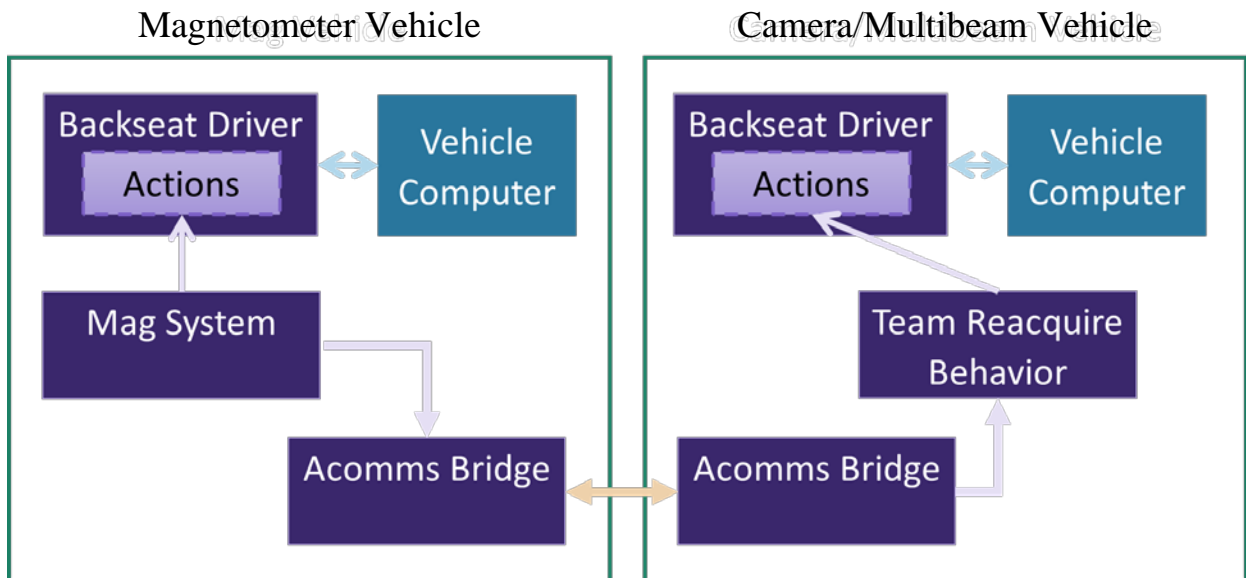
Figure 4.24: Diagram showing major components of the multiple-vehicle autonomous reacquire system.

101

4.8   Conclusions and Future Work

A scalar magnetometer has been integrated in a small REMUS 100 autonomous underwater vehicle, and this system has been fielded to perform geomagnetic and archaeological surveys. This system has been characterized both in the lab and at sea to determine its performance limits. Data from the magnetometer is processed to correct for interference and errors introduced by the AUV platform. It has seen extensive deployment under many different environmental conditions at sites near San Diego (USA), Papua New Guinea, Kiska (Alaska, USA), and Palau.

When conducting seabed surveys, detection and characterization of targets of interest is performed in real-time aboard the AUV. This system is used to drive both single- and multiple-vehicle autonomous target reacquisition behaviors. The combination of on-board target detection and autonomous reacquire capability greatly increases the effective survey coverage rate of the magnetometer system.

Although this system has been used operationally for archaeological surveys, and its accuracy has been validated through comparison with other sensor systems, we have not yet had the opportunity to run against reference magnetic targets on the seabed. This experiment is planned.

Although the profile of the vehicle precludes traditional transverse gradiometer geometries, a longitudinal array may enable new vehicle interference mitigation techniques (common-mode rejection) in addition to providing a fixed geometry for along-track, non-

synthetic gradiometric processing. The system architecture lends itself to incorporating additional sensors and collecting experimental data to evaluate these ideas.

The use of a vector magnetometer in conjunction with the scalar magnetometer has the potential to improve survey performance. When coupled with modified versions of the autonomous reacquire behaviors, the ability to resolve left-right ambiguities without an additional pass would increase the effective coverage rate of the system.

4.9 Acknowledgements

The material in this chapter, in part, has been submitted for publication. The dissertation author was the primary investigator and author of this paper: E. Gallimore, E. Terrill, A. Pietruszka, J. Gee, A. Nager, and R. Hess, "Magnetic survey and autonomous target reacquisition with a scalar magnetometer on a small AUV".

5 The Detection of Submerged WWII Aircraft Sites via Autonomous Underwater Vehicle Based Magnetometer Survey

A system incorporating a scalar magnetometer on a small autonomous underwater vehicle (AUV) is used to conduct surveys searching for submerged World War II-era artifacts, primarily debris associated with aircraft wrecks. The system provides high-accuracy target localization and uses advanced signal processing techniques and vehicle autonomy to increase the effective range of the magnetometer, thereby increasing the survey coverage rate. It offers significant advantages over towed magnetic sensing systems. Several sites surveyed using this system are documented.

5.1 Magnetic Sensing of Aircraft Debris

When magnetically susceptible material is exposed to a magnetic field, such as the Earth's magnetic field, a magnetic dipole is induced in the material. This induced dipole field is superposed with the ambient (Earth) field, and this disturbance field can be sensed by detecting spatial changes in the total magnetic field. The magnitude of this disturbance field is a function of the susceptibility of the material, the mass of material, the geometry and size of the object, and the ambient magnetic field.

At distances significantly larger than the dimensions of a target, which may be a debris field consisting of several discrete components, the observable disturbance field converges to that from an equivalent single dipole source.

Detecting debris associated with aircraft wrecks via magnetic sensing is typically limited to locating specific components, such as engines and landing gear, that are constructed using iron-containing steel. This contrasts with other contemporary artifacts, such as shipwrecks, which often incorporate much more iron and steel in their construction.

Most World-War-II-era aircraft are constructed primarily from aluminum, which is weakly paramagnetic. However, its magnetic susceptibility is low [127], [128], and therefore does not generate signatures observable with the system described here (or traditional towed magnetometer systems). In contrast, many steel alloys and iron are ferromagnetic, and the dipole moments induced in these materials by the earth's magnetic field are observable as disturbances in the total magnetic field near objects. The properties of these objects are generally not known precisely, but "rule-of-thumb" susceptibility values exist [122].

In additional to ferromagnetic material that may experience induced magnetism, wrecks may include permanently magnetized components, such as magnetos or parts magnetized during non-destructive testing [129]. Additionally, ferromagnetic components that have remained stationary for decades will become magnetized by the Earth's field.

5.2 Comparison with Towed Systems

Towed magnetometers have been used for archaeological survey, searching for both buried structures [130] and artifacts such as shipwrecks [131].

Although towed systems sometimes incorporate altimeters, depth sensors, or compasses, the precise position of the towed system at any point must be determined using the position of the controlling ship and calculations based on the amount of deployed cable. This generates a practical limit on position accuracy with towed systems. In contrast, AUVs incorporate precise

navigation using either inertial navigation systems, acoustic trilateration using surveyed beacons, or both.

It is practically difficult to maintain constant altitude over the seafloor with a ship-towed magnetometer. As the strength of dipole fields falls with distance cubed, it is desirable to keep the magnetometer close to the seabed. However, the limited controllability of a towed system requires that it be towed at higher altitude to avoid collisions with the seafloor. In contrast, the AUV offers closed-loop altitude control that allows it to closely follow the seafloor, and it can therefore keep the sensor closer to the objects being sensed. This also avoids the need for so-called draping corrections [130], [132].

Towed systems also present challenges when turning, as large-diameter turns must be executed by the ship in order to avoid slacking the tow line. Excess distance must be incorporated into survey tracklines to ensure that the towed system is travelling straight on the trackline. In contrast, a two-man portable AUV can typically execute a 180-degree turn in a 10 m radius.

When towing from a ship, the towed magnetometer needs to be towed with enough scope that the magnetic signature of the ship does not prevent meaningful observation. The AUV generates smaller magnetic disturbance fields than most ships, so the sensor can be operated closer to the AUV.

The primary advantage of towed systems is that it is possible to separate the magnetometer from the platform used to tow it. As magnetic field intensity falls rapidly with distance, this reduces the amount of observable platform noise. Therefore, mitigation of platform signal contamination is paramount for a sensor that is affixed to the body of the AUV.

5.3   Magnetometer Use within Larger Surveys

Magnetic sensing complements other sensor modalities, such as sonar, when searching for aircraft debris [4]. Sidescan sonar remains the wide-area search tool of choice for most situations, which typical coverage rates of about 0.424 km^2 per hour [7]. The effective range of the magnetic sensor varies with operation area (the range is longer in locations where the Earth's magnetic field is stronger) and target size. Using the matched-filter dipole detection system (section 4.7) and searching for light aircraft debris, it typically covers about 0.100 to 0.175 km^2 per hour. This is enabled by the autonomous reacquisition behavior on the AUV, without which the coverage rate to obtain an equivalent number of target samples would drop by a factor of 4 (section 4.7.7). The higher coverage rate is comparable to that of short-range, high resolution sidescan sonar use for target reacquisition [7].

As the AUV equipped with the magnetometer can also be outfitted with sidescan sonar (as was the case in these studies), it can be used to simultaneously collect high-resolution sidescan data and magnetic data.

The coverage rate suggests that the magnetometer is best suited for small-area searches or reacquisition missions where a target is suspected. However, it offers important advantages over sonar: it can identify buried targets, and it can distinguish between clutter from rocks or coral and anthropogenic targets, including artifacts that have been covered in coral or hidden by fish (underwater wrecks often create vibrant fish habitats).

The magnetometer system on the AUV benefits from using the same navigation as the other AUV-based surveys. This facilitates repeat surveys using different sensor packages.

5.4 Case Studies

This system has been used to aid searches for likely aircraft crash sites worldwide. The survey locations are informed by historical investigation and, in some cases, probabilistic modeling of flight and crash trajectories [4].

At sites where wrecks are identified, empirical estimates of the magnetic moment associated with the debris are computed. This can be used to guide future surveys of new areas, as it bounds the minimum moment size to use when searching for similar artifacts. For the wreck sites where a magnetic moment is given, the moment was calculated by the multiple minimum mean squared error classifier described in section 4.7.5. The corresponding mass values are given assuming a material density of 8000 kg/m^3 (appropriate for steel) and rationalized volume susceptibility (κ) between 12.5 and 125, using "rule-of-thumb" values for man-made steel objects from [122]. (This corresponds to a volume susceptibility of 1 to 10 emu/cm3 in the cgs system.)

5.4.1 B-25 Mitchell, Papua New Guinea

This B-25 Mitchell aircraft, serial number 42-64850, was piloted by Flight Officer Richard Smith and lost November 3, 1943. The aircraft was landed on water under control, and therefore did not disintegrate on impact. The wreck was discovered in 2017 by our research team, and it lies in approximately 32 m of water near Bilibili Island.

Initial surveys were conducted using 600 kHz sidescan sonar and followed with the magnetometer system and dive teams. The repeat survey with the magnetometer was conducted by AUV the day following the sonar survey. These surveys were conducted without deploying acoustic transponders to provide high-resolution undersea navigation, but the repeat navigation performance shows agreement within 10 meters, consistent with navigation uncertainty for an

AUV operating without external navigation fixes under these conditions. Figure 5.1 shows the magnetic target location overlaid on sidescan sonar imagery.

The multiple minimum mean squared error classifier identifies the overall far-field dipole magnitude of the wreck as 34 Am^2, equivalent to a steel mass between approximately 68 and 675 kg.
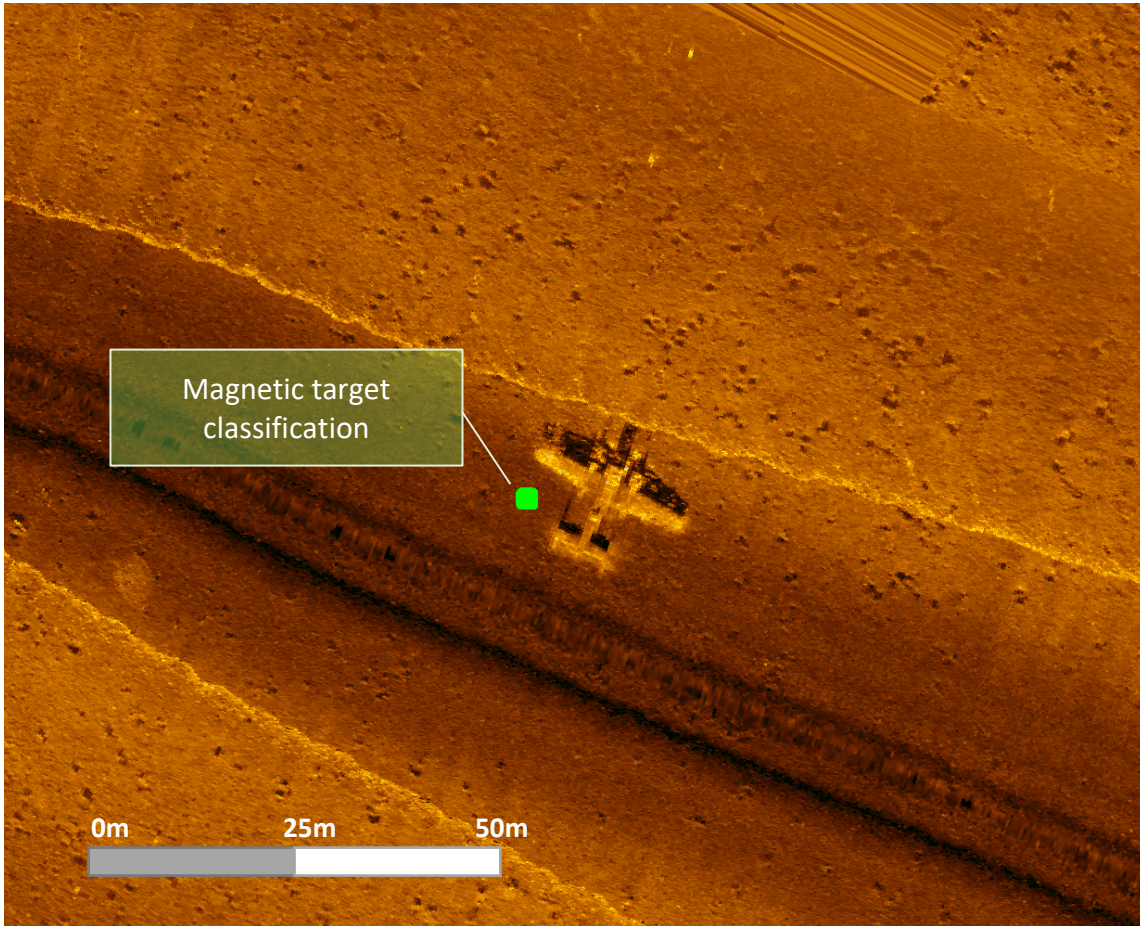
Figure 5.1: Magnetic target location determined by multiple MMSE classifier overlaid on 600 kHz sidescan sonar imagery (collected 12 hours earlier using a different vehicle) of an intact B-25 aircraft wreck near Madang, Papua New Guinea. The classifier incorporated data from seven passes near the target to form this estimate. The classifier estimated the target depth at 31.5 m (below the surface of the water), which is consistent with a target resting on the seabed in this area. The locational accuracy falls within the vehicle navigational accuracy across these two missions.

5.4.2   Torpedo Disposal Site, Palau

An undocumented torpedo disposal site was discovered by our research team in 2019 while searching for an aircraft wreck north of Malakal, Palau. The initial target of interest was identified in wide-area 600 kHz sidescan sonar imagery, and the magnetometer-equipped AUV was deployed to reacquire the area using both high-resolution, 1200 kHz sidescan sonar and the magnetometer system. The vehicle conducted autonomous reacquire maneuvering due to

detection of magnetic targets, which resulted in high density magnetic sampling of the area. The magnetic data clearly indicated the presence of anthropogenic artifacts, and subsequent ROV operations confirmed that these were Japanese torpedoes, presumably dumped by U.S. forces after capturing the munitions 75 years prior during the liberation of the Palau island chain.

The large number of discrete objects lends itself to examination using the synthetic gradient processing toolchain (Section 4.6.2). Figure 5.2 shows synthetic gradient magnitude overlaid on 1200 kHz sonar imagery.
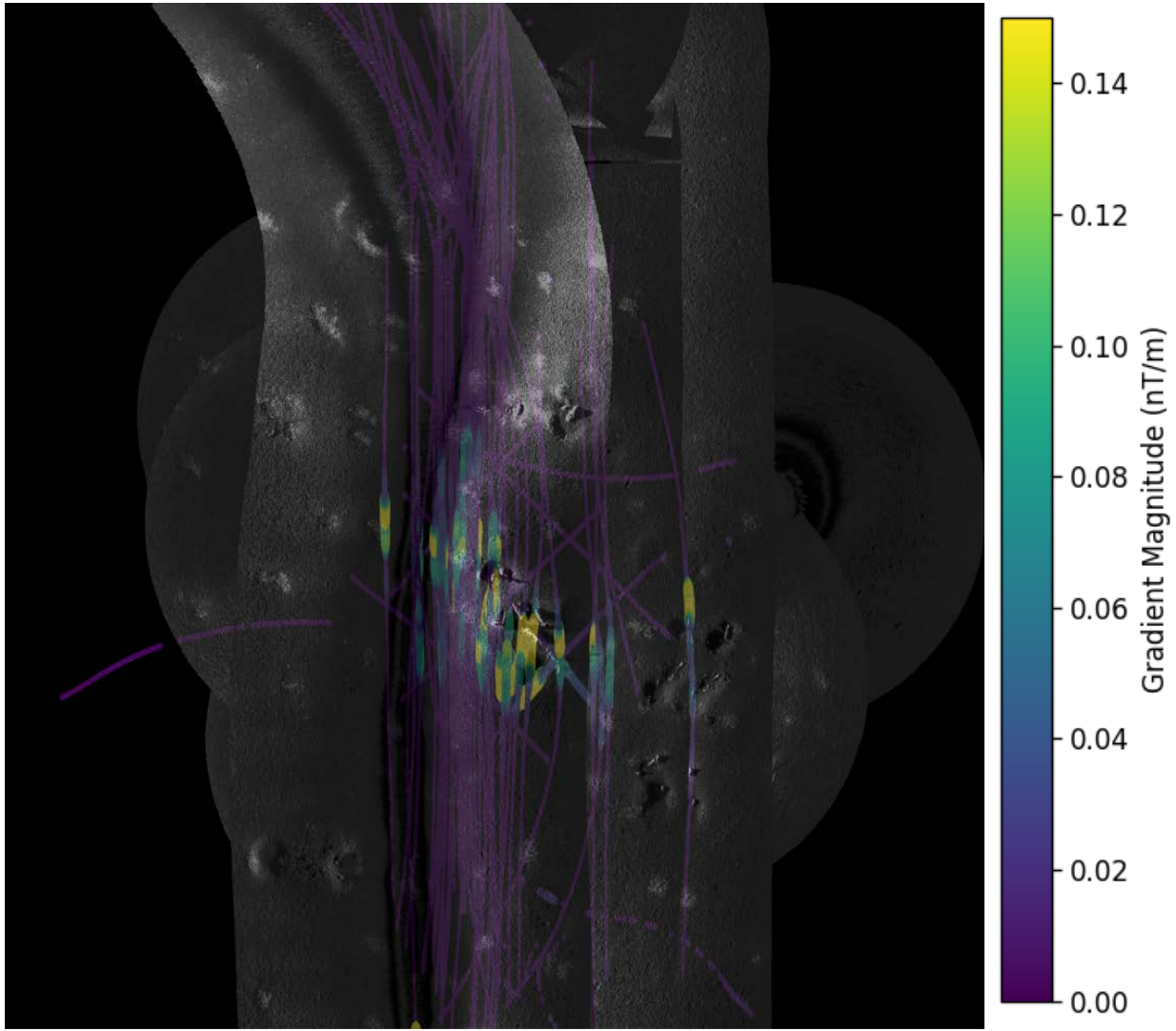
Figure 5.2: Overlay of sidescan sonar imagery (grayscale) and synthetic magnetic gradient data over World War II-era torpedo dump site. The magnetic gradient data clearly differentiates features associated with torpedoes from coral and rocks.

5.4.3   B-25 Mitchell, Papua New Guinea

Debris from a B-25 Mitchell aircraft was located by the magnetometer system and sidescan sonar survey in Hansa Bay, Papua New Guinea during an expedition conducted in October, 2017. Portions of a Wright R-2600 Cyclone engine (Figure 5.3) were identified by subsequent diver survey. The debris lies in approximately 4m water.

The engine generates a dipole anomaly of approximately 18 Am^2, corresponding to a steel

mass between 35 and 350 kg. There is additional, presumably buried, magnetically-detectable

debris extending out approximately 70 m from the location of the engine, with another possible

point target of magnitude 5 Am^2 (10 – 100 kg of steel) approximately 30 m away. No artifacts

beyond the engine were identified during the diver survey.
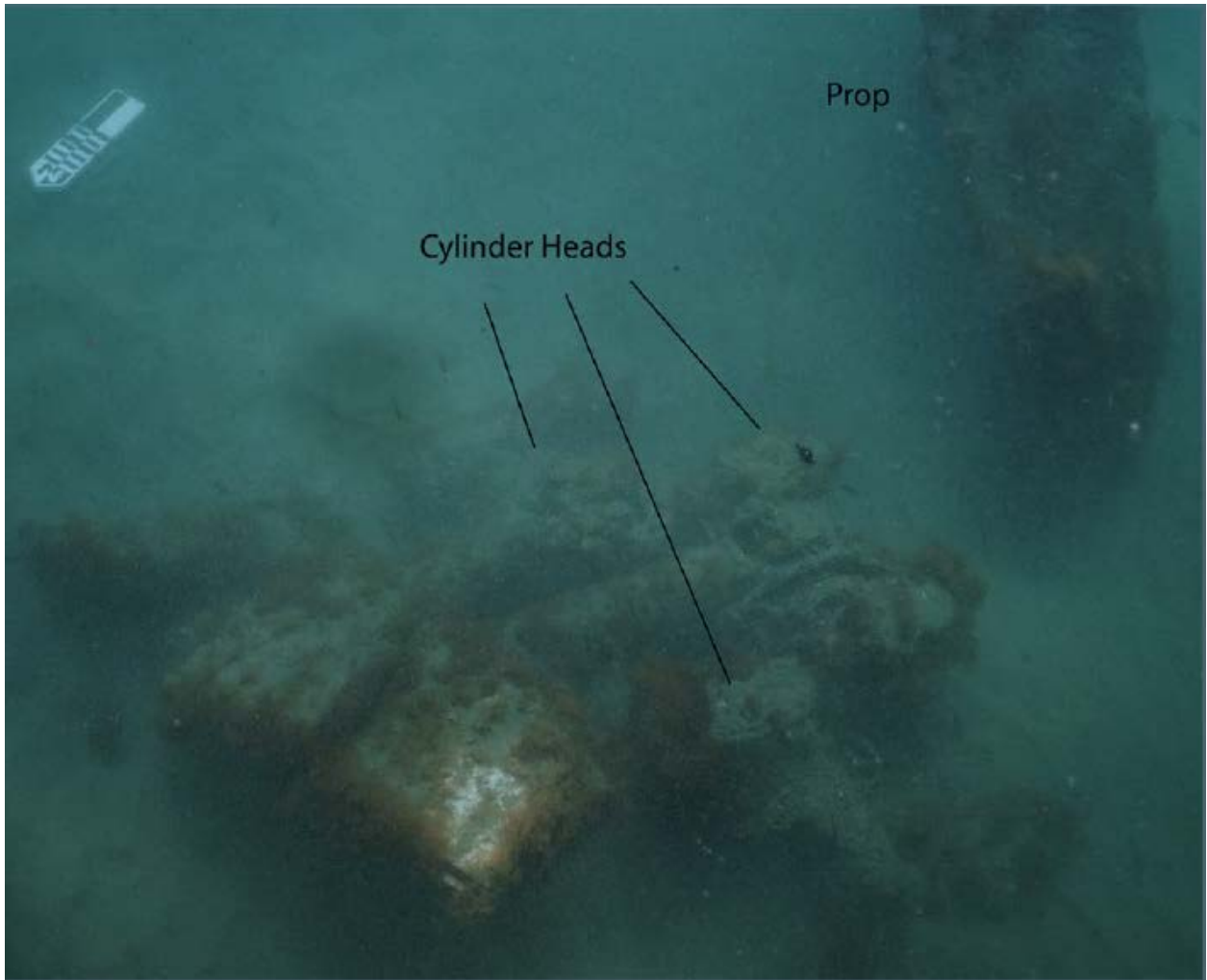
Figure 5.3: Photograph of cylinder head and propeller of Wright R-2600 engine located in
Hansa Bay, Papua New Guinea.

5.4.4   Ki-61, Papua New Guinea

The wreck of a Japanese Ki-61 single-engine aircraft was found in Hansa Bay, Papua New Guinea using the magnetometer system. The engine of this aircraft, which was subsequently identified by diver surveys, is a Kawasaki Ha-40 V-12 piston engine. A photo taken of the engine during this survey is shown in Figure 5.4.

The classified dipole moment was 14 Am^2, corresponding to an approximate equivalent mass of steel between 28 and 275 kg.

Figure 5.4: Photograph of Kawasaki Ha40 engine found as part of a wreck of a Japanese Ki-61 in Hansa Bay, Papua New Guinea.

5.4.5   Known Sites Used for Evaluation

A previously-identified F-4 Phantom aircraft crash site offshore La Jolla, California, USA was used to evaluate the magnetometer system.

The F-4 wreck (BuNo 153090) appears as a concentrated debris pile on sidescan sonar as a result of its high-speed crash after tumbling out of control from 32,000 ft (9750 m) on May 6, 1966.   The area nearby was surveyed, and the magnetic detection system identified and

reacquired the target. The magnetic classifier determined that the debris had a moment of approximately 27 Am^2, corresponding to an equivalent steel mass of approximately 48 to 475 kg (for a range of reasonable, possible magnetic susceptibility values).

5.5 Conclusion

The AUV-based magnetometer system has been successfully used to locate and characterize a number of historic aviation debris fields. This system offers an area coverage rate that is compatible with the needs of archaeological surveys, and it provides significant advantages over traditional towed magnetometer systems in these applications.

5.6 Acknowledgements

This chapter contains material currently being prepared for submission for publication. The dissertation author was the primary investigator and author of this material: E. Gallimore, A. Pietruszka, E. Terrill, "The Detection of Submerged WWII Aircraft Sites via Autonomous Underwater Vehicle Based Magnetometer Survey".

REFERENCES

[1]   N. Farr, A. Bowen, J. Ware, C. Pontbriand, and M. Tivey, "An integrated, underwater optical /acoustic communications system," in *OCEANS 2010 IEEE - Sydney*, 2010, pp. 1–6.

[2]   M. Stojanovic, "On the Relationship Between Capacity and Distance in an Underwater Acoustic Communication Channel," in *Proceedings of the 1st ACM International Workshop on Underwater Networks*, New York, NY, USA, 2006, pp. 41–47.

[3]   N. Farr, A. Chave, L. Freitag, J. Preisig, S. White, D. Yoerger, and P. Titterton, "Optical modem technology for seafloor observatories," in *Proceedings of MTS/IEEE OCEANS, 2005*, 2005, pp. 928-934 Vol. 1.

[4]   E. Terrill, M. Moline, P. Scannon, E. Gallimore, T. Shramek, A. Nager, R. Hess, M. Cimino, P. Colin, A. Pietruszka, and M. Anderson, "Project Recover: Extending the Applications of Unmanned Platforms and Autonomy to Support Underwater MIA Searches," *Oceanography*, vol. 30, no. 2, pp. 150–159, Jun. 2017.

[5]   C. Roman and R. Mather, "Autonomous Underwater Vehicles as Tools for Deep-Submergence Archaeology," *Proceedings of the IMechE*, vol. 224, no. 4, pp. 327–340, Nov. 2010.

[6]   B. Allen, R. Stokey, T. Austin, N. Forrester, R. Goldsborough, M. Purcell, and C. von Alt, "REMUS: a small, low cost AUV; system description, field trials and performance results," in *OCEANS '97. MTS/IEEE Conference Proceedings*, 1997, vol. 2, pp. 994–1000 vol.2.

[7]   E. Gallimore, E. Terrill, R. Hess, A. Nager, H. Bachelor, and A. Pietruszka, "Integration and Evaluation of a Next-Generation Chirp-Style Sidescan Sonar on the REMUS 100," in *Proceedings of the 2018 IEEE OES Autonomous Underwater Vehicle Symposium*, Porto, Portugal, 2018.

[8]   T. Aridgides, P. Libera, M. F. Fernandez, and G. J. Dobeck, "Adaptive-filter/feature-orthogonalization processing string for optimal LLRT mine classfication in side-scan sonar imagery," in *Detection and Remediation Technologies for Mines and Minelike Targets*, 1996, vol. 2765, pp. 110–122.

[9]   M. Montanari, J. R. Edwards, and H. Schmidt, "Autonomous Underwater Vehicle-Based Concurrent Detection and Classification of Buried Targets Using Higher Order Spectral Analysis," vol. 31, no. 1, pp. 188–199, 2006.

[10]   S. Reed, Y. Petillot, and J. Bell, "An automatic approach to the detection and extraction of mine features in sidescan sonar," *IEEE Journal of Oceanic Engineering*, vol. 28, no. 1, pp. 90–105, Jan. 2003.

[11] T. Aridgides, M. Fernandez, and G. Dobeck, "Fusion of adaptive algorithms for the classification of sea mines using high resolution side scan sonar in very shallow water," in *MTS/IEEE Oceans 2001. An Ocean Odyssey. Conference Proceedings (IEEE Cat. No.01CH37295)*, 2001, vol. 1, pp. 135–142 vol.1.

[12] G. J. Dobeck, J. C. Hyland, and L. Smedley, "Automated detection and classification of sea mines in sonar imagery," in *Detection and Remediation Technologies for Mines and Minelike Targets II*, 1997, vol. 3079, pp. 90–111.

[13] G. J. Dobeck, "Algorithm fusion for automated sea mine detection and classification," in *MTS/IEEE Oceans 2001. An Ocean Odyssey. Conference Proceedings (IEEE Cat. No.01CH37295)*, 2001, vol. 1, pp. 130–134 vol.1.

[14] C. M. Ciany and J. Huang, "Computer aided detection/computer aided classification and data fusion algorithms for automated detection and classification of underwater mines," in *OCEANS 2000 MTS/IEEE Conference and Exhibition. Conference Proceedings (Cat. No.00CH37158)*, 2000, vol. 1, pp. 277–284 vol.1.

[15] C. M. Ciany, W. C. Zurawski, G. J. Dobeck, and D. R. Weilert, "Real-time performance of fusion algorithms for computer aided detection and classification of bottom mines in the littoral environment," in *Oceans 2003. Celebrating the Past ... Teaming Toward the Future (IEEE Cat. No.03CH37492)*, 2003, vol. 2, pp. 1119-1125 Vol.2.

[16] B. Bingham, B. Foley, H. Singh, R. Camilli, K. Delaporta, R. Eustice, A. Mallios, D. Mindell, C. Roman, and D. Sakellariou, "Robotic tools for deep water archaeology: Surveying an ancient shipwreck with an autonomous underwater vehicle," *Journal of Field Robotics*, vol. 27, no. 6, pp. 702–717, 2010.

[17] "NOAA Ocean Explorer: AUVfest 2008: Mission Summary." [Online]. Available: https://oceanexplorer.noaa.gov/explorations/08auvfest/logs/summary/summary.html. [Accessed: 01-Apr-2019].

[18] B. P. Foley, K. Dellaporta, D. Sakellariou, B. S. Bingham, R. Camilli, R. M. Eustice, D. Evagelistis, V. L. Ferrini, K. Katsaros, D. Kourkoumelis, A. Mallios, P. Micha, D. A. Mindell, C. Roman, H. Singh, D. S. Switzer, and T. Theodoulou, "The 2005 Chios Ancient Shipwreck Survey: New Methods for Underwater Archaeology," *Hesperia: The Journal of the American School of Classical Studies at Athens*, vol. 78, no. 2, pp. 269–305, 2009.

[19] S. Desset, R. Damus, J. Morash, and C. Bechaz, "Use of GIBs in AUVs For Underwater Archaeology," *Sea Technology; Arlington*, vol. 44, no. 12, pp. 22,24-25,27, Dec. 2003.

[20] H. Singh, J. Adams, D. Mindell, and B. Foley, "Imaging Underwater for Archaeology," *Journal of Field Archaeology*, vol. 27, no. 3, pp. 319–328, 2000.

[21] N. Tsiogkas, Z. Saigol, and D. Lane, "Distributed multi-AUV cooperation methods for underwater archaeology," in *OCEANS 2015 - Genova*, 2015, pp. 1–5.

[22] N. Tsiogkas, G. Frost, N. Monni, and D. Lane, "Facilitating multi-AUV collaboration for marine archaeology," in *OCEANS 2015 - Genova*, 2015, pp. 1–4.

[23] N. Tsiogkas, G. Papadimitriou, Z. Saigol, and D. Lane, "Efficient multi-AUV cooperation using semantic knowledge representation for underwater archaeology missions," in *Oceans - St. John's, 2014*, 2014, pp. 1–6.

[24] M. L. Seto, Ed., *Marine Robot Autonomy*. New York, NY: Springer New York, 2013.

[25] "NOAA Ocean Explorer: AUVfest 2008: May 18 Log." [Online]. Available: https://oceanexplorer.noaa.gov/explorations/08auvfest/logs/may18/may18.html. [Accessed: 01-Apr-2019].

[26] C. von Alt, B. Allen, T. Austin, N. Forrester, R. Goldsborough, M. Purcell, and R. Stokey, "Hunting for mines with REMUS: a high performance, affordable, free swimming underwater robot," in *MTS/IEEE Oceans 2001. An Ocean Odyssey. Conference Proceedings (IEEE Cat. No.01CH37295)*, 2001, vol. 1, pp. 117–122 vol.1.

[27] C. von Alt, "REMUS 100 transportable mine countermeasure package," in *Oceans 2003. Celebrating the Past ... Teaming Toward the Future (IEEE Cat. No.03CH37492)*, 2003, vol. 4, pp. 1925-1930 Vol.4.

[28] R. Stokey, T. Austin, B. Allen, N. Forrester, E. Gifford, R. Goldsborough, G. Packard, M. Purcell, and C. von Alt, "Very shallow water mine countermeasures using the REMUS AUV: a practical approach yielding accurate results," in *MTS/IEEE Oceans 2001. An Ocean Odyssey. Conference Proceedings (IEEE Cat. No.01CH37295)*, 2001, vol. 1, pp. 149–156 vol.1.

[29] E. Bovio and H. Schmidt, "The GOATS Joint Research Project: Underwater Vehicle Networks for Acoustic and Oceanographic Measurements in the Littoral Ocean," MIT, MITSG 03-08J, 2000.

[30] L. Freitag, M. Grund, C. von Alt, A. Stokey, and T. Austin, "A shallow water acoustic network for mine countermeasures," presented at the Underwater Defense Technology, 2005.

[31] E. A. Fiorelli, "Cooperative Vehicle Control, Feature Tracking and Ocean Sampling," Princeton University, 2005.

[32] E. Fiorelli, N. E. Leonard, P. Bhatta, D. A. Paley, R. Bachmayer, and D. M. Fratantoni, "Multi-AUV Control and Adaptive Sampling in Monterey Bay," *IEEE Journal of Oceanic Engineering*, vol. 31, no. 4, pp. 935–948, Oct. 2006.

[33] E. Fiorelli, N. E. Leonard, P. Bhatta, D. Paley, R. Bachmayer, and D. M. Fratantoni, "Multi-AUV control and adaptive sampling in Monterey Bay," in *Autonomous Underwater Vehicles, 2004 IEEE/OES*, 2004, pp. 134–147.

[34] Y. Zhang, J. G. Bellingham, J. P. Ryan, B. Kieft, and M. J. Stanway, "Two-dimensional mapping and tracking of a coastal upwelling front by an autonomous underwater vehicle," in *2013 OCEANS - San Diego*, 2013, pp. 1–4.

[35] Y. Zhang, M. A. Godin, J. G. Bellingham, and J. P. Ryan, "Using an Autonomous Underwater Vehicle to Track a Coastal Upwelling Front," *IEEE Journal of Oceanic Engineering*, vol. 37, no. 3, pp. 338–347, Jul. 2012.

[36] Y. Zhang, J. G. Bellingham, M. A. Godin, and J. P. Ryan, "Using an Autonomous Underwater Vehicle to Track the Thermocline Based on Peak-Gradient Detection," *IEEE Journal of Oceanic Engineering*, vol. 37, no. 3, pp. 544–553, Jul. 2012.

[37] Y. Zhang, M. Godin, J. G. Bellingham, and J. P. Ryan, "Ocean front detection and tracking by an autonomous underwater vehicle," in *OCEANS'11 MTS/IEEE KONA*, 2011, pp. 1–4.

[38] Y. Zhang, J. G. Bellingham, M. Godin, J. P. Ryan, R. S. McEwen, B. Kieft, B. Hobson, and T. Hoover, "Thermocline tracking based on peak-gradient detection by an autonomous underwater vehicle," in *OCEANS 2010 MTS/IEEE SEATTLE*, 2010, pp. 1–4.

[39] S. M. Petillo, "Autonomous & adaptive oceanographic feature tracking on board autonomous underwater vehicles," Thesis, Massachusetts Institute of Technology, 2015.

[40] S. Petillo and H. Schmidt, "Exploiting Adaptive and Collaborative AUV Autonomy for Detection and Characterization of Internal Waves," *IEEE Journal of Oceanic Engineering*, vol. 39, no. 1, pp. 150–164, Jan. 2014.

[41] D. Wang, P. F. J. Lermusiaux, P. J. Haley, D. Eickstedt, W. G. Leslie, and H. Schmidt, "Acoustically focused adaptive sampling and on-board routing for marine rapid environmental assessment," *Journal of Marine Systems*, vol. 78, pp. S393–S407, Nov. 2009.

[42] J. A. Farrell, S. Pang, W. Li, and R. Arrieta, "Chemical plume tracing experimental results with a REMUS AUV," in *Oceans 2003. Celebrating the Past ... Teaming Toward the Future (IEEE Cat. No.03CH37492)*, 2003, vol. 2, pp. 962-968 Vol.2.

[43] J. A. Farrell and and, "Chemical plume tracing via an autonomous underwater vehicle," *IEEE Journal of Oceanic Engineering*, vol. 30, no. 2, pp. 428–442, Apr. 2005.

[44] G. Ferri, M. V. Jakuba, and D. R. Yoerger, "A novel trigger-based method for hydrothermal vents prospecting using an autonomous underwater robot," *Auton Robot*, vol. 29, no. 1, pp. 67–83, Jul. 2010.

[45] D. R. Yoerger, M. Jakuba, A. M. Bradley, and B. Bingham, "Techniques for Deep Sea Near Bottom Survey Using an Autonomous Underwater Vehicle," *The International Journal of Robotics Research*, vol. 26, no. 1, pp. 41–54, Jan. 2007.

[46] G. E. Packard, T. Austin, R. Christenson, J. Kaeli, R. Littlefield, M. Purcell, and R. Stokey, "Servo controlled rapid MCM target reacquisition using REMUS-100," in *2014 Oceans - St. John's*, 2014, pp. 1–3.

[47] M. Quigley, K. Conley, B. Gerkey, J. Faust, T. Foote, J. Leibs, R. Wheeler, and A. Y. Ng, "ROS: an open-source Robot Operating System," in *ICRA workshop on open source software*, 2009, vol. 3, p. 5.

[48] B. Gerkey, "ROS, the Robot Operating System, Is Growing Faster Than Ever, Celebrates 8 Years," *IEEE Spectrum: Technology, Engineering, and Science News*, 09-Dec-2015.

[49] M. Carreras, C. Candela, D. Ribas, A. Mallios, E. Vidal, N. Palomeras, and P. Ridao, "M5 SPARUS II, DESIGN OF A LIGHTWEIGHT HOVERING AUV," p. 2.

[50] K. DeMarco, M. E. West, and T. R. Collins, "An implementation of ROS on the Yellowfin autonomous underwater vehicle (AUV)," in *OCEANS'11 MTS/IEEE KONA*, 2011, pp. 1–7.

[51] "Hydroid Introduces the New Generation REMUS 100 AUV | Hydroid, Inc." [Online]. Available: https://www.hydroid.com/news/hydroid-introduces-new-generation-remus-100-auv. [Accessed: 06-Oct-2018].

[52] T. Austin and R. Stokey, "Integrated Mission, Vehicle, and Sensor Control of the iPUMA AUV:," Defense Technical Information Center, Fort Belvoir, VA, Nov. 2011.

[53] "Documentation - ROS Wiki." [Online]. Available: http://wiki.ros.org/. [Accessed: 20-Sep-2018].

[54] "dynamic_reconfigure - ROS Wiki." [Online]. Available: http://wiki.ros.org/dynamic_reconfigure. [Accessed: 04-Oct-2018].

[55] "actionlib/DetailedDescription - ROS Wiki." [Online]. Available: http://wiki.ros.org/actionlib/DetailedDescription. [Accessed: 06-Jul-2018].

[56] "smach/Documentation - ROS Wiki." [Online]. Available: http://wiki.ros.org/smach/Documentation. [Accessed: 05-Oct-2018].

[57] Sergi Hernandez Juan and Fernando Herrero Cotarelo, "Multi-master ROS Systems," Institut de Robòtica i Informàtica Industrial (IRI), Universitat Politècnica de Catalunya (UPC), Barcelona, Spain, IRI-TR-15-1, Jan. 2015.

[58] B. Allotta, F. Fanelli, N. Monni, C. Petrioli, L. Picari, A. Ridolfi, and D. Spaccini, "Enabling cooperation and networking in heterogeneous underwater networks composed of multi-vendor vehicles and modems," in *OCEANS 2017 - Aberdeen*, 2017, pp. 1–7.

[59] E. Gallimore, J. Partan, I. Vaughn, S. Singh, J. Shusta, and L. Freitag, "The WHOI micromodem-2: A scalable system for acoustic communications and networking," in *OCEANS 2010*, 2010, pp. 1–7.

[60] T. Schneider, S. Petillo, H. Schmidt, and C. Murphy, "The Dynamic Compact Control Language version 3," in *OCEANS 2015 - Genova*, 2015, pp. 1–7.

[61] T. C. Austin, "The application of spread spectrum signaling techniques to underwater acoustic navigation," in *Autonomous Underwater Vehicle Technology, 1994. AUV'94., Proceedings of the 1994 Symposium on*, 1994, pp. 443–449.

[62] T. Fulton, "Acoustic navigation for the autonomous underwater vehicle REMUS," Thesis, Massachusetts Institute of Technology, 2000.

[63] R. M. Eustice, L. L. Whitcomb, H. Singh, and M. Grund, "Recent Advances in Synchronous-Clock One-Way-Travel-Time Acoustic Navigation," in *OCEANS 2006*, 2006, pp. 1–6.

[64] R. M. Eustice, L. L. Whitcomb, H. Singh, and M. Grund, "Experimental Results in Synchronous-Clock One-Way-Travel-Time Acoustic Navigation for Autonomous Underwater Vehicles," in *2007 IEEE International Conference on Robotics and Automation*, 2007, pp. 4257–4264.

[65] S. Singh, M. Grund, B. Bingham, R. Eustice, H. Singh, and L. Freitag, "Underwater Acoustic Navigation with the WHOI Micro-Modem," in *OCEANS 2006*, 2006, pp. 1–4.

[66] M. Stojanovic, L. Freitag, J. Leonard, and P. Newman, "A network protocol for multiple AUV localization," in *OCEANS '02 MTS/IEEE*, 2002, vol. 1, pp. 604–611 vol.1.

[67] M. B. Larsen, "Synthetic long baseline navigation of underwater vehicles," in *OCEANS 2000 MTS/IEEE Conference and Exhibition*, 2000, vol. 3, pp. 2043–2050 vol.3.

[68] J. C. Hartsfield, "Single transponder range only navigation geometry (STRONG) applied to REMUS autonomous under water vehicles," Thesis, Massachusetts Institute of Technology, 2005.

[69] Y. Watanabe, H. Ochi, and T. Shimura, "A study of inverse SSBL acoustic positioning with data transmission for multiple AUV navigation," in *OCEANS, 2012 - Yeosu*, 2012, pp. 1–6.

[70] Y. Watanabe, H. Ochi, T. Shimura, and T. Hattori, "A tracking of AUV with integration of SSBL acoustic positioning and transmitted INS data," in *OCEANS 2009 - EUROPE*, 2009, pp. 1–6.

[71] Y. Watanabe, H. Ochi, T. Shimura, and T. Hattori, "Super Short Baseline Underwater Acoustic Positioning Supported by Inertial Navigation Data Using Spread Spectrum Communication for Autonomous Underwater Vehicle and Error Analysis in Deep Water," *Japanese Journal of Applied Physics*, vol. 48, no. 7, p. 07GL01, Jul. 2009.

[72] T. C. Yang, "Source depth estimation based on synthetic aperture beamfoming for a moving source," *The Journal of the Acoustical Society of America*, vol. 138, no. 3, pp. 1678–1686, Sep. 2015.

[73] P. Rigby, O. Pizarro, and S. B. Williams, "Towards Geo-Referenced AUV Navigation Through Fusion of USBL and DVL Measurements," in *OCEANS 2006*, 2006, pp. 1–6.

[74] F. Gustafsson, *Statistical Sensor Fusion*. Lund, Sweden: Studentlitteratur, 2012.

[75] M. Johnson, L. Freitag, and M. Stojanovic, "Improved Doppler tracking and correction for underwater acoustic communications," in *, 1997 IEEE International Conference on Acoustics, Speech, and Signal Processing, 1997. ICASSP-97*, 1997, vol. 1, pp. 575–578 vol.1.

[76] M. Stojanovic, J. A. Catipovic, and J. G. Proakis, "Phase-coherent digital communications for underwater acoustic channels," *IEEE Journal of Oceanic Engineering*, vol. 19, no. 1, pp. 100–111, Jan. 1994.

[77] Teledyne RD Instruments, "Workhorse Navigator Doppler Velocity Log (DVL) Datasheet." .

[78] S. J. Julier and J. K. Uhlmann, "New extension of the Kalman filter to nonlinear systems," 1997, pp. 182–193.

[79] E. A. Wan and R. V. D. Merwe, "The unscented Kalman filter for nonlinear estimation," in *Adaptive Systems for Signal Processing, Communications, and Control Symposium 2000. AS-SPCC. The IEEE 2000*, 2000, pp. 153–158.

[80] S. J. Julier and J. K. Uhlmann, "Unscented filtering and nonlinear estimation," *Proceedings of the IEEE*, vol. 92, no. 3, pp. 401–422, 2004.

[81] D. Simon, *Optimal state estimation: Kalman, H [infinity] and nonlinear approaches*. Hoboken, N.J: Wiley-Interscience, 2006.

[82] B. Ristic, S. Arulampalam, and N. Gordon, *Beyond the Kalman Filter: Particle Filters for Tracking Applications*. Boston, MA: Artech Print on Demand, 2004.

[83] O. Cappe, S. J. Godsill, and E. Moulines, "An Overview of Existing Methods and Recent Advances in Sequential Monte Carlo," *Proceedings of the IEEE*, vol. 95, no. 5, pp. 899–924, May 2007.

[84] F. Gustafsson, "Particle filter theory and practice with positioning applications," *IEEE Aerospace and Electronic Systems Magazine*, vol. 25, no. 7, pp. 53–82, Jul. 2010.

[85] J. D. Hol, T. B. Schon, and F. Gustafsson, "On resampling algorithms for particle filters," in *Nonlinear Statistical Signal Processing Workshop, 2006 IEEE*, 2006, pp. 79–82.

[86] E. Gallimore, J. Partan, S. Singh, L. Freitag, K. Ball, P. Koski, and A. Beal, "Developments in timing and satellite telemetry with the Micromodem-2," in *7th ACM International Conference on Underwater Networks and Systems (WUWNet '12)*, Los Angeles, CA, 2012.

[87] J. Kitching, S. Knappe, V. Shah, P. Schwindt, C. Griffith, R. Jimenez, J. Preusser, L. A. Liew, and J. Moreland, "Microfabricated atomic magnetometers and applications," in *2008 IEEE International Frequency Control Symposium*, 2008, pp. 789–794.

[88] M. Prouty, "A Miniature Wide Band Atomic Magnetometer," DTIC Document, 2011.

[89] T. R. Clem, J. T. Bono, P. S. Davis, D. J. Overway, L. Vaizer, D. King, A. Torres, T. Austin, R. P. Stokey, and G. Packard, "Initial Buried Minehunting Demonstration of the Laser Scalar Gradiometer Operating Onboard REMUS 600," in *OCEANS 2006*, 2006, pp. 1–7.

[90] T. R. Clem, P. S. Davis, R. J. McDonald, D. I. Overway, J. W. Purpura, L. Vaizer, and D. King, "Preliminary evaluation of the laser scalar gradiometer for buried minehunting," in *Proceedings of MTS/IEEE OCEANS, 2005*, 2005, pp. 1944-1955 Vol. 3.

[91] S. Kumar, D. C. Skvoretz, C. R. Moeller, M. J. Ebbert, A. R. Perry, R. K. Ostrom, A. Tzouris, S. L. Bennett, and P. A. Czipott, "Real-Time Tracking Gradiometer for use in an autonomous underwater vehicle for buried minehunting," in *Proceedings of OCEANS 2005 MTS/IEEE*, 2005, pp. 2108-2111 Vol. 3.

[92] G. Sulzberger, J. Bono, R. J. Manley, T. Clem, L. Vaizer, and R. Holtzapple, "Hunting sea mines with UUV-based magnetic and electro-optic sensors," in *OCEANS 2009*, 2009, pp. 1–5.

[93] Graham Chandler, "AUV Magnetometers a leap forward in seabed surveying," *Earth Explorer*, 08-Mar-2013.

[94] R. Steigerwalt, "Autonomous Underwater Munitions and Explosives of Concern Detection System," Mar. 2015.

[95] R. Steigerwalt, R. M. Johnson, A. C. Trembanis, V. E. Schmidt, and G. Tait, "Autonomous Underwater Vehicle Magnetic Mapping System," *AGU Fall Meeting Abstracts*, vol. 51, Dec. 2012.

[96] "Marine Magnetics Explorer and Gavia Trials: Trial Data from Sensor Integration." Teledyne Marine, 12-Oct-2018.

[97] Dana Yoerger and James Kinsey, "Sentry Autonomous Underwater Vehicle (AUV) Operational Guidelines and Scientific Capabilities," Woods Hole Oceanographic Institution, Nov. 2010.

[98] A. K. Shah, M.-H. Cormier, W. B. F. Ryan, W. Jin, J. Sinton, E. Bergmanis, J. Carlut, A. Bradley, and D. Yoerger, "Episodic dike swarms inferred from near-bottom magnetic anomaly maps at the southern East Pacific Rise," *Journal of Geophysical Research: Solid Earth*, vol. 108, no. B2, 2003.

[99] M. A. Tivey, H. P. Johnson, A. Bradley, and D. Yoerger, "Thickness of a submarine lava flow determined from near-bottom magnetic field mapping by autonomous underwater vehicle," *Geophysical Research Letters*, vol. 25, no. 6, pp. 805–808, 1998.

[100] F. C. Teixeira, J. Quintas, and A. Pascoal, "Experimental validation of magnetic navigation of marine robotic vehicles*," *IFAC-PapersOnLine*, vol. 49, no. 23, pp. 273–278, 2016.

[101] J. Lenz and S. Edelstein, "Magnetic sensors and their applications," *IEEE Sensors Journal*, vol. 6, no. 3, pp. 631–649, Jun. 2006.

[102] J. Kitching, S. Knappe, W. C. Griffith, J. Preusser, V. Gerginov, P. D. D. Schwindt, V. Shah, and R. Jimenez-Martinez, "Uncooled, millimeter-scale atomic magnetometers with femtotesla sensitivity," in *2009 IEEE Sensors*, 2009, pp. 1844–1847.

[103] R. Zhang, K. Smith, and R. Mhaskar, "Highly sensitive miniature scalar optical gradiometer," in *2016 IEEE SENSORS*, 2016, pp. 1–3.

[104] S. D. Billings, L. R. Passion, and D. W. Oldenburg, "UXO Discrimination and Identification Using Magnetometry," in *Symposium on the Application of Geophysics to Engineering and Environmental Problems 2002*, 2002, pp. 12UXO4-12UXO4.

[105] J. E. McFee, Y. Das, and R. O. Ellingson, "Locating and identifying compact ferrous objects," *IEEE Transactions on Geoscience and Remote Sensing*, vol. 28, no. 2, pp. 182–193, Mar. 1990.

[106] L. Vaizer, J. Lathrop, and J. Bono, "Localization of magnetic dipole targets," in *Oceans '04 MTS/IEEE Techno-Ocean '04 (IEEE Cat. No.04CH37600)*, 2004, vol. 2, pp. 869-873 Vol.2.

[107] S. D. Billings and F. J. Herrmann, "Automatic detection of position and depth of potential UXO using continuous wavelet transforms," in *Detection and Remediation Technologies for Mines and Minelike Targets VIII*, 2003, vol. 5089, pp. 1012–1023.

[108] R. Davis, J. Bellingham, P. Chandler, F. Chavez, N. Leoanard, and A. Robinson, "AOSN II system goals and performance metrics," Monterey Bay Aquarium Research Institute, 2003.

[109] V. Djapic and D. Nad, "Using collaborative Autonomous Vehicles in Mine Countermeasures," in *OCEANS 2010 IEEE - Sydney*, 2010, pp. 1–7.

[110] M. R. Benjamin, H. Schmidt, P. M. Newman, and J. J. Leonard, "Nested autonomy for unmanned marine vehicles with MOOS-IvP," *J. Field Robotics*, vol. 27, no. 6, pp. 834–875, Nov. 2010.

[111] M. Mandea and M. Korte, Eds., *Geomagnetic Observations and Models*. Dordrecht: Springer Netherlands, 2011.

[112] G. I. Allen, R. Matthews, and M. Wynn, "Mitigation of platform generated magnetic noise impressed on a magnetic sensor mounted in an autonomous underwater vehicle," in *MTS/IEEE Oceans 2001. An Ocean Odyssey. Conference Proceedings (IEEE Cat. No.01CH37295)*, 2001, vol. 1, pp. 63–71 vol.1.

[113] E. Gallimore, R. Stokey, and E. Terrill, "Robot Operating System (ROS) on the REMUS AUV using RECON," in *Proceedings of the 2018 IEEE OES Autonomous Underwater Vehicle Symposium*, Porto, Portugal, 2018.

[114] M. Prouty, K. Smith, and R. Johnson, "Performance considerations for total field magnetometers," in *Proceedings of IEEE Sensors, 2003*, 2003, vol. 1, pp. 483-486 Vol.1.

[115] "Explorer Mini Marine Magnetometer Brochure." Marine Magnetics.

[116] J. M. D. Day, A. A. P. Koppers, B. C. Mendenhall, and B. Oller, "The 'Scripps Dike' and its implications for mid-Miocene volcanism and tectonics of the California Continental Borderland," in *From the Mountains to the Abyss: The California Borderland as an Archive of Southern California Geologic Evolution - SEPM Special Publication*, vol. 110, Society for Sedimentary Geology, 2018.

[117] A. Chulliat, P. Alken, M. Nair, A. Woods, and S. Maus, "The Enhanced Magnetic Model 2015-2020." National Centers for Environmental Information, NOAA, 2015.

[118] M. Tchernychev, J. Johnston, and R. Johnson, "Transverse Total Magnetic Field Gradiometer Marine Survey in Hawaii: The Quasi-Analytic Signal Approach and Multi-Channel Total Field Dipole Modeling," in *Symposium on the Application of Geophysics to Engineering and Environmental Problems 2009*, 2009, pp. 424–433.

[119] M. Tchernychev, R. Johnson, and J. Kulpa, "Using a transverse marine gradiometer (TVG) as submarine pipeline location tool," in *2013 OCEANS - San Diego*, 2013, pp. 1–6.

[120] A. Salem, D. Ravat, T. J. Gamey, and K. Ushijima, "Analytic signal approach and its applicability in environmental magnetic investigations," *Journal of Applied Geophysics*, vol. 49, no. 4, pp. 231–244, Apr. 2002.

[121] A. Chulliat, S. Macmillan, P. Alken, C. Beggan, M. Nair, B. Hamilton, A. Woods, V. Ridley, S. Maus, and A. Thomson, "The US/UK World Magnetic Model for 2015-2020," NOAA National Geophysical Data Center, Boulder, CO, 2014.

[122] S. Breiner, "Applications manual for portable magnetometers." Geometrics, San Jose, 1999.

[123] S. M. Kay, *Fundamentals of Statistical Signal Processing: Practical algorithm development*. Pearson Education, 2013.

[124] S. M. Kay, *Fundamentals Of Statistical Processing, Volume 2: Detection Theory*. Pearson Education, 2009.

[125] Grami, Ali, *Introduction to Digital Communications*. Elsevier, 2016.

[126] B. M. Carrier, A. Pulkkinen, and M. Heinz, "Recognizing Geomagnetic Storms in Marine Magnetometer Data: Toward Improved Archaeological Resource Identification Practices," *STAR: Science & Technology of Archaeological Research*, vol. 2, no. 1, pp. 1–14, Jan. 2016.

[127] ASM International, Ed., *ASM ready reference. Electrical and magnetic properties of metals*. Materials Park, OH: ASM International, 2000.

[128] G. C. English and William King, "Investigation of the Mechanism of Stress Corrosion of Aluminum Alloys," Alcoa Research Laboratories, 602120, Jul. 1964.

[129] "Overhaul Instructions Models R-1830-43, -43A, -65, -65A, -90C, and -90D Aircraft Engines." Secretary of the Air Force, 01-Mar-1947.

[130] J. I. Boyce, E. G. Reinhardt, A. Raban, and M. R. Pozza, "Marine Magnetic Survey of a Submerged Roman Harbour, Caesarea Maritima, Israel," *International Journal of Nautical Archaeology*, vol. 33, no. 1, pp. 122–136, 2004.

[131] J. J. Boshoff, "The Search for the Slave Ship Meermin. Developing a Methodology for Finding Inter Tidal Shipwrecks," University of South Africa, Pretoria, South Africa, 2018.

[132] M. Pilkington and J. B Thurston, "Draping corrections for aeromagnetic data: Line versus grid-based approaches," *Exploration Geophysics*, vol. 32, pp. 95–101, Jan. 2001.